# QUANTITATIVE BACKGROUND-ORIENTED SCHLIEREN (BOS) MEASUREMENTS OF EXPLOSIVES AND HIGH-SPEED PROJECTILES USING OPTICAL FLOW TECHNIQUES

by

Kailene Marie Strebe

Submitted in Partial Fulfillment
of the Requirements for the Degree of
Master of Science in Mechanical Engineering
with Specialization in Explosives Engineering

NEW MEXICO TECH
SCIENCE • ENGINEERING • RESEARCH UNIVERSITY
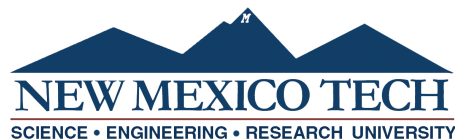
New Mexico Institute of Mining and Technology
Socorro, New Mexico
August, 2023

This thesis is dedicated to my wonderful husband for his never-ending encouragement and support in all things.

Kailene Marie Strebe
New Mexico Institute of Mining and Technology
August, 2023

ACKNOWLEDGMENTS

I would like to thank my advisor Dr. Hargather for his guidance and patience on this project, as well as the members of the SGDL for their help and feedback. I want to thank my friends in Christian Challenge for their friendship and fellowship throughout the years, and my family for their love and support. Finally, I would like to thank my husband Luke for encouraging me and being my study partner through undergraduate and graduate school.

This thesis was typeset with LaTeX[1] by the author.

---

[1] The LaTeX document preparation system was developed by Leslie Lamport as a special version of Donald Knuth's TeX program for computer typesetting. TeX is a trademark of the American Mathematical Society. The LaTeX macro package for the New Mexico Institute of Mining and Technology thesis format was written by John W. Shipman.

ABSTRACT

Background-oriented schlieren (BOS) is a refractive imaging technique that is used to visualize refractive disturbances without the size limitations that traditional schlieren techniques have. Many BOS images are processed using block-matching techniques which have limitations for identifying small disturbances in a refractive flow. Optical flow is an image processing technique that has been shown to provide more detailed results than block-matching techniques. The various optical flow techniques, however, have not been compared for applications in compressible flows and specifically for shock wave quantification. Here the Horn-Schunck and Lucas-Kanade gradient-based optical flow techniques are used to reconstruct the density field around supersonic projectiles and an explosive blast. The reconstructed density fields are compared between optical flow processing methods and to traditional quantitative schlieren and field pressure measurements. The optical flow techniques are compared at a small scale using a $10°$ half-angle conical projectile traveling at Mach 2.15. The techniques are then compared at a large scale with a 1 kg spherical explosion of C4. Both optical flow techniques are shown to produce density and pressure profiles that agree with traditional data acquisition techniques, but Horn-Schunck tends to produce more accurate results and less error than Lucas-Kanade in both small-scale and large-scale settings.

Keywords: High-Speed Imaging; Background-Oriented Schlieren; Optical Flow; BOS; Explosives; Projectiles

CONTENTS

LIST OF TABLES

LIST OF FIGURES

This thesis is accepted on behalf of the faculty of the Institute by the following committee:

<div align="center">

Michael Hargather

</div>

<div align="center">

Academic and Research Advisor

</div>

<div align="center">

Tei Wei

</div>

<div align="center">

David Morrow

</div>

I release this document to the New Mexico Institute of Mining and Technology.

Kailene Marie Strebe   August, 2023

CHAPTER 1

INTRODUCTION

1.1   Research Motivation

Background-oriented schlieren (BOS) is a method for imaging and measuring fluid flows via the distortion of a distant background. BOS visualizes refractive index disturbances which are related to density differences in the fluid medium being imaged. The BOS method is of interest because it can be used to visualize flow fields at a larger scale than traditional refractive imaging methods, such as schlieren, which requires precision optics that define the available field of view. Recent work at NASA Armstrong [1] highlights the large-scale capabilities of BOS with the visualization of detailed shock structures around a supersonic jet in flight. The history of BOS and typical applications are well documented by Raffel [2].

BOS has been used to visualize explosives [3, 4] and supersonic flows [5, 6] of varying sizes. Some research has used BOS to analyze the explosively-driven shock waves to measure the Mach number (M) and initial pressure rise of the shock [3, 4], while others have used BOS to reconstruct temperature [7] and density behind shock fronts [5, 8, 9]. Quantitative reconstruction via BOS increases the spatio-temporal understanding of a blast field, which is a focus of the present work.

The quality of the reconstructed flow field is directly related to the post-processing techniques used to analyze the BOS data. Most BOS data is processed with block matching or cross-correlation techniques using a method similar to particle image velocimetry (PIV). While block-matching techniques have been shown to process BOS data well [7, 9, 10], they require BOS images to be divided into relatively large windows and then processed, which leads to spatial averaging over the entire window. Optical flow, or OF, is a post-processing technique that detects changes in intensity between image pairs, and functions similarly to block-matching techniques, but divides the data into significantly smaller windows. OF is typically used in computer vision for autonomous vehicle navigation [11, 12] and stereovision [13], but it has recently been implemented with BOS [14–16]. Atcheson [14] evaluated the performance of different OF algorithms for incompressible flows, and while many researchers have used OF techniques for compressible flows, there is no research comparing the results of the different OF algorithms within the context of compressible flows with shock waves. The

present work will compare the effectiveness of two main OF algorithms specifically for compressible flow data.

1.2 Refractive Imaging Techniques

Refractive imaging is a way to measure the apparent bending of light as it passes through regions of different refractive indexes. There are several imaging techniques to measure the refractive index, including interferometry, schlieren, and BOS. In a typical test setup, the refraction angle is the output of the refractive imaging method, which can be related to the refractive index gradient:

$$\varepsilon_y = \int \frac{1}{n}\frac{\delta n}{\delta y}dz \tag{1.1}$$

The refractive index is then related back to density via the Gladstone-Dale relation:

$$n = \kappa\rho + 1 \tag{1.2}$$

where ρ is density, n is the refractive index and κ is the Gladstone-Dale constant.

1.2.1 Interferometry

Interferometry uses wave interference to measure distances and refractive index fields [17]. For optical techniques, mirrors and beam splitters are used to detect light wave interference. The resulting light intensity at the point of interference is determined by constructive or destructive interference. When light waves interfere constructively a bright band is created, and when they interfere destructively dark bands are created, thus creating a pattern of light and dark bands referred to as fringes. Fringes are used to determine the refractive index of the material the light has passed through.

There are many different interferometers with unique designs to measure specific factors, Hariharan and Steel discuss these different interferometers and their applications in their respective books [17,18]. In the book by Settles [19], a set of techniques are defined as "Schlieren interferometry" which are interferometry techniques that can produce images optically similar to schlieren. Settles used a z-type schlieren system where the knife-edge was replaced with a birefringent Wollaston prism, causing interference between light beams with slightly different phases or optical path lengths. The interference fringe pattern is proportional to the refractive index gradient of the object.

Interferometry is a useful tool [20], but it requires a significant amount of effort, time, and equipment to set up and is less favorable today than schlieren or BOS because of their simpler setups.

1.2.2 Schlieren

Schlieren imaging is a refractive imaging technique that is widely used to visualize fluid flows. It can be applied to incompressible flows as well as compressible flows. The traditional parallel light schlieren setup uses a set of mirrors or lenses to visualize how light bends as it passes through a refractive index field.
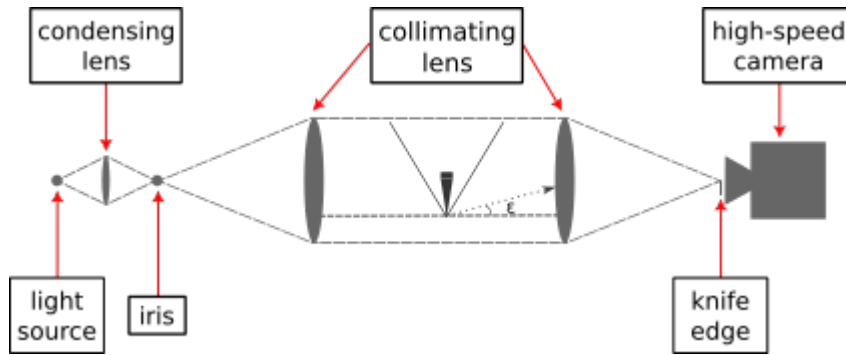
Figure 1.1: Schematic of a schlieren test setup

For the parallel light schlieren system, which is shown schematically in Figure 1.1, light from a light source passes through a condensing lens that focuses the light to a point. At that point, the light is passed through an iris which allows the light to imitate a point source of a known physical size. The light then expands to a collimating lens which makes the light parallel in the test region. At the end of the test region, the light passes through another collimating lens which focuses the light back down to a point where a knife edge is placed. Refracted light intersects or passes the knife edge, resulting in locations being highlighted or darkened because of the knife edge cut-off. The knife edge is what gives the schlieren image its characteristic light-dark gradient. The same optical arrangement with no knife edge is a focused shadowgraph system.

To quantify how light is bent, a weak calibration lens, as exemplified in Figure 1.2, with a known focal length is imaged in the test section prior to testing. The calibration lens image allows the correlation of intensity variation to a local refraction angle. This allows for the refractive index gradient of the known calibration image to be compared to the refractive index gradient of an unknown schlieren object. Schlieren is beneficial because it does not require any post-processing to see the refractive image. The issue with schlieren is that the test section is constrained to the size of mirrors or lenses used, so experiments requiring larger fields of view are either too expensive or infeasible.
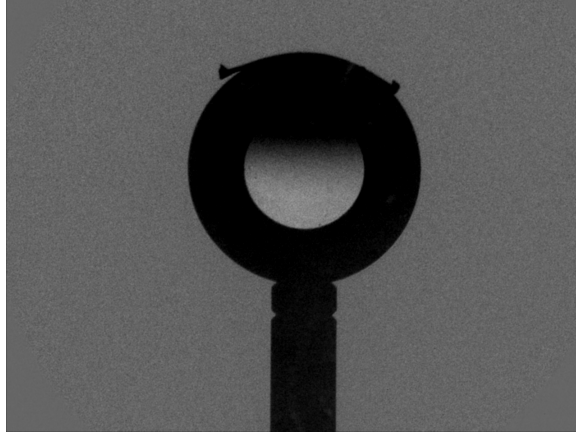
Figure 1.2: Weak calibration lens with a focal length of 4 m used to correlate image intensity to refraction angle.

1.2.3 Background Oriented Schlieren (BOS)

A BOS setup is shown schematically in Figure 1.3 with two import distances: camera to object, l, and camera to the background, L. To maximize the sensitivity of the system the ratio, $\frac{l}{L}$ should be minimized while striving to keep both object and background in focus [21]. The overall length of the system is typically dependent on test setup constraints and the desired field of view.
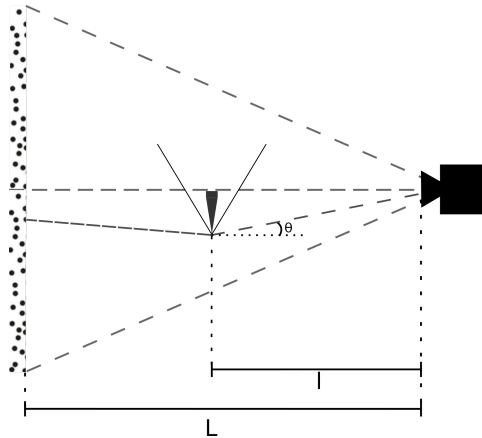
Figure 1.3: Schematic of a BOS setup with the speckled background shown on the left, the schlieren object shown in the middle, and the high-speed camera on the right. A visual representation of a background distortion is shown by the dashed line connecting the schlieren object to the background, and the corresponding refractive angle labeled as θ.

BOS uses background distortion to identify locations of refractive index gradients in a field of view [22]. In practice, the technique identifies changes between a pair of images that are a result of refractive disturbances. The pair of images needed is a reference image, referred to as the "flow-off" image, and an image of interest, the "flow-on" image. The flow-off image is typically an image captured before the flow-on image with an undistorted view of the background. A flow-on image can be any image with some distortion of interest. If there is a series of flow-on images that are of interest to visualize, they would all be processed by comparing them back to the same flow-off image. There are some cases where the frame immediately before the flow-on image is used as the flow-off image and this is called sequential BOS. Using the image immediately before the frame of interest visualizes the changes between the pair as a temporal variation in the refractive index field [22]. Figure 1.4 shows the difference between background subtracted BOS and sequential subtracted BOS. In the sequential subtracted BOS, the shock wave from both the flow-off and flow-on image can be seen, as well as the changes inside the fireball. Sequential subtraction is not useful for this current work, so only the undistorted reference image will be used as the flow-off image.
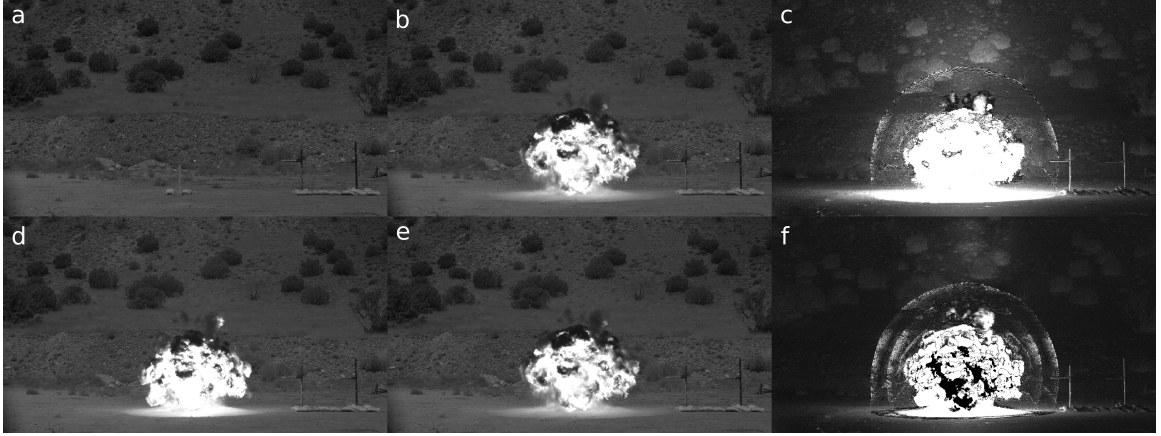
Figure 1.4: A comparison between using an undistorted flow-off image (a-c) and a distorted flow-off image for background subtraction BOS. a) flow-off image with an undistorted background, b) flow-on image of interest, c) resulting BOS image, d) flow-off image with a distorted background, e) flow-on image of interest, f) resulting sequential subtraction BOS. Both cases use the same image for the flow-on. In (c) the shock wave is clearly visible. In (f) there appears to be two shock waves, which is the position of the shock wave in images (d) and (c) respectively.

BOS requires post-processing to visualize any shifts that occur between the pair of images. Depending on the post-processing technique, the change identified in the image can either be quantitative or qualitative. One qualitative approach described by Hargather and Settles [22] simply compares each pixel in

5

the flow-off image to the respective pixel in the flow-on image according to the equation:

$$\text{new}(i,j) = \frac{(\text{hot}(i,j) - \text{cold}(i,j))^2}{\frac{\text{hot}(i,j) + \text{cold}(i,j)}{2} + 1} \tag{1.3}$$

where (i,j) corresponds to a pixel location within the image. This approach highlights any intensity changes detected between the images and darkens regions where there are no intensity changes detected. This technique was used in Figure 1.4 to show the difference between sequential and background-subtracted images and is similar to shadowgraph imaging.

Quantitative post-processing techniques include block-matching, cross-correlation, and optical flow algorithms, which yield images that are optically equivalent to schlieren images. Each of these techniques operate similarly to each other. Figure 1.5 schematically represents how block-matching techniques divide the flow-off image into smaller windows and then search the flow-on image until it finds a region that best matches each window. This process allows for the movement caused by a shock wave or other refractive event to be located and measured. The difference between block-matching and OF methods is the window size and function that is minimized to match each window. Cross-correlation and block-matching algorithms typically have a larger window size of around 16x16 pixels, and OF can have a window size as small as 3x3 pixels [14].Thus, OF is a desirable technique because it is more sensitive to refractive disturbances than block-matching techniques.
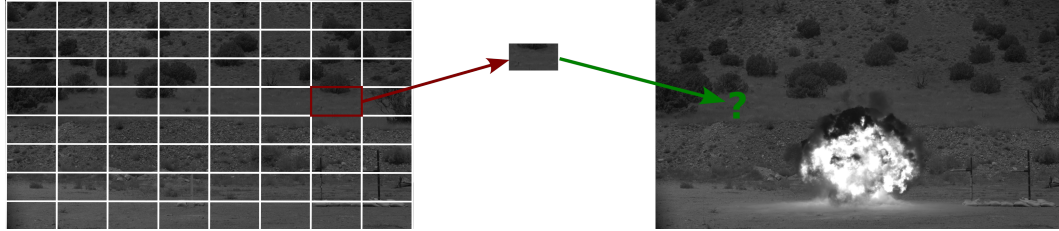
Figure 1.5: Example of how quantitative BOS analysis works. The left image is the flow-off image which is divided into smaller windows; each window is then compared to the flow-on image using a cross-correlation algorithm and matched to a best-fit region.

1.3 Optical Flow

Optical flow measures the apparent motion of light intensity in an image. Optical flow is defined by the equation:

$$I(x,y,t) = I(x + dx, y + dy, t + dt) \tag{1.4}$$

where $I(x, y, t)$ is the intensity inside the flow-off image, and $I(x + dx, y + dy, t + dt)$ is the intensity in the flow-on image. dx is the perceived horizontal intensity movement, dy is the perceived vertical intensity movement, and dt is the time step between the images. OF assumes the image intensity is constant between the flow-off and flow-on images and that the intensity has shifted due to the refractive disturbance.

There are many different OF techniques that have been extensively compared for computer vision by Barron et. al. [23], including differential techniques (first-order and second-order), block-matching, energy-based methods, and phase-based methods. Atcheson et. al. [14] evaluated different OF techniques for BOS imaging which included block-matching algorithms, gradient-based techniques (first-order differential techniques), multi-scale multi-resolution methods, and variational algorithms. Atcheson et. al. [14] found that first-order differential techniques provide more accurate results than block-matching methods and that variational approaches tend to over-smooth the high-frequency data found in BOS data sets. Although first-order differential models have been shown to be more accurate, there have only been a few implementations of it with supersonic BOS data sets [5, 15, 16, 24].

A supersonic jet flow has been reconstructed [25] using the Lucas-Kanade method [13]. Underwater shock waves were analyzed by Hayaskaka et. al. [15] using a combination of the Horn-Schunck method [26] and the Liu-Shen variational model [27]. The flow-field around a wedge in a flow of $M = 3.5$ [28] was analyzed using a Horn-Schunck variation introduced by Sun et. al. [28] and the flow around a cone in a $M = 2$ flow [5] was reconstructed using a variational method introduced by Schmidt and Woike [29]. None of these recent works have compared the results of multiple OF techniques or applied OF to large-scale tests with high-explosives.

1.4   Goals of Current Research

Optical flow has proven to be a great tool for analyzing BOS images and extracting quantitative data. Research has shown that OF data produces better results than block-matching techniques, but there have not been studies that compare different OF methods and their results for compressible flows. Due to the positive results from Atcheson and Barron with implementing first-order differential techniques, this work will compare two key first-order differential OF algorithms: Horn-Schunck (HS) [26] and Lucas-Kanade (LK) [13, 30]. The HS and LK algorithms will be applied to both ballistic and high-explosive tests, and then the results from each algorithm will be used to create a density reconstruction behind the shock front of each event. These density values will be compared to theoretical results and quantitative schlieren measurements to determine how well each OF method works in different settings and scenarios.

CHAPTER 2

EXPERIMENTAL METHODS

To test the application of OF with compressible flows, small-scale and large-scale tests were performed. For the small-scale tests, the flow field over 0.50"-caliber (12.7-mm-diameter) conical projectile was analyzed. For the large-scale tests, the shock propagation from varying charges of C4 were investigated.

2.1 High Speed Imaging

A camera with a fast frame rate is required to visualize supersonic events. There are many options when it comes to high-speed cameras and it is important to select the correct type of camera for the experiment. Key factors that must be considered before selecting a high-speed camera include the resolution, duration of the event, and field of view (FOV). Because the sensitivity of a BOS system is directly related to camera resolution, it is desirable to have the highest-resolution images for analysis. The consequence of high-resolution images with modern high-speed cameras, however, is that the frame rate decreases as resolution increases. Therefore, the first thing that must be considered is the FOV of the experiment. Here the FOV for the small-scale was 0.127 m wide and 10 m wide for the large-scale tests. The known FOV and the assumed velocity of the object (v_{expected}) being imaged was then used to estimate the duration of the event ($t_{\text{in frame}}$) with the equation:

$$t_{\text{in frame}} = \frac{\text{FOV}}{v_{\text{expected}}} \tag{2.1}$$

then the frame rate was set using:

$$\text{Frame Rate} = \frac{\text{\# of frames}}{t_{\text{in frame}}} \tag{2.2}$$

where frame rate is the minimum frame rate required to have # of frames with the object in view. Once the minimum frame rate was found, the camera that can achieve that frame rate and that had the highest resolution was selected.

Other factors that affect data collection included the camera focus, depth of field, and exposure. For BOS experiments it was important to have both the object and background in focus since the background supplies the intensity variations from which the BOS image is created. The depth of field needed to be sufficient to satisfy both of these focus requirements. In these experiments, if only the background or object could be in focus, the background was prioritized because the sharp features of the background are what allow BOS imaging. One instance where the depth-of-field could not be increased was when the ambient lighting was too dim and the minimum exposure would have produced more motion blur than what was desired.

Table 2.1 shows the variety of cameras that have been used for data collection here. In the table, the camera frame rate, resolution, and type of tests imaged are listed.

Table 2.1: Camera varieties and their settings

Camera	Frame Rate (fps)	Pixel Resolution	Test Used
Specialized Imaging SIMX	Variable	1,280 x 960	Small Scale
Shimadzu HPV-X2	1,000,000	400 x 250	Small Scale
Phantom V711	7,500	1,280 x 800	Small Scale
Photron SA-X2	30,000	896 x 496	Small Scale
Photron NOVA S16	30,000	1,024 x 512	Small Scale
Phantom VEO 990	900	4,096 x 2,304	Large Scale
Phantom T1340	2,700	2,048 x 1,952	Large Scale

The small-scale tests prioritized frame rate because the number of frames desired was the driving factor. Large-scale tests prioritized pixel resolution for more detail and the resulting frame rates still satisfied the minimum desired frames.

2.2 Small Scale Tests

The small-scale tests used a pneumatic gun system with a 0.50"-caliber (12.7-mm-diameter) rifled barrel to launch projectiles at supersonic speeds. The projec-

tiles used were 10° half-angle cones machined from 353 brass [31] shown schematically in Figure 2.1. The propellant cartridge was loaded with 9.07 g (140 grains) of IMR 7828 smokeless powder which yielded an exit velocity of approximately 715 m/s. Table 2.2 shows the different cameras that were used for testing with the associated frame rates, the number of frames captured with the projectile in FOV, and the approximate pixel-to-millimeter ratio. A detailed procedure for the testing can be found in Appendix A.
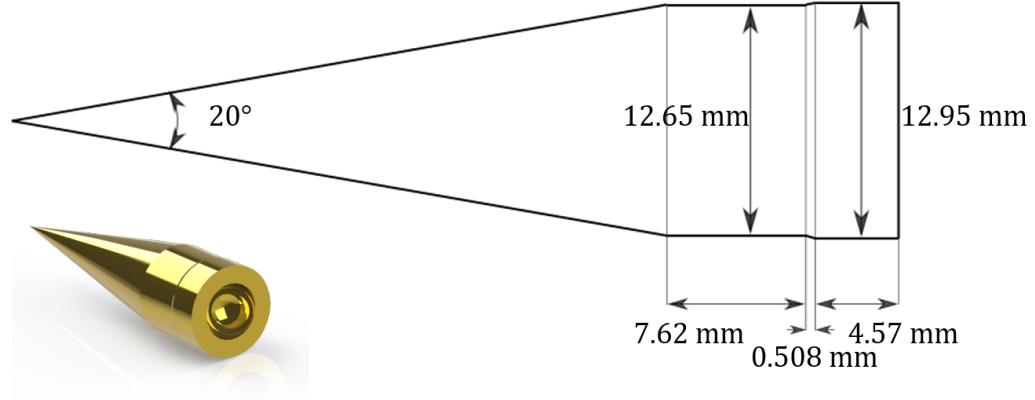
Figure 2.1: Schematic of the 10° half-angle cone projectile used for small-scale testsn[31].

Table 2.2: Cameras used for small scale tests with details

Camera	Frame Rate (fps)	Pixel Resolution	# of Frames	Approximate Ratio (pxl/mm)
Specialized Imaging SIMX	Variable	1,280 x 960	15	10
Shimadzu HPV-X2	1,000,000	400 x 250	178	3
Phantom V711	7,500	1,280 x 800	1	10
Photron SA-X2	30,000	896 x 496	5	7
Photron NOVA S16	30,000	1024 x 512	5	7

A parallel light imaging system was used for these tests and is shown schematically in Figure 2.2. This setup is similar to a schlieren setup except the knife edge was removed and a speckled background was added inside the test region. Figure 2.3 shows the physical test setup with the pneumatic gun system and the

speckled background labeled. This optical setup is used because it enables BOS data and schlieren data to be collected with minimal changes to the test setup between tests; the parallel light simplifies analysis of the small-scale tests and the parallel light BOS produced more than satisfactory background illumination.
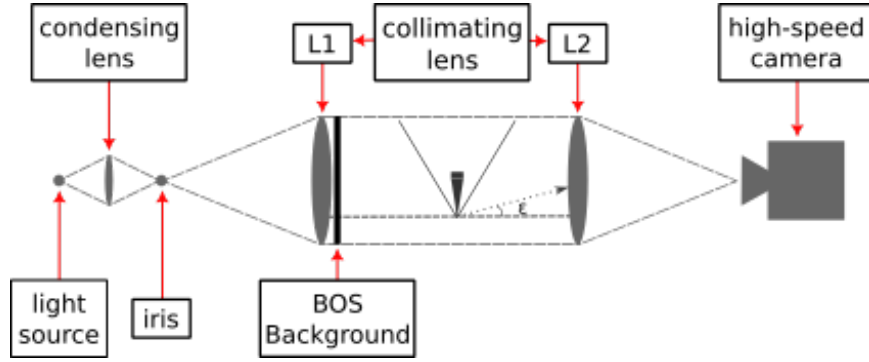
Figure 2.2: Schematic of the optical system with added BOS background and pneumatic gun system
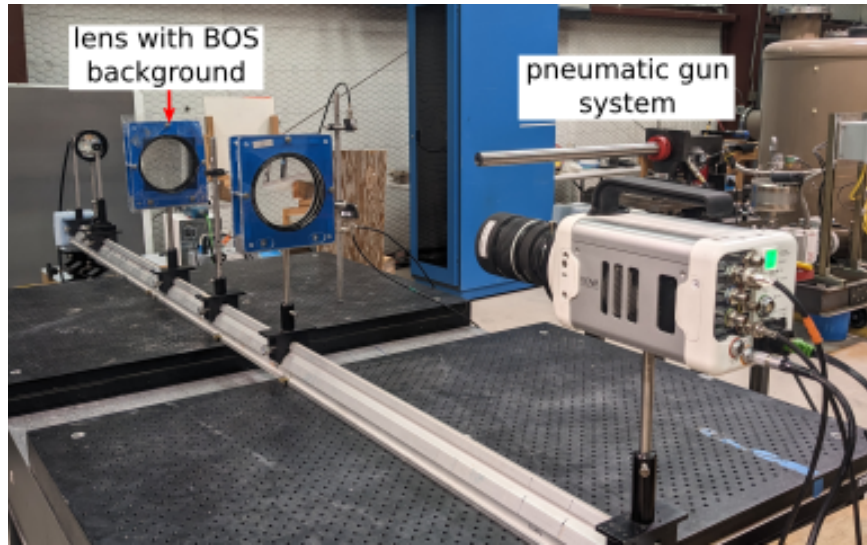
Figure 2.3: Image of the optical system with added BOS background

This schlieren setup used a sugarCUBE white LED illuminator, 30 mm condensing lens, and 127 mm diameter collimating lenses. The speckled background was fixed to the L1 collimating lens and the two lenses were 0.7 m apart. The distance from the L2 lens to the projectile centerline was 0.4 m. Therefore, the distances l and L in Figure 1.3 are 0.4 m and 0.7 m and $\frac{l}{L}$ is 0.57.

The primary data here was collected using the Photron NOVA S16. The speckled background is shown in Figure 2.4 was created using the built-in MATLAB "randi" function to create a random 512 x 512 matrix with binary values of either 0 or 1. The ones represent light regions and zeros represent dark regions for the background. The background was printed on a transparency as a 0.127 m x 0.127 m square; this size filled the entire diameter of the collimating lens and would provide light-dark regions equivalent to the sensor size of the NOVA, making each dot approximately 1 pixel wide.
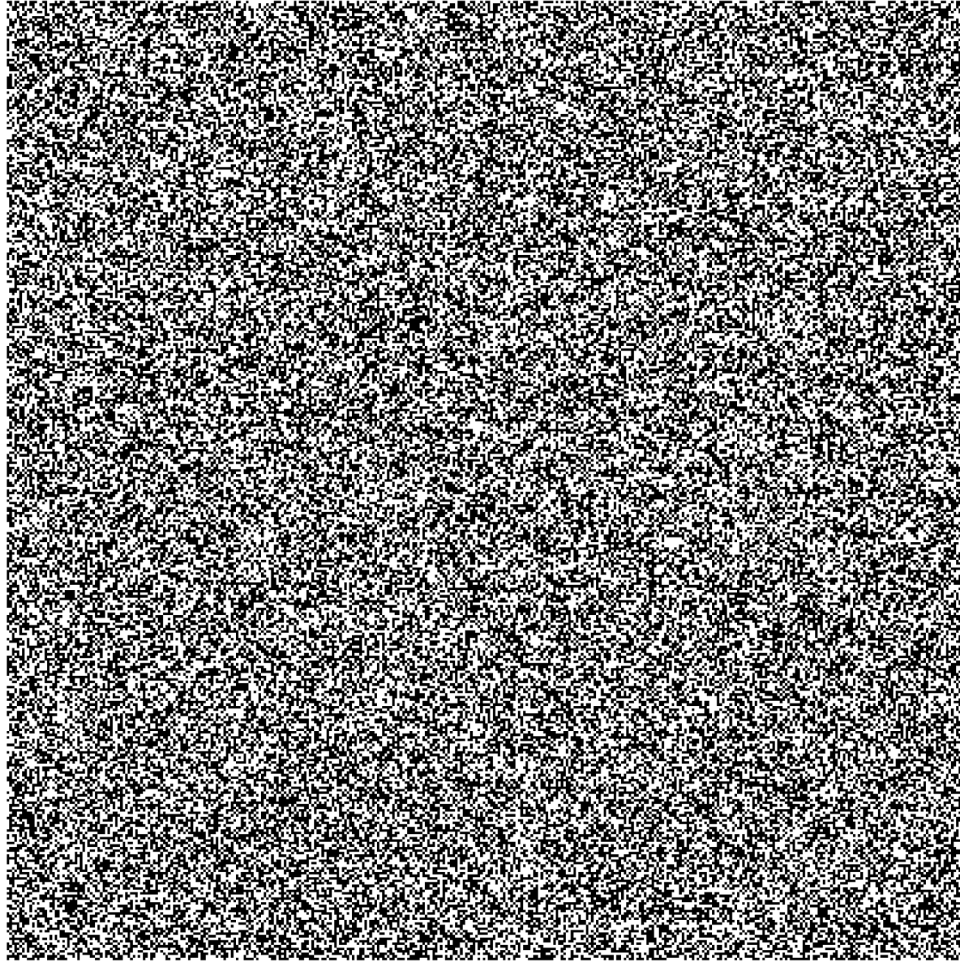
Figure 2.4: Example of the random speckled background used for the parallel light BOS data analysis. This picture is shown to size of what was printed and inserted into the test section.

2.3 Large Scale Tests

The large-scale experiments were performed at the Energetic Materials Research and Testing Center (EMRTC), located adjacent to the New Mexico Tech campus. Six tests of C4 charges were performed with charge sizes of 0.1, 1, and 10 kg. Three cameras were used to record each test, two Phantom VEO 4k 990s and one Phantom T1340; the primary camera was one of the VEO 4k 990s. Two pressure gauges (PCB model number 102A05) measured free-field pressure during each test; one was placed 3 m away from the detonation site and the other 5 m away. The locations of the cameras, pressure gauges, and detonation site are shown in Figure 2.5 and a close-up is shown in Figure 2.6.
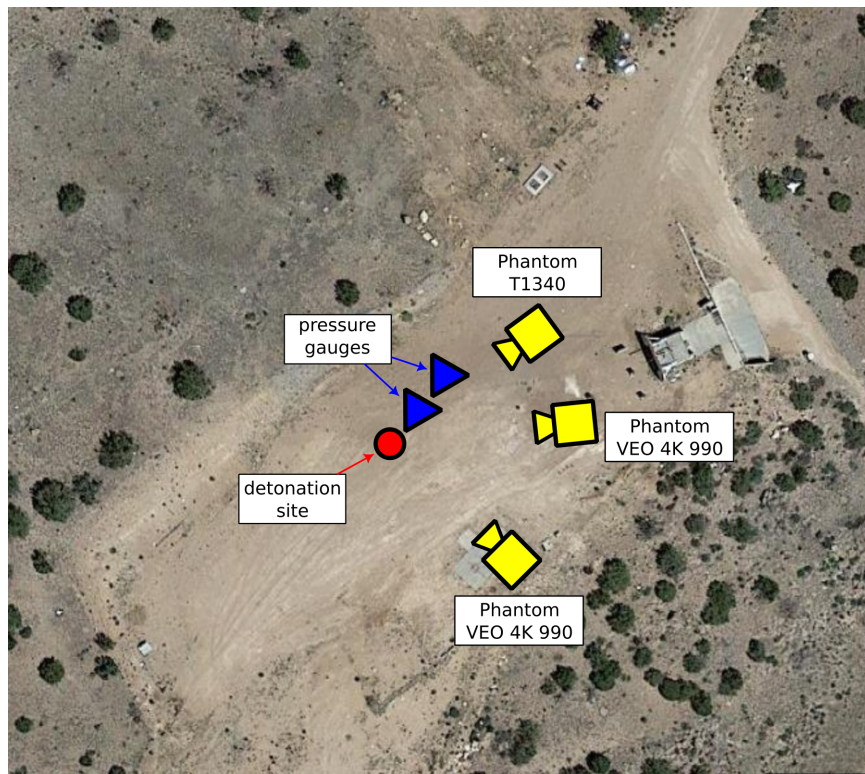
Figure 2.5: Overhead schematic of the detonation site, camera, and pressure gauge locations. The primary camera is the bottom Phantom.
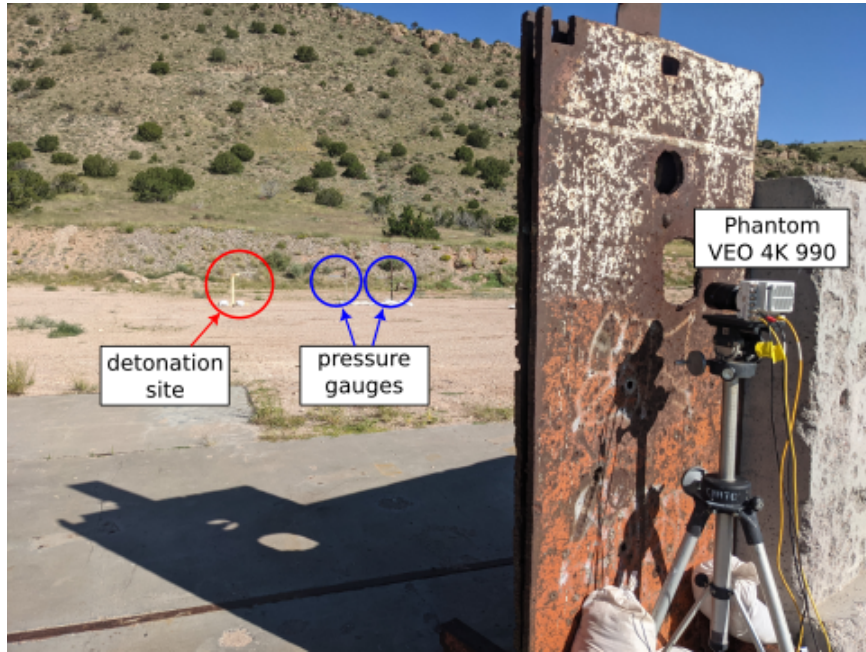
Figure 2.6: Image of the detonation site and pressure gauge locations taken near the primary camera.

Table 2.3 lists the camera settings at each location and the corresponding frame rates, the number of frames captured, and the approximate pixel-to-millimeter ratio (note that values vary slightly between each test). The natural background that was used had a two-tiered appearance; Figure 2.7 shows the two tiers. Here the two parts of the background are referred to as the "berm" and "far hill". The depth of field was set to accommodate both the detonation site and the background, but it was set to favor the berm part of the background. The distances between the camera and detonation site, background berm, and the background far hill are listed in Table 2.4. The primary data set discussed here is one of the 1kg charges.

Table 2.3: Cameras used for large scale tests with details

Camera	Frame Rate (fps)	Pixel Resolution	# of Frames	Approximate Ratio (pxl/mm)
Phantom VEO 4K 990	900	4096 x 2304	7	0.33
Phantom T1340	2700	2048 x 1952	12	0.45
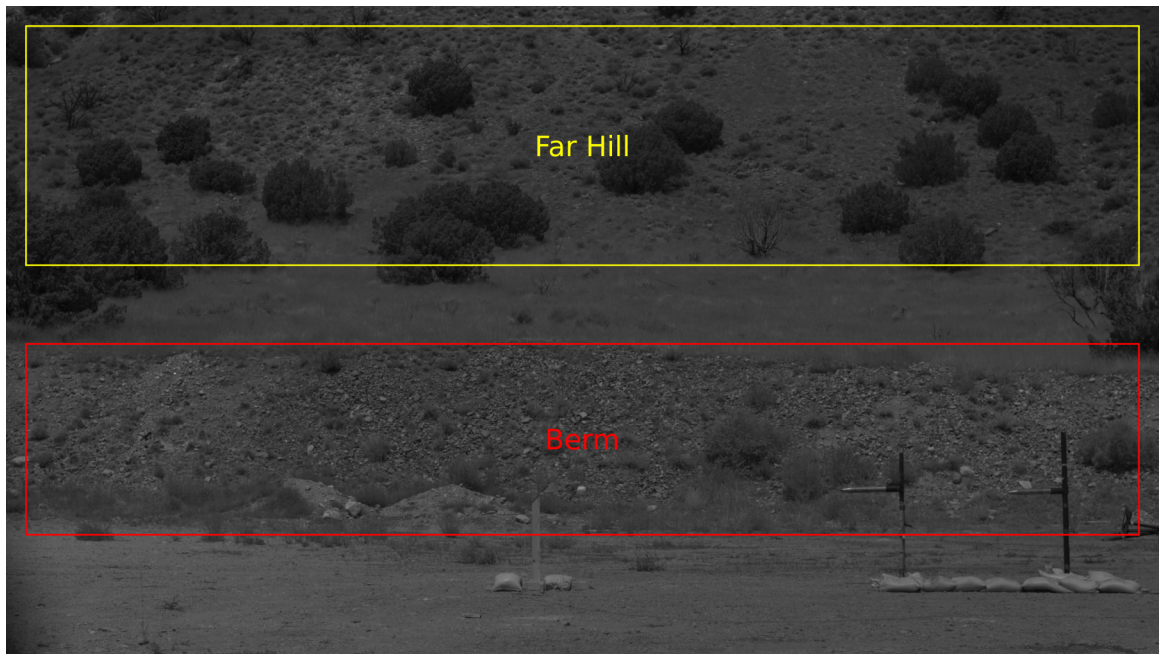
Figure 2.7: Location of the two-tiered backdrop for the large-scale BOS images. The berm-shown in red-was approximately 40 m away from the detonation site and the far hill-shown in yellow-was approximately 120 m away. There was a small slope connecting the berm and far hill which is the region between the red and yellow boxes.

Table 2.4: Large-scale test setup distances

Camera	Camera to Ground Zero (m)	Camera to Berm (m)	Camera to Far Hill (m)
1	23	49	120
2	31	96	138
3	29	98	259

2.4 Quantitative BOS

Optical flow seeks to minimize the relationship:

$$I(x, y, t) = I(x + dx, y + dy, t + dt) \tag{2.3}$$

Where I is the intensity of an image, dx and dy are the horizontal and vertical displacement, and dt is the partial time derivative between the image pairs. Here different algorithms are explored for the calculation of the intensity displacements. The HS algorithm implements a smoothness constraint to solve the intensity relationship and the LK algorithm performs a least-squares fit to solve the intensity relationship. The horizontal and vertical displacement are also known as the horizontal and vertical velocities of the flow and this is calculated at each pixel in the image.

2.4.1 Horn and Schunck Optical Flow Method

Horn-Schunck optical flow is a gradient-based algorithm for detecting the motion of light intensity between a pair of images [26]. This method implements a smoothness constraint that assumes each point has a similar displacement to its surrounding points. HS also uses a smoothing parameter α that is equal to the expected noise within the image, which minimizes the error that could occur in areas with a small brightness gradient. Here α is set to 0.05. The HS function to be minimized is described by:

$$\int_D ((\nabla I * \mathbf{v} + I_t)^2 + \alpha^2(|\nabla u|^2 + |\nabla v|^2))dxdy \tag{2.4}$$

Where ∇I is the intensity gradient, I_t is the time derivative, and $\mathbf{v}$ is the vector field of the horizontal (u), and vertical (v) displacements. To calculate the displacement, the partial derivative of brightness is first estimated at each point within the image in the horizontal (x) direction (I_x) and vertical (y) direction (I_y):

$$I_x(i,j) = \frac{1}{4}(I_{i-1,j+1,k} - I_{i-1,j-1,k} + I_{i+1,j+1,k} - I_{i+1,j-1,k} + I_{i-1,j+1,k+1}$$
$$- I_{i-1,j-1,k+1} + I_{i+1,j+1,k+1} - I_{i+1,j-1,k+1}) \tag{2.5}$$

$$I_y(i,j) = \frac{1}{4}(I_{i+1,j-1,k} - I_{i-1,j-1,k} + I_{i+1,j+1,k} - I_{i-1,j+1,k} + I_{i+1,j-1,k+1}$$
$$- I_{i-1,j-1,k+1} + I_{i+1,j+1,k+1} - I_{i-1,j+1,k+1}) \tag{2.6}$$

$$I_t(i,j) = \frac{1}{4}(I_{i-1,j-1,k+1} - I_{i-1,j-1,k} + I_{i+1,j-1,k+1} - I_{i+1,j-1,k} + I_{i-1,j+1,k+1}$$
$$- I_{i-1,j+1,k} + I_{i+1,j+1,k+1} - I_{i+1,j+1,k}) \tag{2.7}$$

Where the indices i and j represent the column and row locations of a given pixel, k, is the flow-off image, and, $k + 1$, is the flow-on image. Each i and j location is depicted in Figure 2.8 where (i,j) is the point that the gradients are calculated for.

(i-1,j-1)	(i,j-1)	(i+1,j-1)
(i-1,j)	(i,j)	(i+1,j)
(i-1,j+1)	(i,j+1)	(i+1,j+1)

Figure 2.8: Representation of the grid for calculating derivatives on point (i,j) in an image for the HS algorithm

The local averages of the flow field of a given window size. Here the window size was 3x3 so the local averages are defined as:

$$\bar{u}_{i,j,k} = \frac{1}{6}(u_{i-1,j,k} + u_{i,j+1,k} + u_{i+1,j,k} + u_{i,j-1,k})$$
$$+ \frac{1}{12}(u_{i-1,j-1,k} + u_{i-1,j+1,k} + u_{i+1,j+1,k} + u_{i+1,j-1,k} \tag{2.8}$$

$$\bar{v}_{i,j,k} = \frac{1}{6}(v_{i-1,j,k} + v_{i,j+1,k} + v_{i+1,j,k} + v_{i,j-1,k})$$
$$+ \frac{1}{12}(v_{i-1,j-1,k} + v_{i-1,j+1,k} + v_{i+1,j+1,k} + v_{i+1,j-1,k} \tag{2.9}$$

Where $\bar{u}$ and $\bar{v}$ are the horizontal and vertical average flow fields. Finally, the best flow velocity estimation is found by iterating the equation:

17

$$u_{new} = \bar{u}_{old} - \frac{I_x(I_x\bar{u}_{old} + I_y\bar{v}_{old} + I_t)}{\alpha^2 + I_x^2 + I_y^2} \tag{2.10}$$

$$v_{new} = \bar{v}_{old} - \frac{I_y(I_x\bar{u}_{old} + I_y\bar{v}_{old} + I_t)}{\alpha^2 + I_x^2 + I_y^2} \tag{2.11}$$

Where *new* represents the next iteration value and *old* is the previous iteration values. This equation is iterated until the maximum iteration is reached or the minimum error is satisfied. In this case, HS recommends the maximum iteration be equivalent to the pixel width of the image; the minimum error is desired to be 10^{-6} [26]. The error is calculated using:

$$error = \sqrt{(u_{new} - u_{old})^2 + (u_{new} - u_{old})^2} \tag{2.12}$$

2.4.2   Lucas and Kanade Optical Flow Method

LK is different from HS because it uses a least squares approximation for analyzing the displacement. The LK quantity to be minimized is described by:

$$\sum W^2(\nabla I \cdot \mathbf{v} - I_t)^2 \tag{2.13}$$

Where ∇I is the intensity gradient, $\mathbf{v}$ is the flow field made up of the horizontal (u) and vertical (v) displacements, I_t is the time derivative, and W is a weighted window function. The weighted function W can be used to give points closer to the center of the window more influence. The weighted window was not used in this implementation of LK because it was not found to improve the results.

The solution to Equation 2.13 is given by:

$$C^T C\mathbf{v} = C^T\mathbf{b} \tag{2.14}$$

Which can be simplified into:

$$\mathbf{v} = (C^T C)^{-1}C^T b \tag{2.15}$$

where,

$$C = (\nabla\mathbf{I}(x_1), ..., \nabla\mathbf{I}(x_n))^T \tag{2.16}$$

$$b = -(\mathbf{I}_t(x_), ..., \mathbf{I}_t(x_n))^T \tag{2.17}$$

$\nabla\mathbf{I} = (I_x, I_y)$ and includes all the points within the given window indexed (x_1-x_n) as a column matrix and $\mathbf{v} = (u, v)^T$. The window size can be changed by

increasing the radius (w) of the window. Figure 2.9 shows a visual representation on how w affects the window size.

(i-w,j-w)	...	(i,j-w)	...	(i+w,j-w)
⋮	⋱	⋮	⋰	⋮
(i-w,j)	...	(i,j)	...	(i+w,j)
⋮	⋰	⋮	⋱	⋮
(i-w,j+w)	...	(i,j+w)	...	(i+w,j+w)
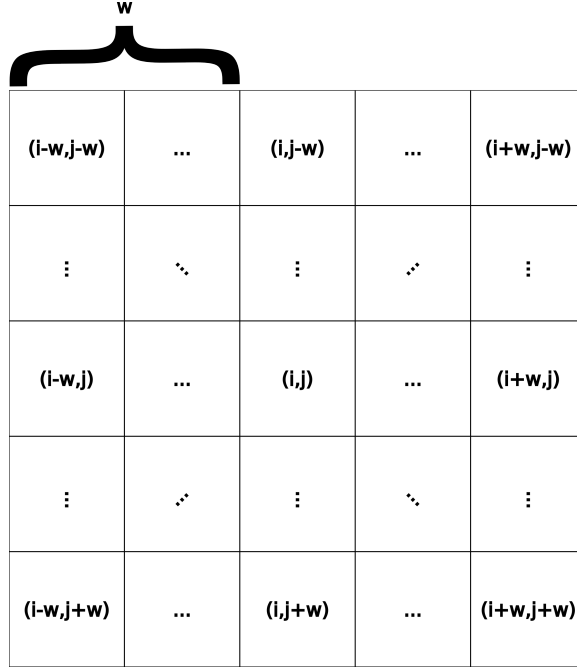
Figure 2.9: Visual of the LK window and how the window radius, w, affects the overall window size

Here the window radius is 2 with an overall window size of 5 x 5. The intensity gradient is calculated using a 2D convolution with a specified kernel (K) defined by [23]:

$$K = \frac{1}{12}(-1, 8, 0, -8, 1) \tag{2.18}$$

and the time gradient is calculated with:

$$I_t(i, j) = I_{k+1}(i, j) - I_k(i, j) \tag{2.19}$$

To minimize unreliable displacement estimates, a modification to LK introduced by Simoncelli et. al. [32] and suggested by Barron et. al. [23] was implemented. The modification minimizes unreliable estimates by finding the eigenvalues of $C^T C$ and setting a threshold value, τ, so that if both eigenvalues are greater than τ, the displacement is found using Equation 2.15. If only one of the eigenvalues are less than τ then the image gradient is normalized to find the displacements, and if both eigenvalues are less than τ the displacement is set to zero. This modification was used in this implementation of LK.

2.5 Density Reconstruction

The output of the optical flow algorithms is the horizontal and vertical displacements, and magnitude displacement in pixels. The displacements are to be related to refractive index and, ultimately, density variations. For the small-scale tests, the vertical displacement was used to calculate density, and, for large-scale tests, the horizontal displacement was used. The first step was to convert the pixel displacement to a physical displacement value. To do this, a calibration object with a known size was imaged to create a pixel-to-distance ratio for each test. Figure 2.10 shows the calibration objects used for each test. The small-scale test calibration object was a small calibration lens (the same one that is used for correlating refractive index to intensity in schlieren) with an outer diameter of the lens holder (outer diameter of the black ring in Figure 2.10) equal to 0.045 m. The large-scale calibration object was a board with a 0.127 m grid, that was held up parallel to the camera and in line with the detonation location. The pixel ratio is calculated with the relationship:

$$\text{ratio} = \frac{dx_{pixels}}{dx_{physical}} \tag{2.20}$$
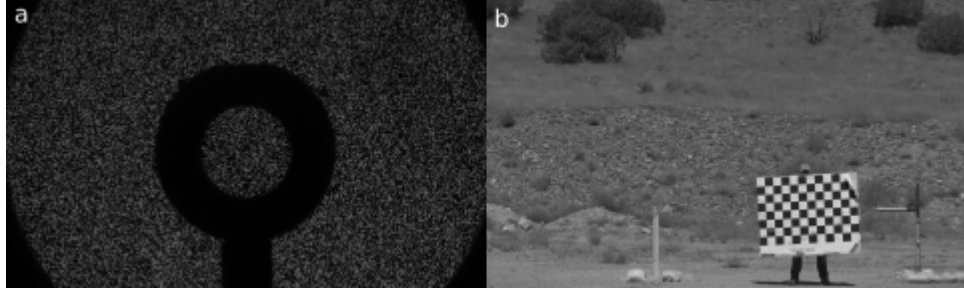
Figure 2.10: Calibration objects to convert displacement units from pixels to meters. a) is the small-scale calibration lens with an outer diameter of 0.0198m, and b) is the large-scale calibration board with a 0.127m grid

The displacement in meters was calculated by dividing the displacement in pixels by the pixel-to-meter ratio:

$$\mathbf{v} = \begin{bmatrix} u \\ v \end{bmatrix}_{\text{m}} = \frac{\begin{bmatrix} u \\ v \end{bmatrix}_{\text{pixel}}}{\text{ratio}} \tag{2.21}$$

Next, using the l and L distances shown in Figure 1.3 the displacement values were converted to a refraction angle in radians, ε:

$$\varepsilon = \arctan(\frac{u_{\text{m}}}{L - l}) \tag{2.22}$$

$$\varepsilon = \arctan\left(\frac{v_{\mathrm{m}}}{L-l}\right) \tag{2.23}$$

The refractive angle, ε, was then converted to a refractive index ratio, δ, using the two-point Abel inversion process [33] with the following equations for each radial point, r_i:

$$\delta(r_i) = \sum_{j=i}^{N+1} D_{i,j}\varepsilon_j \tag{2.24}$$

$$D_{i,j} = \begin{cases} \frac{1}{\pi}(A_{i,j} - A_{i,j-1} - jB_{i,j} + (j-2)B_{i,j-1}), & \text{if } j > i \text{ and } j \neq 2 \\ \frac{1}{\pi}(A_{i,j} - jB_{i,j} - 1), & \text{if } j > i \text{ and } j = 2 \\ \frac{1}{\pi}(A_{i,j} - jB_{i,j}), & \text{if } j = 1 \text{ and } i = 1 \\ 0, & \text{if } j = i = 1 \text{ or } j < i \end{cases} \tag{2.25}$$

$$A_{i,j} = \sqrt{j^2 - (i-1)^2} - \sqrt{(j-1)^2 - (i-1)^2} \tag{2.26}$$

$$B_{i,j} = \ln\left(\frac{j + \sqrt{j^2 - (i-1)^2}}{(j-1) + \sqrt{(j-1)^2 - (i-1)^2}}\right) \tag{2.27}$$

$$\delta(r_i) = \frac{n(r_i)}{n_0} - 1 \tag{2.28}$$

The Abel inversion requires that the refractive field from the shock-front all the way to the axis of symmetry be analyzed. This means, for the ballistic tests, the shock-edge to the centerline of the projectile is processed, and, for the C4 tests, the shock-edge to the detonation site is processed. The refractive index was then converted to density, ρ, using the Gladstone-Dale law:

$$n(r_i) = \kappa\rho(r_i) + 1 \tag{2.29}$$

Where the Gladtone-Dale coefficient for air, $\kappa = 2.23 * 10^{-4}\frac{\mathrm{m}^3}{\mathrm{kg}}$, is used. The density reconstruction for the small-scale test was then related back to the schlieren density reconstruction. The schlieren density reconstruction was calculated in the same manner listed here, except that the ε was calculated using the intensity variation inside the calibration lens shown in Figure 1.2 [21, 31]. This density comparison is the final step for the small-scale experiments, but the large-scale experiments are compared back to pressure-gauge data so further steps are required.

Before the large-scale density reconstruction can be converted to pressure using the Ideal Gas Law, the temperature profile was determined. The temperature profile was assumed to follow the model described by Tobin and Hargather

[34], where the temperature peaked at the shock front and then linearly decayed back down to atmospheric temperature in the time that the density and pressure profile decayed back to atmospheric conditions. This time was estimated using the pressure profile measured with the pressure gauges.

To estimate the peak temperature at the shock front, the velocity of the shock wave was estimated using the change in shock location between two consecutive frames of the high-speed videos. The estimated shock velocity (v_{shock})can then be converted to Mach number (M):

$$M = \frac{v_{shock}}{\sqrt{\gamma R T_1}} \tag{2.30}$$

Where the heat capacity ratio (γ) is 1.4, the gas constant (R) is 287($\frac{J}{kg \cdot K}$), and T_1 is the atmospheric temperature. With M, the ratio between peak temperature T_2 and atmospheric temperature was found from one-dimensional gas dynamic relationships:

$$\frac{T_2}{T_1} = \frac{(1 + \frac{\gamma-1}{2}M^2)(\frac{2\gamma}{\gamma-1}M^2 - 1)}{M^2(\frac{2\gamma}{\gamma-1} + \frac{\gamma-1}{2})} \tag{2.31}$$

$$T_2 = \frac{T_2}{T_1}T_1 \tag{2.32}$$

The density and temperature profile was converted to a function of time by dividing the radial distance by the found shock velocity, which assumes the velocity of the shock was constant throughout the duration of the event [34]. Finally, the Ideal Gas Law was used to determine the pressure profile behind the shock front:

$$P(t_i) = \rho(t_i)RT(t_i) \tag{2.33}$$

The calculated temporal pressure was compared back to the pressure-gauge data, which gave a good representation of the effectiveness of OF techniques for large-scale tests.

CHAPTER 3

SMALL-SCALE RESULTS

The small-scale tests visualized the refractive field around a 10° half angle conical projectile. The high-speed images are processed through each of the OF codes to quantify the density fields. The results are compared between methods and to quantitative schlieren as a baseline.

3.1 Optical Flow Processing

The BOS images were recorded with the Photron NOVA S16 at 30,000 fps and with a 1024 x 512 resolution. The flow-off and flow-on images used for analysis are shown in Figure 3.1. Both the background and projectile could not be in focus, so the background was prioritized, causing the projectile to be slightly out of focus. To identify the body of the cone during analysis, a mask was applied to the flow-on image so that the cone edge could be detected. The image had an actual pixel-to-millimeter ratio of 7.48 pxl/mm.
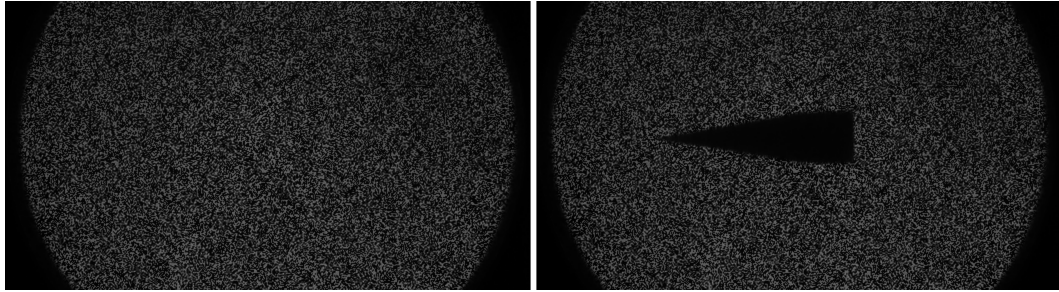
Figure 3.1: The flow-off and flow-on images that each OF method will process. The flow-off image is on the left and the flow-on image is on the right.

The output of the OF methods are the measured intensity shifts in the horizontal and vertical direction between the image pair shown in Figure 3.1. The calculated horizontal and vertical displacement at each pixel are represented as a colored array that correlates the displacement to a specific color on the colorbar. The magnitude of the displacement was also calculated using:

$$a = \sqrt{u^2 + v^2} \tag{3.1}$$

where a is the magnitude, and u and v are the horizontal and vertical displacements respectively. The magnitude displacement can also be displayed using the colored array method. To represent both the magnitude and direction of each displacement value, a quiver plot can be used which displays the magnitude and direction of the OF displacement field using red arrows. The output of the OF methods using these visuals are shown in Figure 3.2.
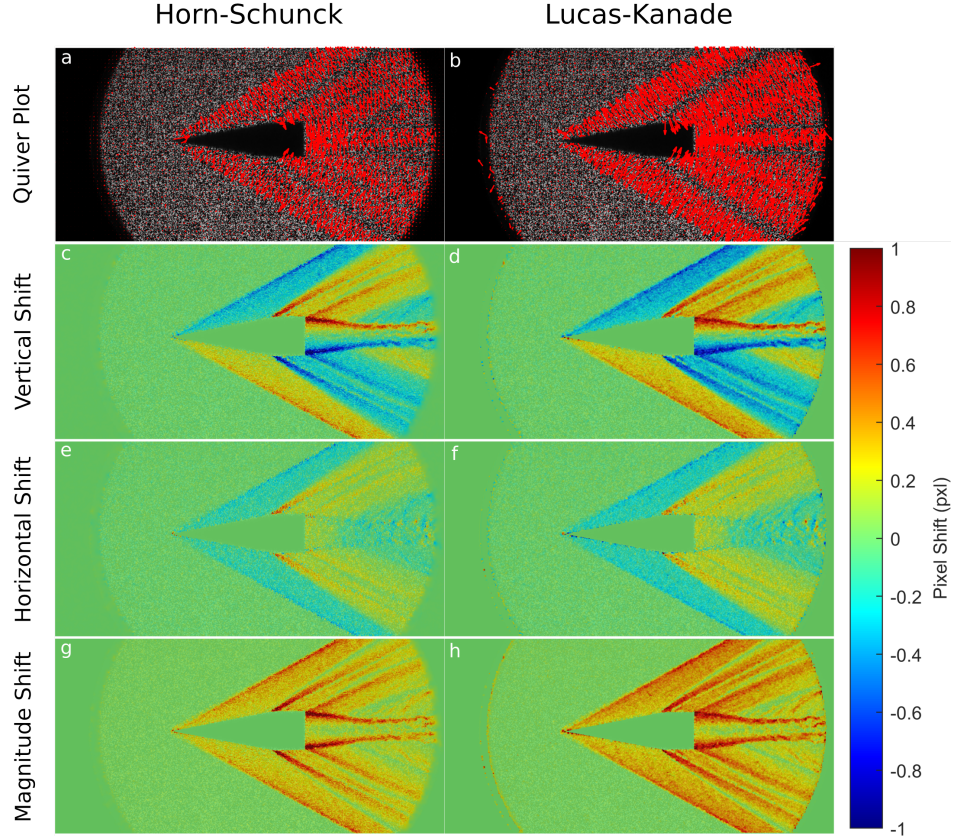
Figure 3.2: Results from the HS and LK OF algorithms. The left column (images a,c,e,g) are the results from the HS method and the right column (images b,d,f,h) are the results from the LK method. Images (a) and (b) show the quiver plots, (c) and (d) show the horizontal displacement, (e) and (f) show the vertical displacement, and (g) and (h) show the magnitude displacement

The OF vertical displacement is equivalent to a schlieren system with a horizontal knife edge as it shows the vertical gradient inside the image, and the horizontal displacement is equivalent to a vertical knife edge which shows the horizontal gradient. The measured displacements for each method range between -1 to 1 pixel. The vertical displacement contour image shows the radial lines associated with conical flows in more detail than the horizontal displacement which is expected based on the geometry and projectile velocity here. For the present

work the vertical displacement is of primary interest. The vertical displacement results of each method appear to be very similar, however, it is noticeable that LK detects a larger pixel shift than HS, especially at the shock boundary. To investigate this further, the numeric values of the vertical pixel shifts were compared.

3.2   Background Noise Characterization

The background regions outside of the bullet shock flow field are generally uniform in calculated background displacement. The variation in displacement calculated in these undisturbed regions represents a background noise in the system which must be characterized to define a baseline minimum refraction that can be observed. This noise represents an overall noise in the system which may be due to small ambient atmosphere disturbances along the optical path or numerical noise in the OF calculations. To measure the background noise from each method, a pre-shock region with no disturbance was selected and the displacement values within that region were plotted. The region of interest is illustrated by the red square in Figure 3.3 and the vertical displacement distribution inside the pre-shock region are plotted in Figure 3.4.
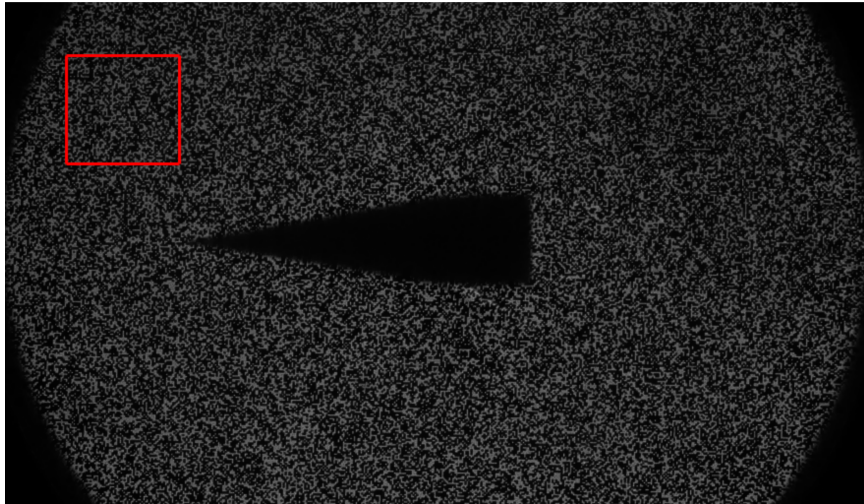
Figure 3.3: The background characterization was performed in the image region contained in the red box, which is expected to be undistorted background.
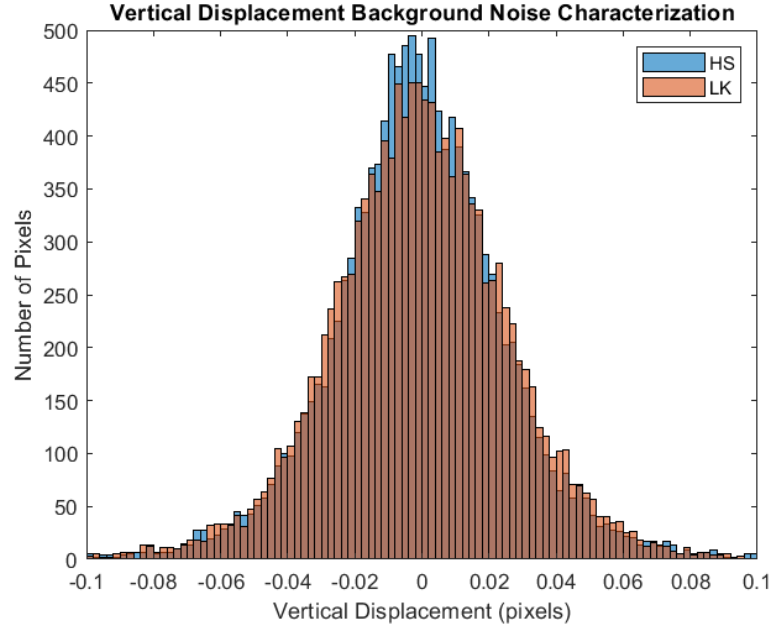
Figure 3.4: Histogram of the calculated vertical displacements in the undisturbed background region. The Horn-Schunck characterization is in blue and the Lucas-Kanade characterization is in red.

The plot shows a normal distribution of the measured displacements. The average displacement in the pre-shock region was 0 pixels with a standard deviation of ± 0.0249 pixels for both methods, indicating random, Gaussian-distributed noise. While only the vertical background noise is shown here, the horizontal displacement still had the same distribution, once again showing random noise.

3.3 Pixel Displacement Analysis

The post-shock region was characterized to compare the average vertical displacement that each algorithm measured. To do this, the shock position needed to be located to ensure only the post-shock region was characterized. To locate the shock boundary, the flow-on image, shown in Figure 3.1, was subtracted from the flow-off image. This is a simple background subtraction method that identifies any changes between the image pairs. A 0.5 shift was added to the histogram of the background subtracted image so that areas with no change are represented as the 50% gray regions, this shift better visualizes the changes in the image. Image (a) of Figure 3.5 shows the shifts between the images with this process. Next, the built-in Matlab "edge" function was used to define the boundary further; detected edges were represented by the white regions in image (b) of Figure 3.5. A line was then manually fit to the shock boundary as shown in Figure 3.6. This line along the shock front represents the top of the region of interest for the density analysis. The region then extends vertically downward to the cone surface

and from the tip of the cone to the end of the $10°$ cone section since this is the only region that will be compared. The final region for the post-shock analysis is shown in Figure 3.7.
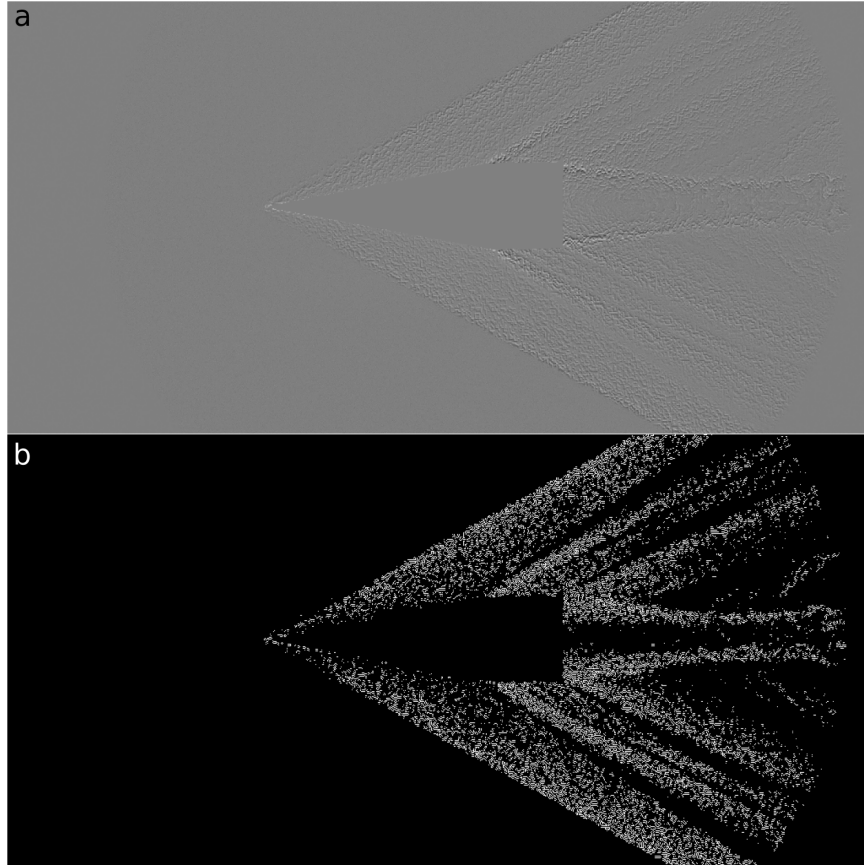
Figure 3.5: Image (a) shows the result of the simple image subtraction process and image (b) shows the result of applying the built-in "edge" function in Matlab to image (a). The white regions in (b) show the location where an edge was detected and the black shows the regions where no edge was detected. This process allows for the shock-edge to easily be located.

Figure 3.6: Background subtracted image with the found shock edge shown in red.
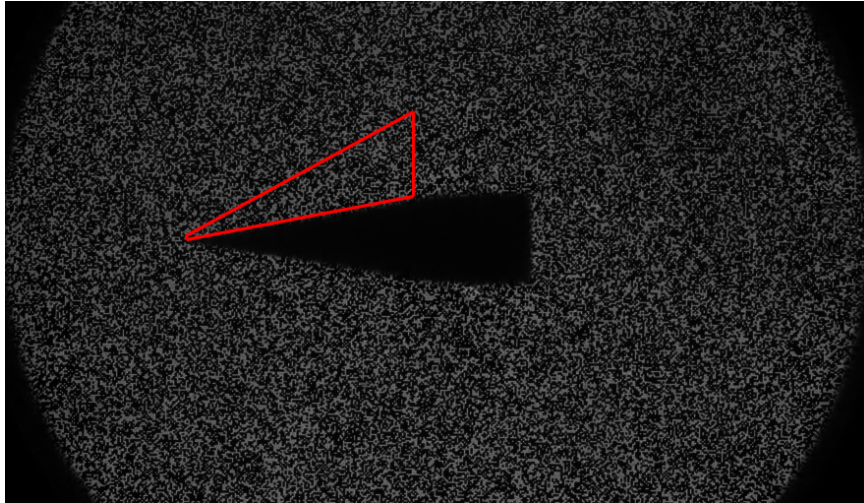
Figure 3.7: Visualization of the region of interest for the post-shock comparison of each algorithm.

The vertical displacement distribution inside the post-shock region was plotted in the same manner as Figure 3.4 and is shown in Figure 3.8. The HS method measured an average vertical displacement of 0.23 pixels, whereas the LK method measured an average vertical displacement of 0.29 pixels with a standard deviation of $\pm$ 0.1187 pixels. The calculated displacements vary between the methods because of the different constraints that each method applies to the intensity assumption, for HS applies a global smoothness constraint, and LK applies the least squares fit. The LK method detected a larger pixel shift on average than the HS method which, according to Equation 2.23, will lead to a larger refractive angle ε and therefore a larger density measurement. With this characterization, it is expected that LK will lead to a higher-valued density reconstruction than HS.
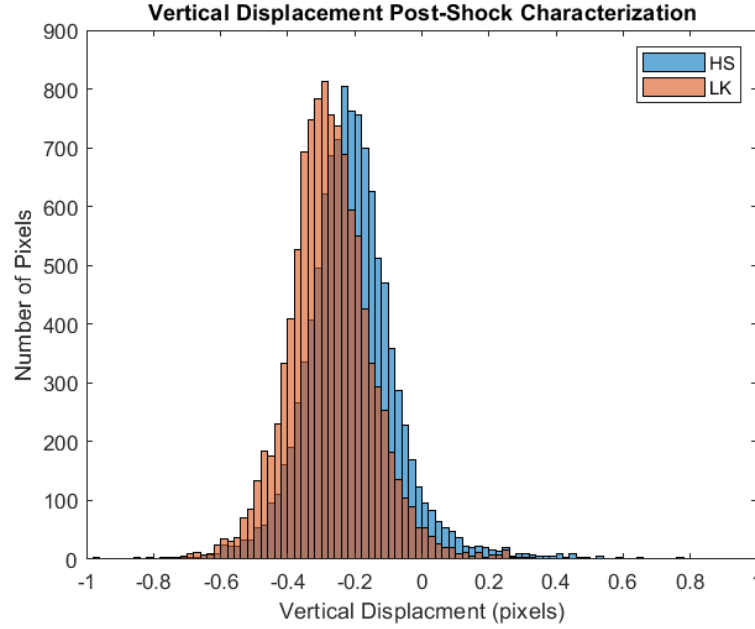
Figure 3.8: Histogram of the calculated OF vertical displacement in the post-shock region. The Horn-Schunck characterization is in blue and the Lucas-Kanade characterization is in red. The two OF methods result in different calculated pixel displacements as evident by the difference in the histograms.

The displacement values were further analyzed by comparing pixel columns of the image at different locations along the cone. The locations were 1.16 cm (400 pixels), 2.23 cm (470 pixels), and 3.3 cm (550 pixels) from the tip of the cone, as shown in Figure 3.9. The line plots of the OF vertical displacements for each of these locations are shown in Figure 3.10. The shock edge location determined earlier from the simple background subtraction process is shown in each plot as a vertical black dashed line. The background noise threshold, defined as the standard deviation of the OF methods from Figure 3.3, is represented by the two horizontal gray dotted lines. Figure 3.10 shows that the displacement values increase linearly from the cone surface to the shock edge. At the shock wave edge, the displacement values do not depict an instantaneous jump, but rather as a gradient in pixel displacement which has some spread or width. Table 3.3 lists the pixel location for where each OF method crosses the standard deviation boundary, where there is an identified peak, and where the location of the shock wave is as identified by the background subtraction process.
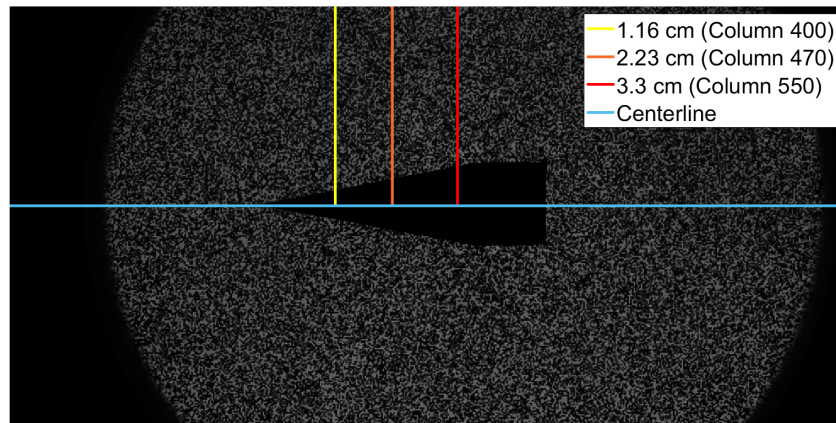
Figure 3.9: Location of the line plots compared. Column 400 is at 1.16 cm from the cone tip, Column 470 is at 2.23 cm, and Column 550 is at 3.3 cm. The blue line depicts the centerline of the projectile.
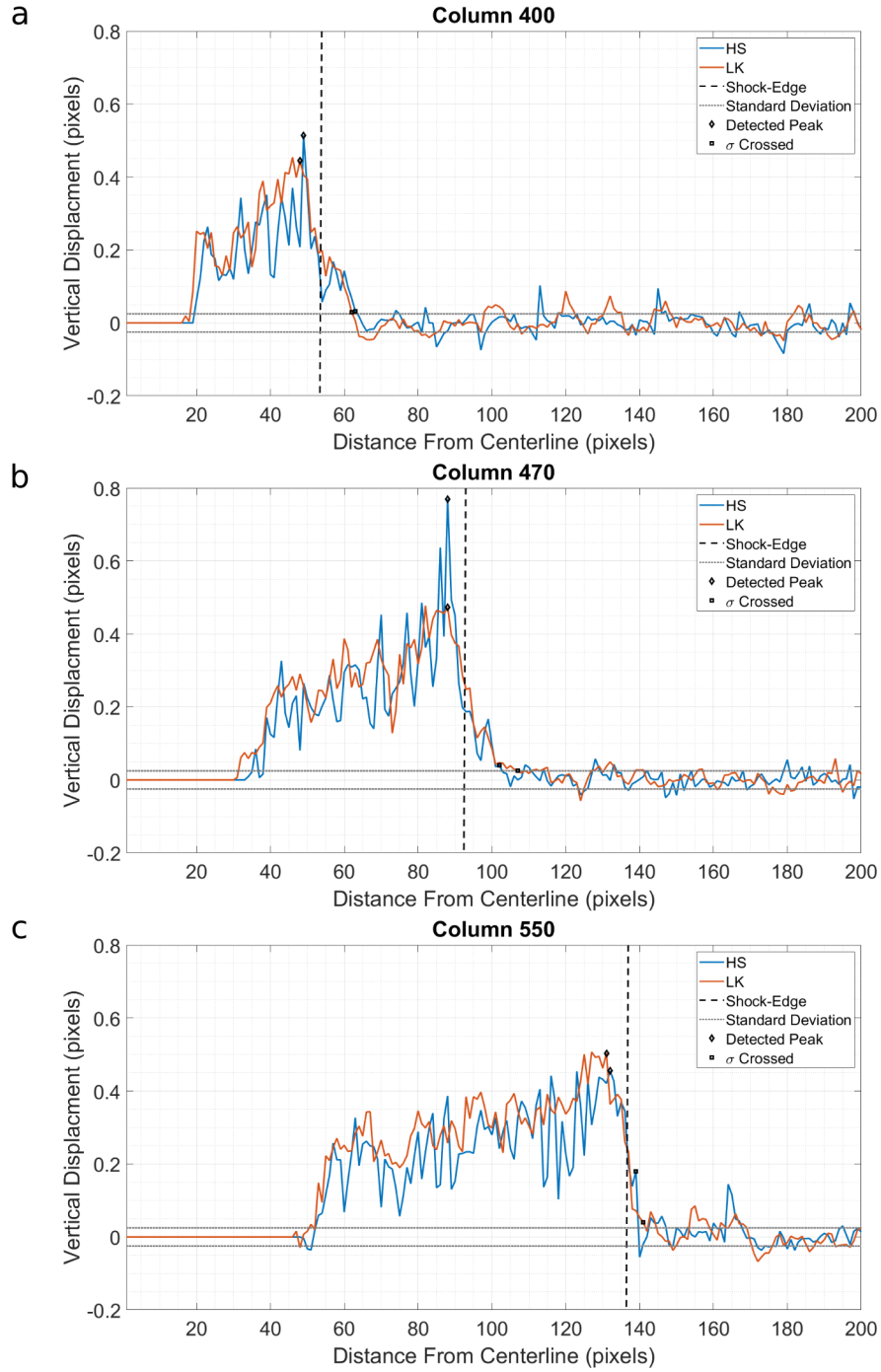
Figure 3.10: Line plot of the LK and HS displacement values. HS is shown in blue, LK is shown in red, the expected shock wave location is shown as a black vertical line, and the standard deviation is represented by the horizontal gray dotted lines.

Table 3.1: HS and LK shock detection location in pixels from the cone centerline

		HS		LK	
Location on Cone (cm)	Shock Location (pix)	σ Crossed (pix)	Peak (pix)	σ Crossed (pix)	Peak (pix)
1.16	54	63	49	62	48
2.23	93	102	88	107	88
3.3	136	139	132	141	131

Both OF results cross the standard deviation threshold before the expected shock edge and then reach the peak displacement after the expected shock edge. The LK method typically crossed the standard deviation threshold 1-3 pixels sooner than HS. On average, the effective shock "width" from when the noise threshold is crossed to when the OF detected the peak displacement is about 11.7 pixels for HS and 13.7 pixels for LK. The HS method analyzes a 3 x 3 pixel neighborhood for each point in the image, and the LK method analyzes a 5 x 5 pixel neighborhood, so it is logical to attribute the larger width in the LK method to the larger neighborhood size. However, the shock width is not just a factor of the OF analysis. In Falls' Thesis [31], he found that the schlieren images of these projectiles also detected a certain thickness or width to the shock edge. Therefore it is reasonable to say that the BOS images are also detecting the same shock width with the addition of the OF causing additional width.

To further visualize the apparent shock width, the simple background intensity differences at 3.3 cm (Column 550) were plotted and it is evident that there is a gradient in the intensity difference, which does suggest a shock thickness approximately 6 pixels wide. From Kinney and Graham [35] the actual thickness of a shock wave defined as the distance from the atmospheric density to the peak density after the shock, is approximately 0.225 μm for a shock velocity of 453 m/s. The 6-pixel "width" here represents 1.4 mm with this image resolution. The shock "width" here is not the actual physical thickness of the shock, but an apparent thickness over which the density rise is observed or calculated based on the optical arrangement and the optical flow processing.
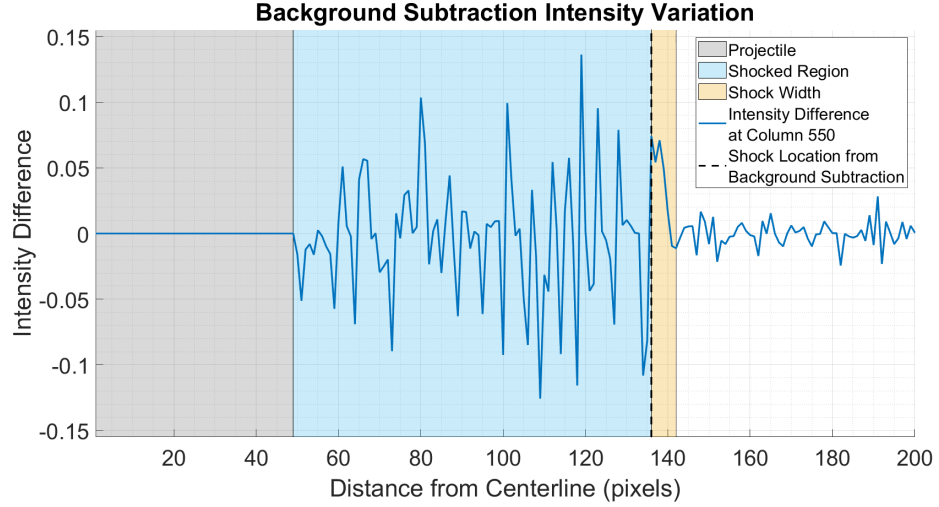
Figure 3.11: The intensity variation from the background-subtracted image at 3.3 cm from the cone tip. The gray region shows where the projectile is, the blue region shows the shocked flow, and the yellow region shows the shock width. The intensity variation line plot also depicts a shock width associated with the data set.

Each method is influenced by the neighborhood of pixels being analyzed for each location, so, to determine if the peak location and value of the vertical displacement could be resolved better, a mask was applied to the data set so only the post-shock location was processed through OF. The comparison between the OF results with and without the masked-out region is shown in Figure 3.12. Masking out the pre-shock region did not improve the ability of either method to detect the shock edge closer to the expected shock location. There is a slight variation in the peak displacement value measured, but it is not significant and the displacement values after the peak match exactly. Because there was not much improvement in the displacement values by masking the pre-shock region, this was not implemented in further processing and the displacement values without the mask were used to calculate density.
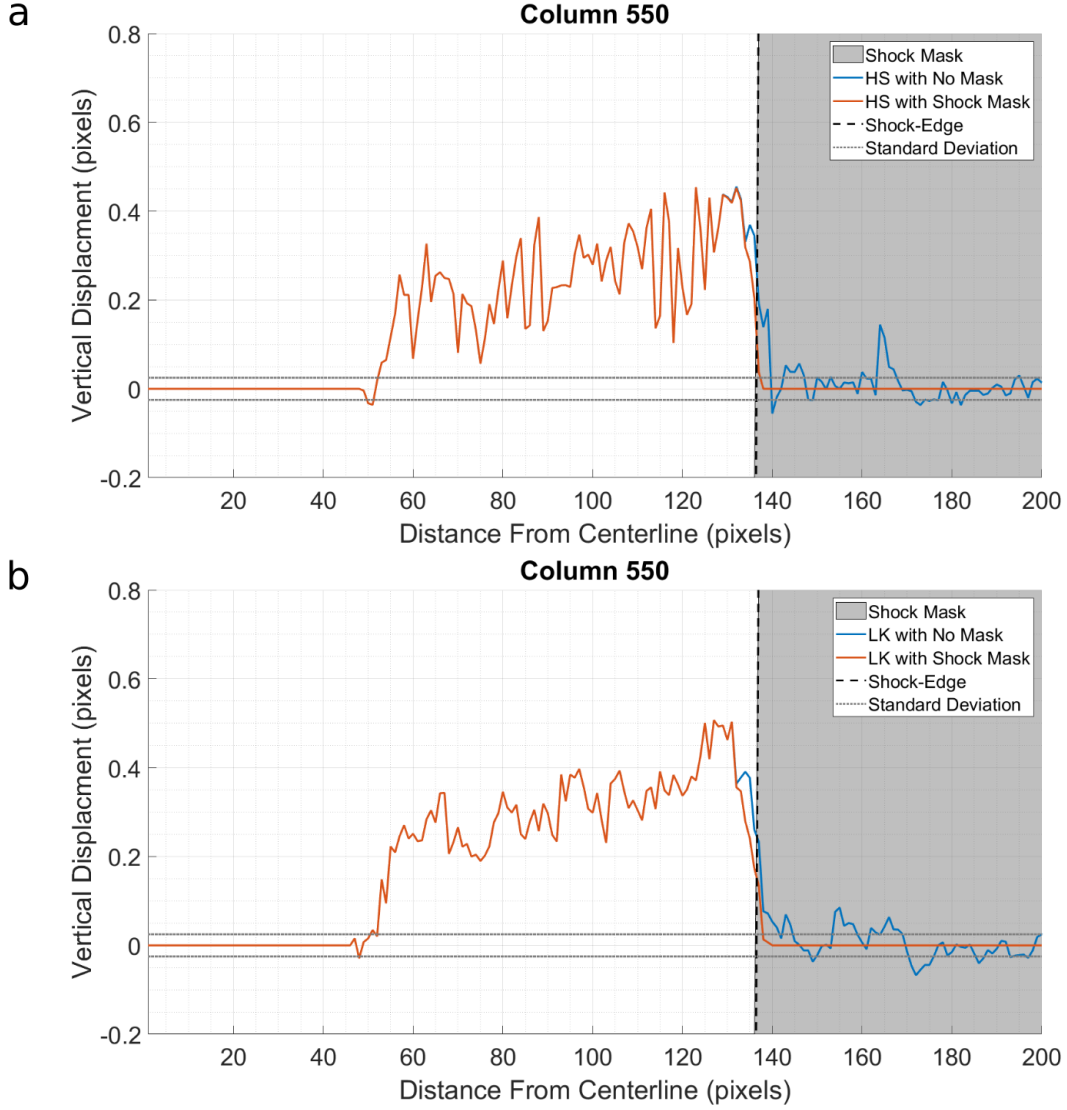
Figure 3.12: Line plot comparison of the effects of masking out the pre-shock region for HS and LK OF.

3.4 Density Reconstruction

The OF vertical pixel displacement values were converted to displacement in meters using Equation 2.21, and then the refraction angle was calculated using Equation 2.22. With the atmospheric conditions listed in Table 3.4, the Abel inversion process (Equations 2.24-2.28) was used to determine the density field around the top half of the cone. Figures 3.13 and 3.14 show the density reconstruction of the HS and LK data.

Table 3.2: Atmospheric conditions when the BOS test images were captured.

Atmospheric Pressure (kPa)	Atmospheric Temperature (K)	$\frac{Pixel}{mm}$
84.79	293	7.48

HS Density Reconstruction
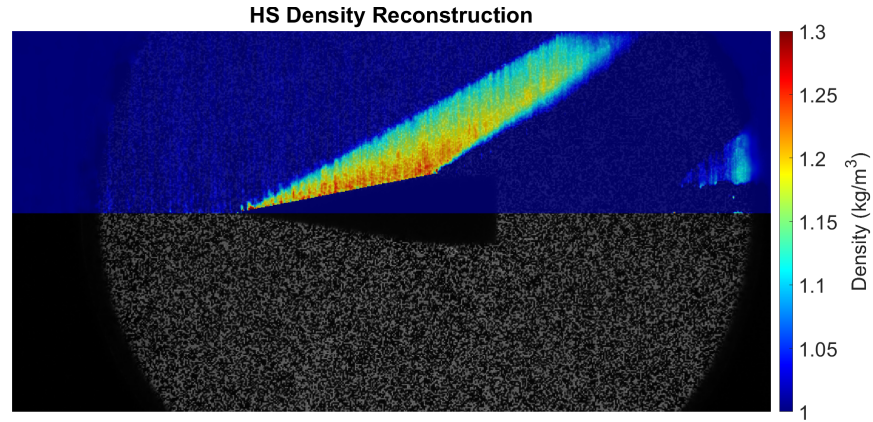
Figure 3.13: Density reconstruction of the top half of the conical projectile derived from the HS OF method. The bottom half of the image is left as the flow-on image for comparison.

LK Density Reconstruction
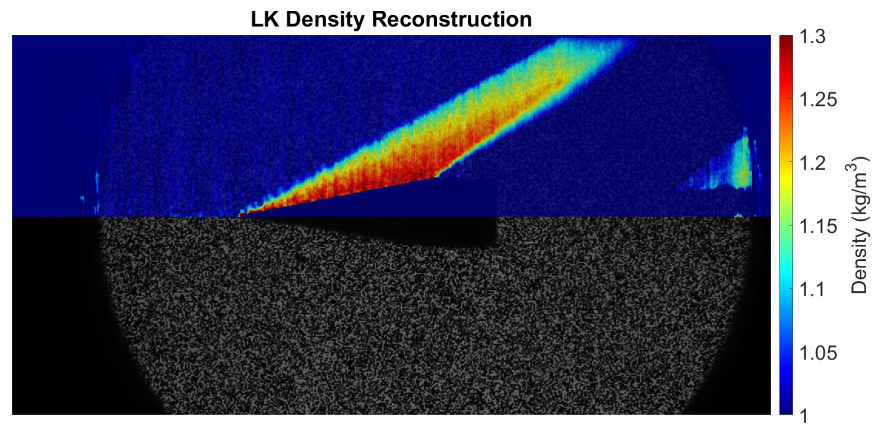
Figure 3.14: Density reconstruction of the top half of the conical projectile derived from the LK OF method. The bottom half of the image is left as the flow-on image for comparison.

Figure 3.15 shows the line plots of the HS and LK density reconstruction at 3.3 cm from the cone tip plotted together. The theoretical density profile was calculated using the theoretical Taylor Maccoll profile and is shown in the Figure as the yellow line. As expected, the LK method resulted in a larger density profile than the HS method, but the HS method results in density values closer to the theoretical line. To examine individual radial profiles along the cone length, the density data was normalized for a radius from 0 to 1, where 0 is the cone surface and 1 is the free-stream boundary. The normalized HS-derived density profile is shown in Figure 3.16 and the LK-derived density profile is shown in Figure 3.17. The plots show the density profile extracted from incremental locations along the $10°$ section of the cone, where the location 3.3 cm away from the cone tip is highlighted in blue for HS and red for LK.
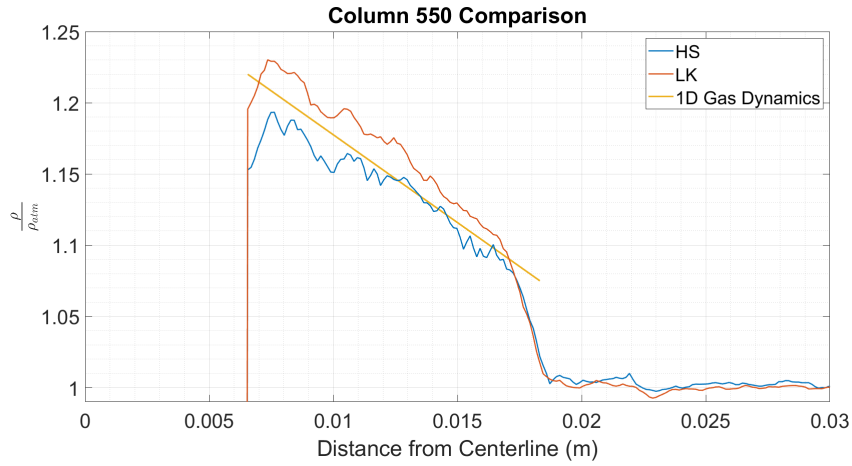
Figure 3.15: Comparison of the OF derived density reconstruction at 3.3 cm away from the cone tip. The blue line depicts the HS-derived data and the red line depicts the LK-derived data. The centerline of the cone is at $x = 0m$, the cone surface is at approximately $x = 0.0065m$, and the free-stream/shock wave boundary is at approximately $x = 0.0182m$.
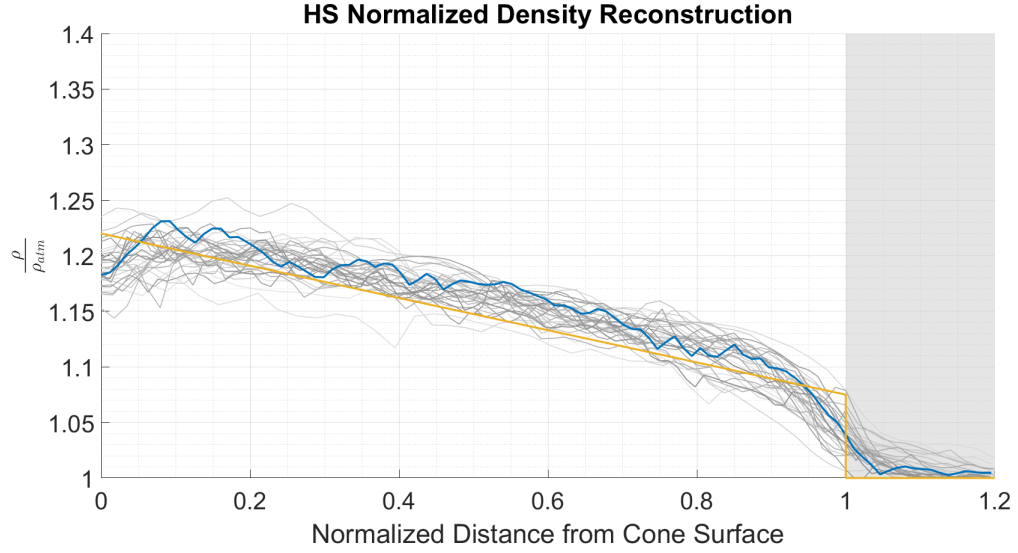
Figure 3.16: Comparison between the HS displacement values without the pre-shock region masked out and with the pre-shock region masked.
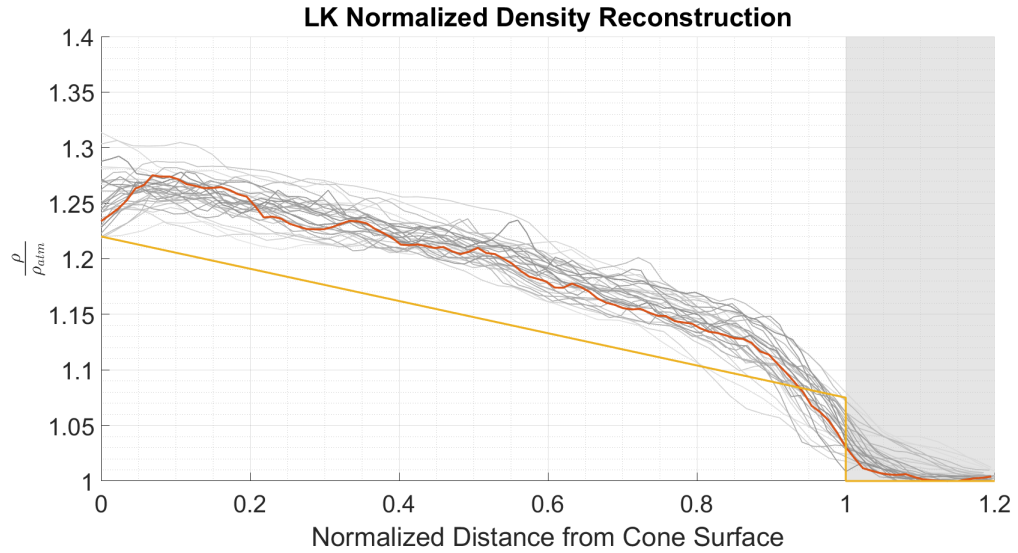
Figure 3.17: Comparison between the LK displacement values without the pre-shock region masked out and with the pre-shock region masked.

Figure 3.15 shows that the density increased from the atmospheric density across the shock wave boundary ($x = 0.01825m$) and then linearly increased closer to the cone surface ($x = 0.007m$). The decrease in density at the cone surface is not physically resolved but is rather the result of the projectile being out of focus. This trend follows 1D gas dynamic relationship for a conical shock as

Taylor Maccoll suggests in his solution for supersonic flow over a cone [36]. The slope of each line was also determined and are listed in Table 3.3. To calculate the slope, the data points between 0.1 and 0.9 of the normalized distance were used so only the linear portion of the data was considered. As shown in the table, the HS method results in a slope closer to the theoretical value. While both methods result in density values that follow the expected theoretical trend, HS results in a more similar slope.

Table 3.3: Slopes of the density profile at 3.3 cm for HS, LK, and theoretical results

1D Gas Dynamics	HS	LK
-0.1450	-0.1469	-0.1844

3.5   Comparison to Quantitative Schlieren

The schlieren data that was processed is shown in Figure 3.18. This schlieren data is from a test series done by Falls in [31], where he describes the schlieren analysis of these conical projectiles in further detail. This data was taken with the Phantom VEO-4K 990 camera at full resolution (2304 x 4096 pixels) and had a resulting pixel-to-millimeter ratio of 35.67 pix/mm.
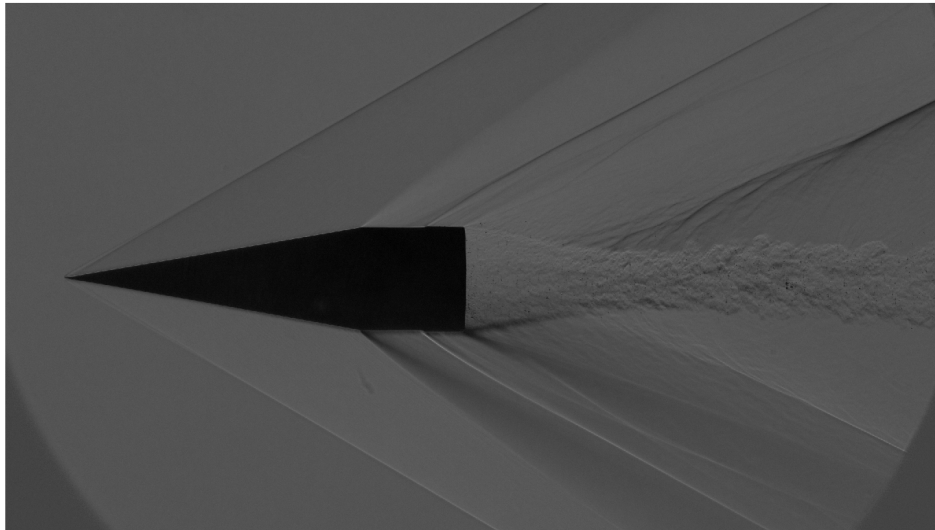
Figure 3.18: Schlieren image of the conical projectile in flight that was used to calculate the density profile [31].

The refractive angle was calculated using the procedures described by Hargather and Settles [21, 31]. A 10 m focal length calibration lens was used to determine the refractive angle by comparing the intensity variation inside the calibration lens to the intensity variation inside the schlieren image.

The Abel inversion process (Equations 2.24-2.28) was used to reconstruct the density field around the top half of the schlieren image using the values from Table 3.4. The schlieren derived density field is shown in Figure 3.19. The normalized density profile at incremental locations along the $10°$ section of the cone is shown in Figure 3.20 where the location 3.3 cm away from the cone tip is highlighted in green.

Table 3.4: Atmospheric conditions on the day the BOS test images were captured [31].

Test	Atmospheric Pressure (kPa)	Atmospheric Temperature (K)	$\frac{Pixel}{mm}$
Schlieren	84.8	286	35.66
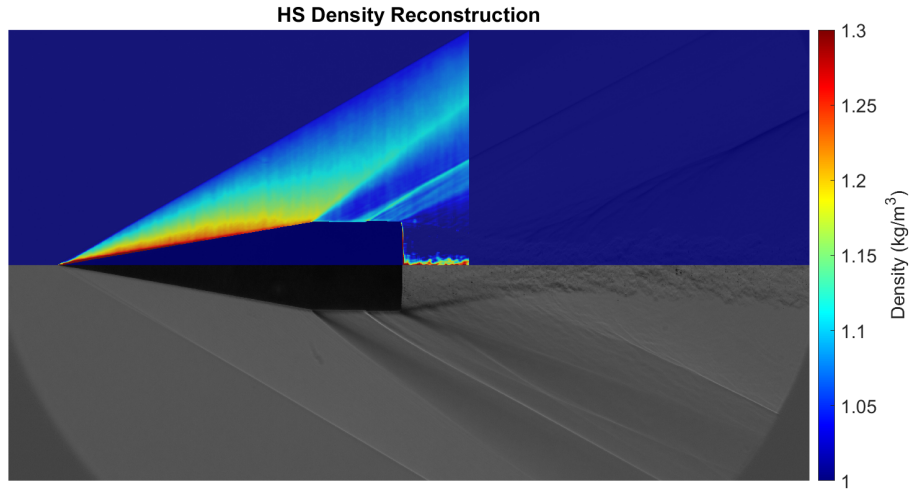
Figure 3.19: Density reconstruction of a conical projectile using schlieren imaging [31].
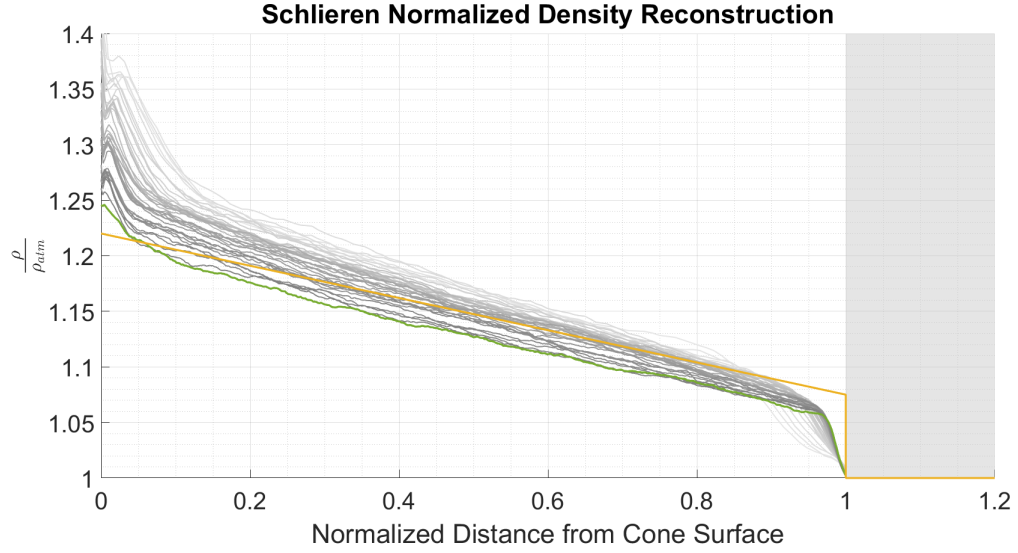
Figure 3.20: Normalized schlieren density profile for various locations along the conical projectile [31].

The density values derived from HS, LK, and schlieren are plotted in Figure 3.21. The density values at 1.16 cm, 2.23 cm, and 3.3 cm are all included in the plot with the distance from the cone surface normalized between 0 and 1.
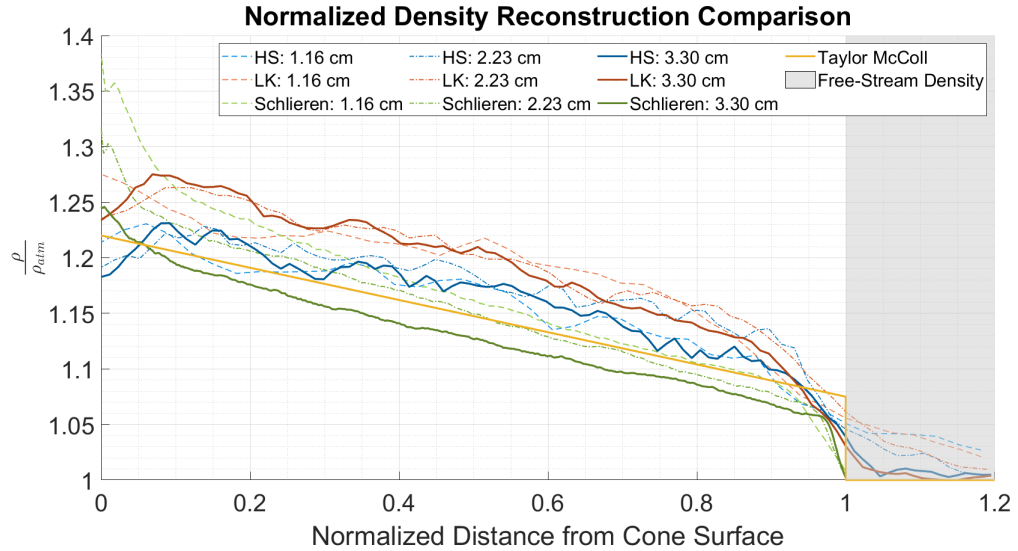
Figure 3.21: Density comparison plot. Calculated density profile around a $10°$ projectile traveling at $M = 2.15$ using optical flow, schlieren, and 1D gas dynamics.

Figure 3.21 shows that the schlieren density data falls below the theoretical values, the HS density values are above the theoretical values, and the LK density

values are above the HS values. Visually the HS values provide the best density reconstruction results for OF methods for the small-scale tests, but the error analysis of the density reconstruction will be used to make a final comparison of the OF methods.

3.6   Error Analysis

A standard error propagation [37, 38] was used to measure the error of the calculated refraction angle ε. The ε error is a function of the OF calculation and the calibration measurements for the test setup. The uncertainties associated with this are shown in Table 3.5.

Variable	Units	Error	Notes
Optical Flow	pixel	0.0249	One standard deviation of the un-shocked region
Pixel Measurement	pixel	1	Uncertainty in pixel measurement for calculating the pixel-to-meter ratio
Calibration Measurement	m	0.0001	Uncertainty in distance value for calculating pixel-to-meter ratio
L and l Distance	m	0.005	Uncertainty in length measurements
ε	radians	1.184×10^{-5}	Uncertainty in the refraction angle, this is a function of all the variables listed in this table

Table 3.5: Variables and the associated errors for the small-scale ε calculation

Calculating the error propagation through the Abel inversion is complicated since it propagates error from the free-stream air down to the cone surface. Abel is a function of ε and radius, however, the primary source of uncertainty is ε. To measure the uncertainty propagated through Abel, one standard deviation was added and subtracted to each ε value before the Abel inversion was performed. Adding one standard deviation is used to define the higher error bound for δ (the output of Abel), and subtracting one standard deviation defines the lower error bound. This method overestimates the error by maximizing the error associated with ε. The resulting error bounds for the Abel inversion are equivalent to the density uncertainty. Therefore, the density uncertainty is visualized in Figure 3.22.
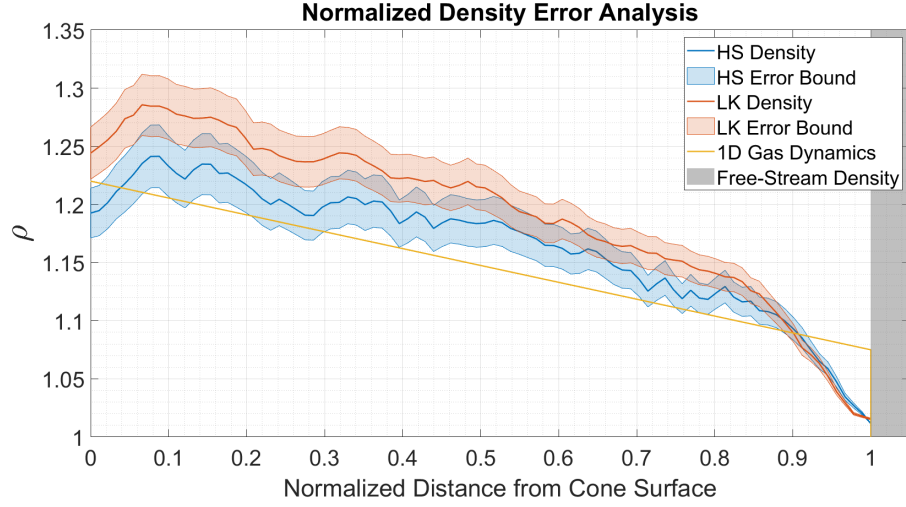
Figure 3.22: The HS density profile at 3.3 cm away from the cone tip, with the calculated error bounds and the 1D gas dynamic density values.

The percent error of both the HS and LK-derived density values was calculated using the equation:

$$\% \text{ Difference} = \frac{\text{Experimental-Theoretical}}{\text{Theoretical}} \cdot 100\% \qquad (3.2)$$

Where theoretical is the 1D gas dynamics relationship and experimental is the HS and LK-derived density values. The percent error for each OF method is shown in Figures 3.23.
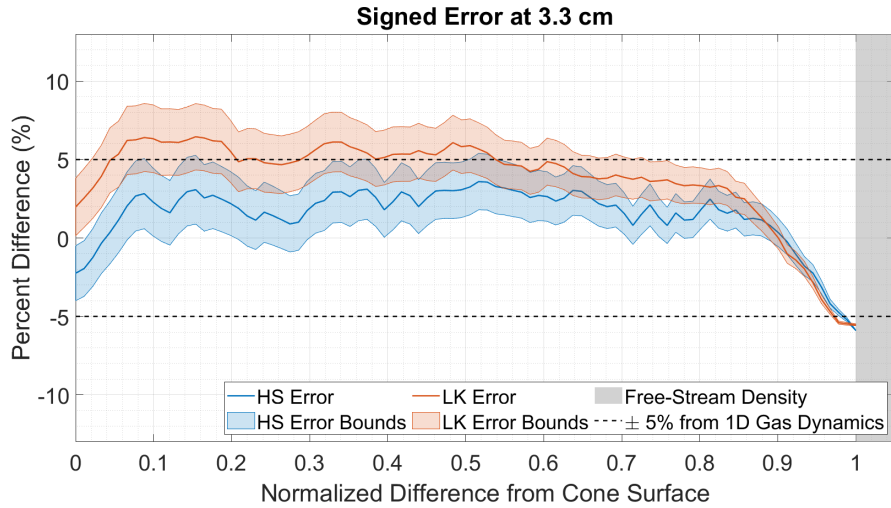
Figure 3.23: The HS signed percent error. The calculated error between the theoretical and experimental values.

Figure 3.23 demonstrates that HS calculation is better than the LK calculation in the small-scale tests since it only has a $\pm$ 5% error relative to the 1D gas dynamics.

3.6.1 Horn-Schunck Smoothing Considerations

It is of interest to see how changing the smoothing parameter value can affect the results of the HS method, so the HS density was reconstructed for various values of α. To determine the effects of smoothing on the HS method, the density field 3.3 cm away from the cone tip was reconstructed and plotted against one another. Figure 3.24 shows the density line plots with varying alpha values as well as the LK result. The slopes of each line are shown in Table 3.6.1.
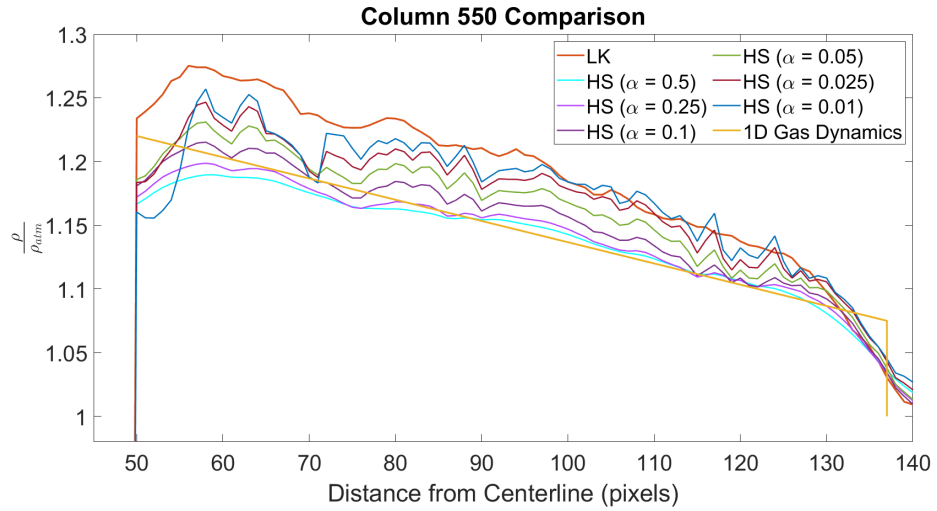
Figure 3.24: The effects of different alpha values on the density reconstruction

Table 3.6: Slopes of the density profile at 3.3 cm for varying α values

Method	α value	Slope ($\frac{\rho_{norm}}{dx_{norm}}$)
LK	-	-0.187
HS	0.5	-0.120
HS	0.25	-0.126
HS	0.1	-0.140
HS	0.05	-0.147
HS	0.025	-0.145
HS	0.01	-0.144

Figure 3.24 shows the variation in the density results with α values ranging between 0.01-0.5, as well as the LK and Taylor Maccoll profiles. A larger α value tends to dampen the density results, but too small of an α results in noisy data, which was also found by Atcheson [14] with subsonic flows. The slopes for each density profile are listed in table 3.6.1 and were calculated in the same manner as Table 3.3. The slopes for the density profiles are relatively close for the α values between 0.01 and 0.1 but vary more for the large α values. While the higher α values result in a normalized density that follows the theoretical profile more closely, the shock thickness does appear to increase. Since the α parameter does not significantly change the results of the values between 0.1-0.01, the 0.05 value will continue to be used for the analysis presented here. With $\alpha = 0.05$, the data is not over-smoothed nor under-smoothed (which can lead to the data becoming under-determined as found by Atcheson [14]).

CHAPTER 4

LARGE-SCALE RESULTS

The large-scale tests visualized the refractive field from a 1 kg spherical C4 charge. The high-speed images are processed through the two OF methods to quantify the density field which is then used to calculate the pressure profile. The pressure results are then compared between methods and to the pressure gauge as a baseline.

4.1 Optical Flow Processing

The primary BOS images were recorded with the Phantom VEO-4K 990 camera with a 4096 x 2048 resolution. The flow-off and primary flow-on image used for analysis are shown in Figure 4.1. The primary frame of interest is frame 9, which is 10 ms after detonation. The images had a resulting pixel-to-millimeter ratio of 0.3059 pxl/mm.

Figure 4.1: The (left) flow-off and (right) primary flow-on images that each OF method processed.

As discussed in the previous chapter, the output of the OF methods are the intensity shifts in the horizontal and vertical direction between the image pair. The measured horizontal and vertical shifts, as well as the calculated shift magnitude, are shown as colored arrays in Figure 4.2. Furthermore, a quiver plot depicting the magnitude and direction of the calculated pixel shift is shown for

every twentieth pixel. The charge was positioned 1 m above the ground. This resulted in a ground reflection, which caused an irregular shock wave reflection and mach stem to form. As observed in Figure 4.2, the mach stem is clearly visible and is part of the shock wave measured by the second pressure gauge. This mach stem is what will be analyzed here.
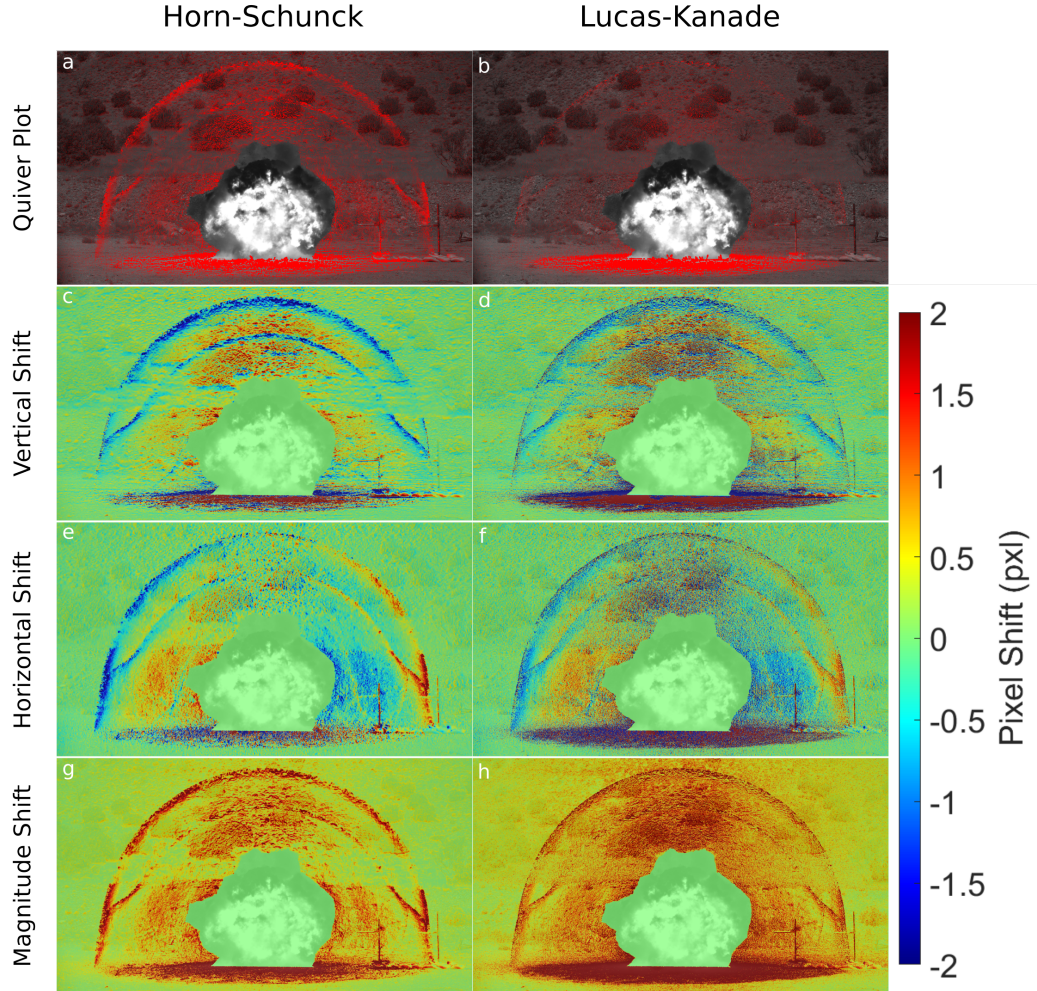
Figure 4.2: Results from the HS and LK OF algorithms. The left column (images a,c,e,g) are the results from the HS method, and the right column (images b,d,f,h) are the results from the LK method. Images (a) and (b) show the quiver plots, (c) and (d) show the horizontal displacement, (e) and (f) show the vertical displacement, and (g) and (h) show the magnitude displacement

The measured displacement for each method ranges from approximately -2 to 2 pixels, twice the amount of the small-scale tests. The far hill provided sufficient variation for the vertical displacement at the top of each image and the berm

also provided adequate variation to the horizontal displacement. However, the region between the berm and the far hill did not detect a significant displacement value in any direction. Figure 4.1 shows that this region is relatively uniform so it is expected that a variation due to a refractive disturbance would not be resolved well. The fireball and product gases were masked out of the OF processing since these regions could not be analyzed. In all of the images, the ground just below the fireball detected a large displacement. This displacement is due to the loose dirt on the test range becoming disturbed as the shock wave passes over that region of the ground and will therefore be neglected.

It appears that the LK method detected a higher displacement value than HS since there are regions that appear darker in it than in the HS counterpart. But, the HS method has smoother variation in the displacement gradient, expanding radially outward, which could be due to the HS smoothing parameter (α). To compare the OF methods further, the numeric displacement values were compared. The pressure gauges were located to the right of the detonation and measured the horizontal displacements of the blast waves. Because of the pressure gauge positions, the horizontal displacements to the right of the detonation site were used for the primary analysis. The horizontal displacements are shown in Figure 4.2 as images e and f.

4.2   Background Noise Characterization

The background regions outside of the blast wave appear to be relatively uniform in calculated background displacement. To characterize the background noise in the system, the horizontal displacements in an undisturbed region of the background were measured and plotted. To find the undisturbed background region, the shock wave edge was found using the basic image subtraction process described in the previous chapter. The background-subtracted image with a zoomed in view of the shock edge is shown in Figure 4.3.
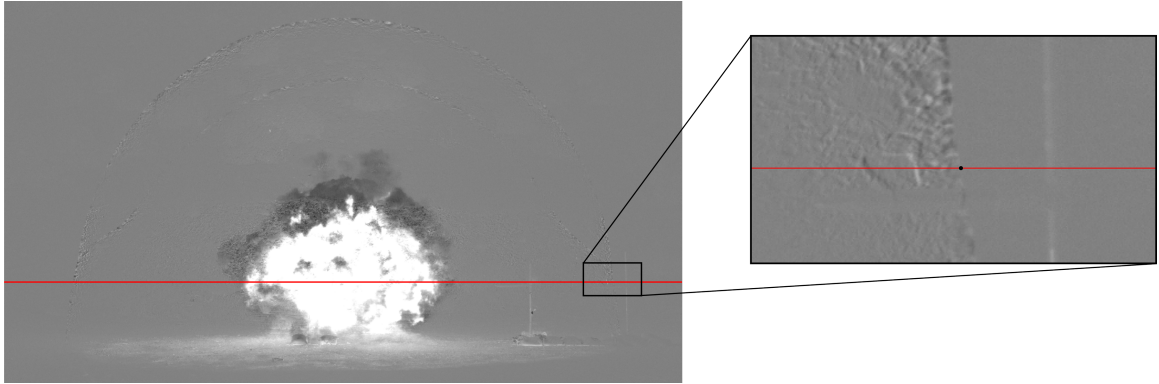
Figure 4.3: Background subtracted image with a histogram shift of the large-scale test. A zoomed-in region of the right side of the shock wave is enlarged to show detail.

The undisturbed region of the background that was selected is shown in Figure 4.4. The horizontal displacement values inside the region were graphed as a histogram. The histogram plot is shown in Figure 4.5 and was used to calculate the standard deviation of each OF method for the large-scale tests. The average background distortion for both methods is 0.024 pixels with a standard deviation of $\pm$ 0.1623 pixels for the HS method, and $\pm$ 0.3425 pixels for the LK method. Both standard deviations were higher than the small-scale tests which was due to the use of a natural background.

Figure 4.4: Region of interest that was used to measure the standard deviation of the OF methods.

Horizontal Displacement Background Characterization
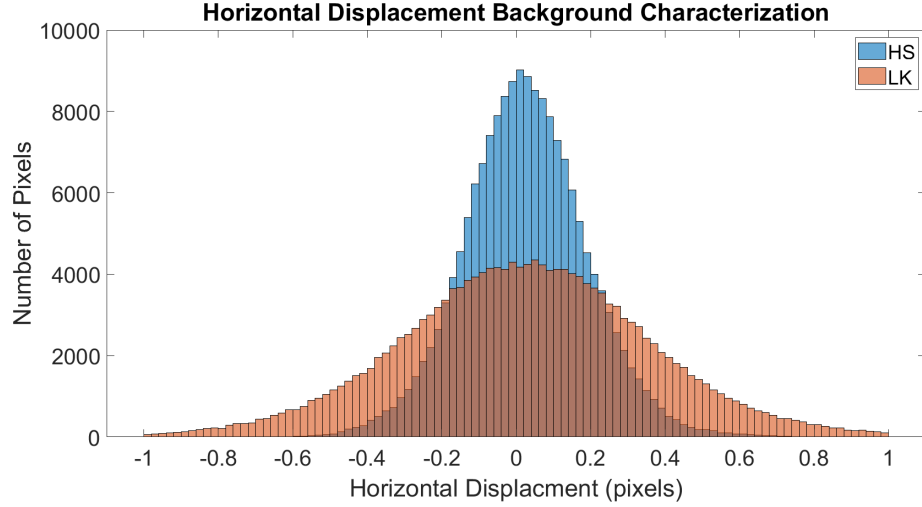
Figure 4.5: Distribution plot of the horizontal displacement values for each OF method. The distribution plot is the horizontal measurements of an undisturbed region of the background.

Unlike the small-scale results, the average displacement and background standard deviation values would change slightly when the identified background region was changed. The small-scale tests had a random light-dark pattern that was designed to provide sufficient background variation in order to detect refractive fields. The variation in the natural background of the large-scale test is random both in intensity value and in the size of the variation. As shown in Figure 4.1, there are large bushes that provide darker intensity variations over a large area and there are also lighter intensity variations over a small area due to rocks and debris. While the variation in the average displacement and standard deviation was small ($\pm$ 0.02 pixels), the region that is most similar to the local regions of an image for their background noise was used to assess the local pixel displacement measurements.

4.2.1 Natural Background Grade System

An analysis method was developed to "grade" the background. The method consisted of manufacturing a flow-on image by translating the flow-off image a specified amount of pixels in the x and y direction. For this method, the manufactured image was translated 1 pixel to the right. The manufactured image was translated in the horizontal direction since that is the primary displacement gradient that was of interest for this analysis. The image was translated 1 pixels over since Figure 4.2 shows the displacement values to be around 2 pixels at the shock edge —so 1 pixel allowed for a good assessment of the background's capability of detecting the shift inside the shock wave.

The flow-off image and manufactured flow-on image were processed through both OF methods to determine what regions will measure the full 1-pixel horizontal displacement. The pixel locations that were able to measure a 1-pixel horizontal shift were considered areas of optimal variation, and areas not able to calculate any shift are areas with insufficient background variation. To visualize the detected shifts, a colored array was used where yellow areas highlight a good background variation grade, and blue denotes a poor background variation grade. The colored array for both the HS and LK method is shown in Figure 4.6.

Both OF methods have good variation throughout the entire image, however, there were regions where the LK method did not resolve the pixel shift as well as the HS method. This procedure was also done with a single pixel shift in the vertical direction and there was no noticeable difference between the vertical grade results and the horizontal grade results. To simulate a flow in both the horizontal and vertical direction, the manufactured image was translated 1 pixel up and 1 pixel to the right to see if there was any variation from Figure 4.6. The grade results from this translation are shown in Figure 4.7. The colored array shows that the HS method grade decreased slightly in some areas, but the LK method was significantly affected.

The HS method's ability to detect both the horizontal and vertical pixel shift better than the LK method is attributed to the HS method smoothing term, α. To determine the full effect of α, a background noise histogram plot was created to compare the HS noise if the α term was changed. This histogram is shown in Figure 4.8. As the histogram shows, the smaller α term does result in a histogram similar to the LK result in Figure 4.5. For the data analyzed here, an α of 0.05 was used.

As shown in Figure 4.2, the shock front detected an absolute pixel displacement value of approximately 2 pixels. Therefore the background grade for the detection of a large shift (3 pixels) was conducted. The results of each method are shown in Figure 4.9. The results are similar to what was found previously with the addition that only certain areas in the background are suited for detecting large shifts.
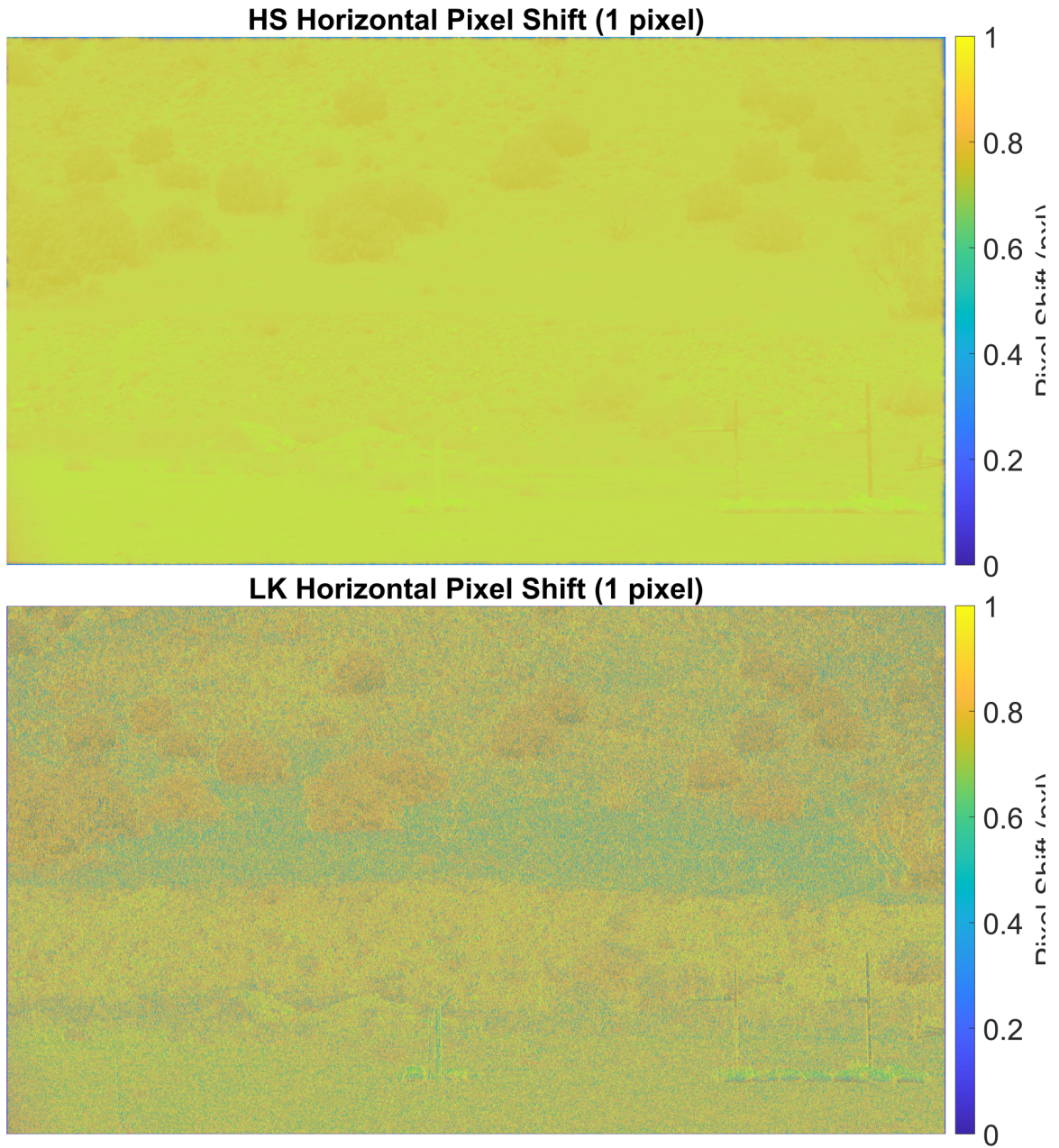
Figure 4.6: The background grades for the HS and LK OF methods. The HS background grade is on the top. The LK background grade is on the bottom. A detected pixel shift of 1 represents good background variation and is highlighted in yellow. Poor background variation is a detected pixel shift of 0 and is highlighted inblue

HS Horizontal and Vertical Pixel Shift (1 pixel)

LK Horizontal and Vertical Pixel Shift (1 pixel)
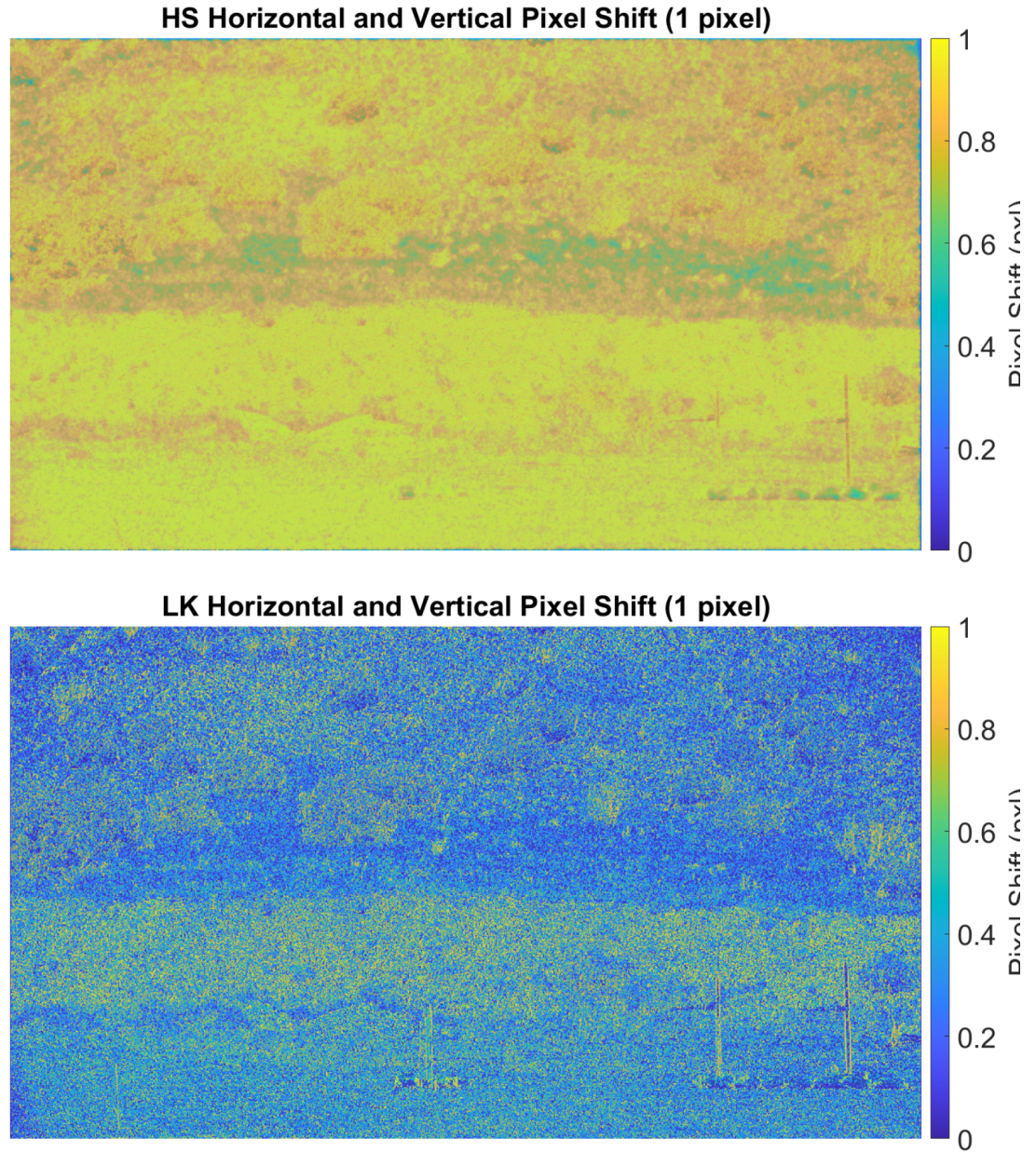
Figure 4.7: The background grades for the HS and LK OF methods. The HS background grade is on the top. The LK background grade is on the bottom. A detected pixel shift of 1 represents good background variation and is highlighted in yellow. Poor background variation is a detected pixel shift of 0 and is highlighted inblue
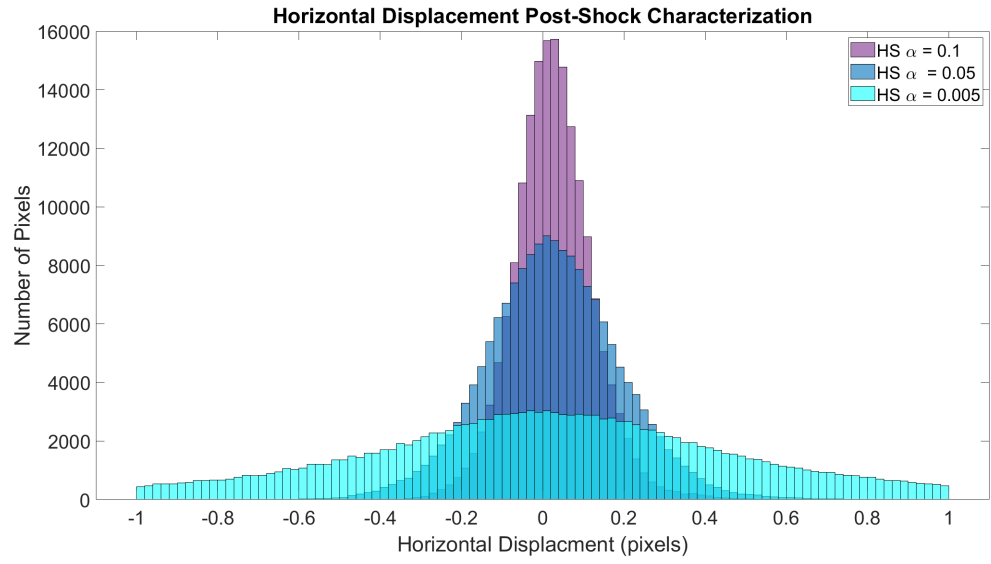
Figure 4.8: Background noise histogram comparing the HS method and the effects of different α values.

Background Grade (Horizontal Shift Only)

LK Background Grade (Horizontal Shift Only)
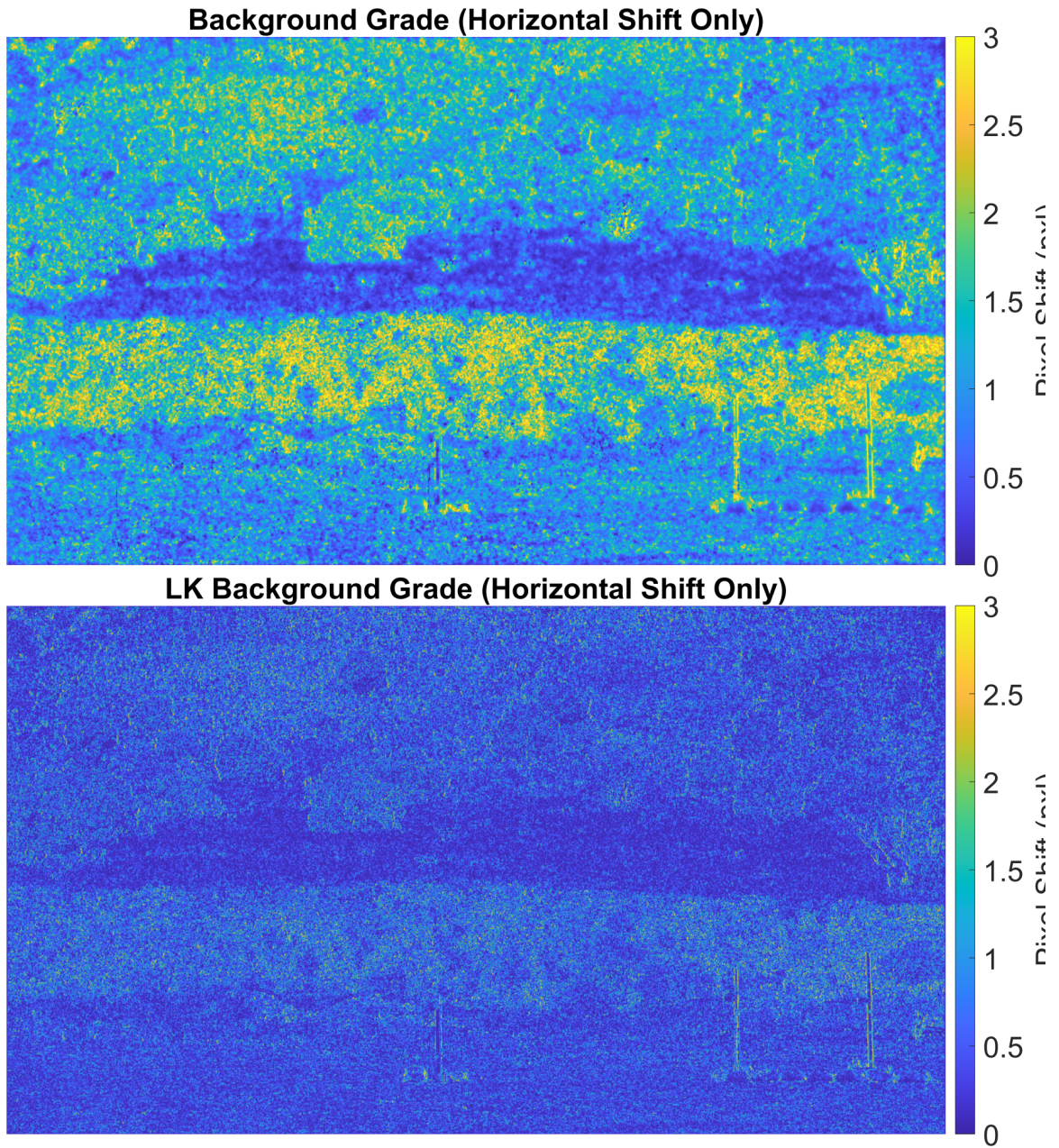
Figure 4.9: The background grades for the HS and LK OF methods. The HS background grade is on the top. The LK background grade is on the bottom. A detected pixel shift of 3 represents good background variation and is highlighted in yellow. Poor background variation is a detected pixel shift of 0 and is highlighted inblue

54

4.3 Pixel Displacement Analysis

To compare the calculated displacements from each OF code, a row from the image needed to be selected. To select a row with optimal background variation, the HS background grade image in Figure 4.6 was used. The bounds to determine which row was to be extracted included the region just below the triple point of the primary shock, reflected shock, and the mach stem (found using Figure 4.3) and above the pressure gauge; these are marked on Figure 4.10 as black horizontal solid lines. Anything below the pressure gauge had insufficient variation to detect large pixel shifts. Also shown in Figure 4.10, are two black vertical dotted lines that show the shock locations for 10 ms and 12.2 ms after detonation as determined by the background-subtracted images (Figure 4.3).The row that was analyzed is shown in the figure as a black horizontal dashed line. This row was manually selected and was specifically chosen because it was close to the pressure gauge and had a good overall grade at the shock location for both 10 ms and 12.2 ms after detonation.
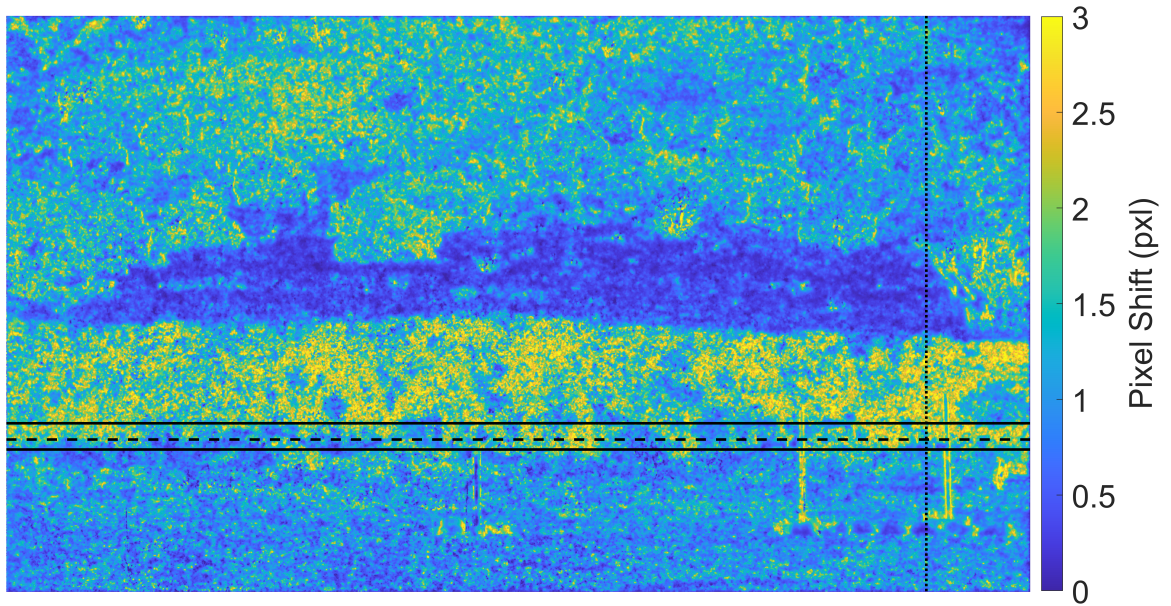
Figure 4.10: The HS background grade image with annotations to determine the best row to analyze. The two horizontal black lines represent the bounds of which the row could be selected with the bottom line depicting the top of the pressure gauge and the top line the location of the mach stem triple point. The vertical dotted lines show the shock location for 10 ms and 12.2 ms after detonation. The horizontal dashed line represents the line that was selected to be analyzed.

The line that was selected in Figure 4.10 is the 1695th row from the top of the image. Only the right hand side of the row was analyzed, from the detonation site (centerline) and extending to the right of the image, as shown by Figure

4.11 by the red line. The horizontal displacements calculated by HS and LK are shown in Figure 4.12 for 10 ms after detonation and Figure 4.13 for 12.2 ms after detonation).

Figure 4.11: The flow-on image 10 ms after detonation. The red line depicts the row that is analyzed and ultimately converted to pressure. The line falls just above both pressure gauges, but below the triple point with the mach stem.

a

b
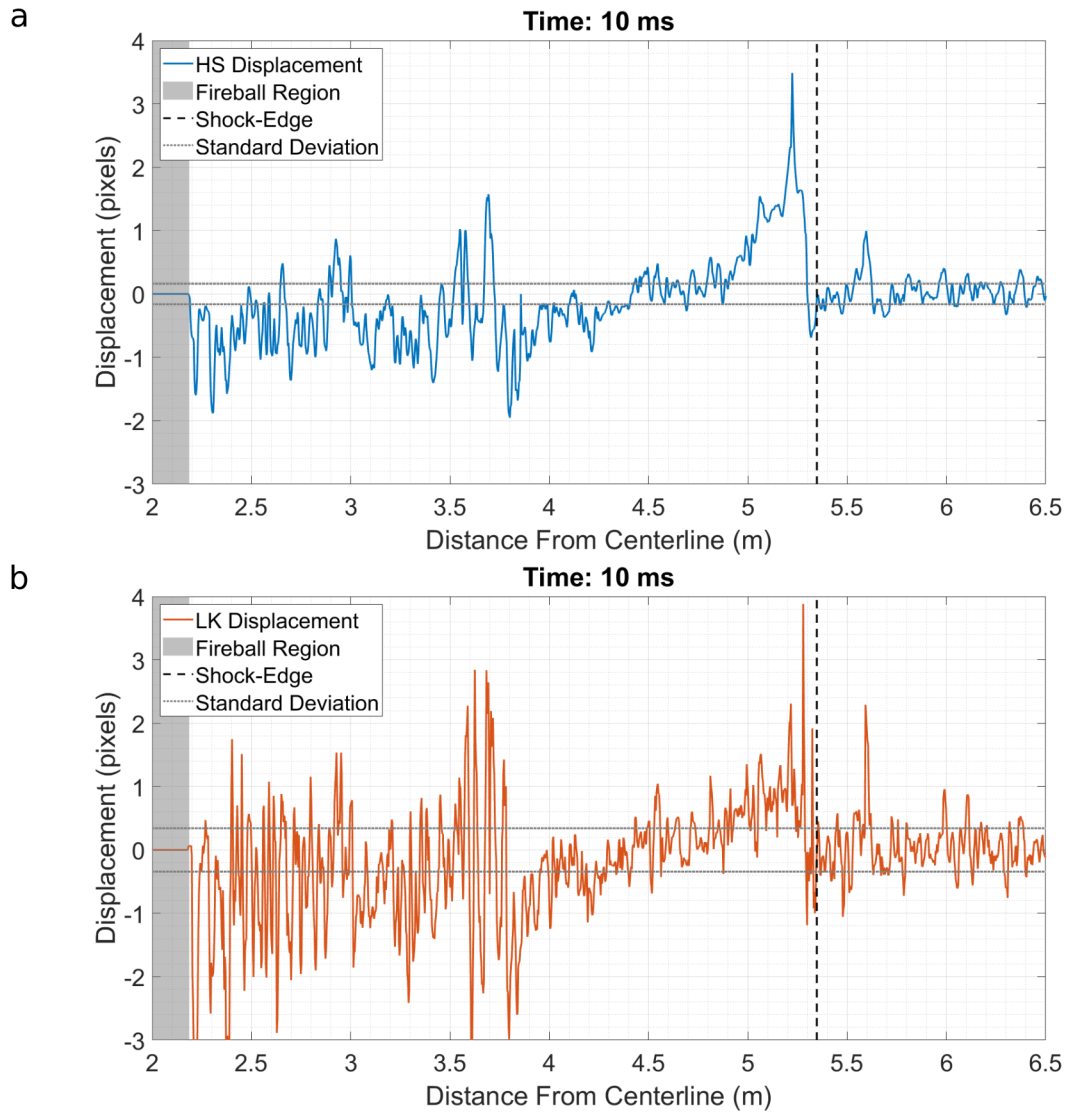
Figure 4.12: Line plot of the OF outputs at 10 ms after detonation. The HS results are in blue, the LK results are in red, the shock location is marked with a black vertical line, and the gray horizontal lines show the standard deviation for each method.
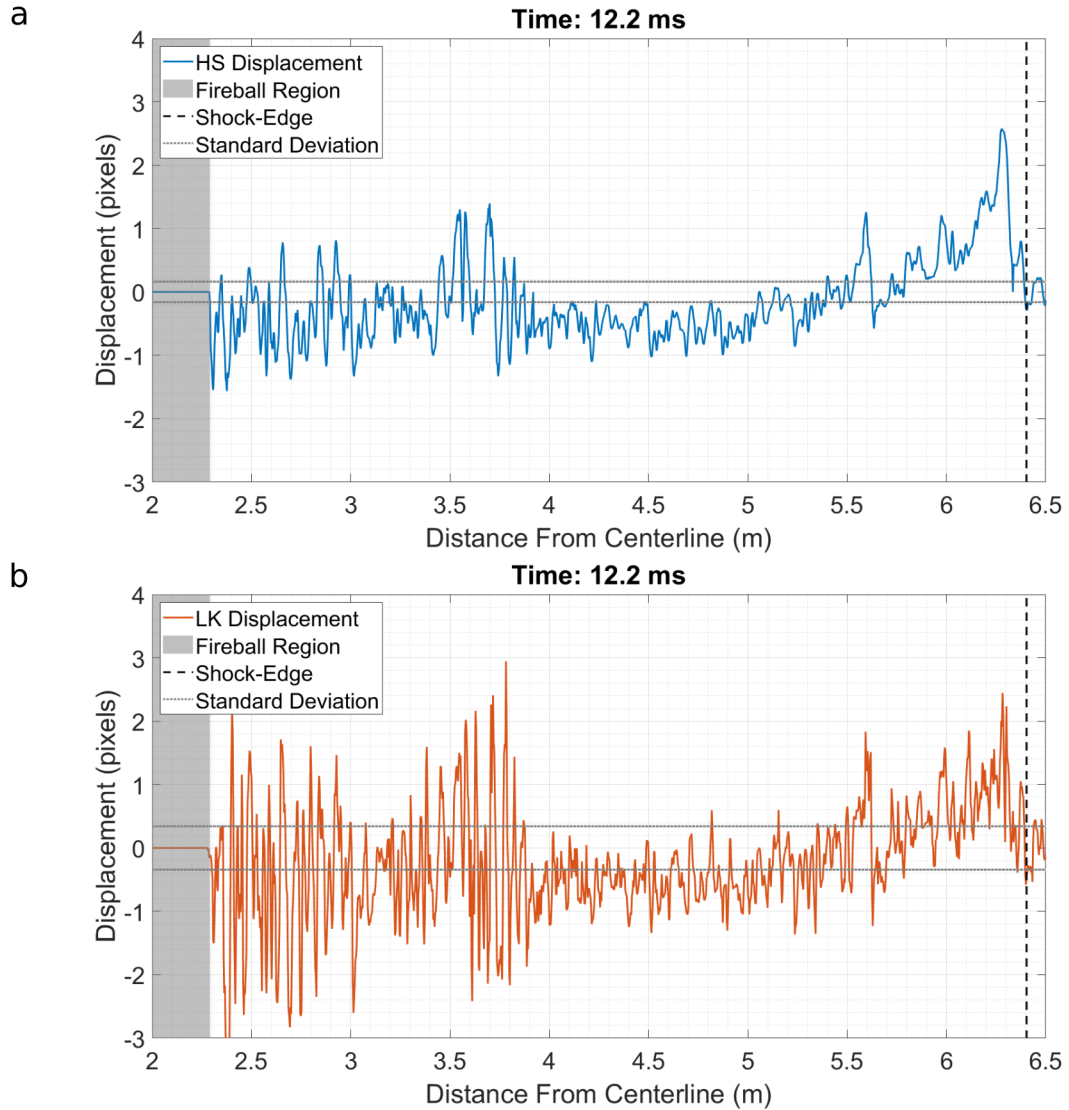
Figure 4.13: Line plot of the OF outputs at 12.2 ms after detonation. The HS results are in blue, the LK results are in red, the shock location is marked with a black vertical line, and the gray horizontal lines show the standard deviation for each method.

Each plot has the calculated standard deviation shown by two horizontal gray dotted lines, and one black dashed vertical line showing the shock location measured from the background-subtracted images. The detected peaks in all four graphs at 3.65 m and 5.6 m is the illumination of the pressure gauge stands and not a shock feature. The LK method appears to be significantly noisier than the HS method. As shown in Figure 4.8, this can be attributed to the HS α which smoothed the oscillations that the LK method highlights. This gives HS a relatively clean gradient of measured displacements with well-defined peaks.

Table 4.1 lists the pixel location from the centerline where each OF method

detected a displacement peak. The table also has the point at which each OF code crossed the standard deviation boundary and the expected shock wave location found using the background-subtracted image in Figure 4.3).

Table 4.1: HS and LK Shock Detection Values in Pixels from the Explosion Center

		HS		LK	
Time after Detonation (ms)	Shock Location (pix)	σ Crossed (pix)	Peak (pix)	σ Crossed (pix)	Peak (pix)
10.0	1636	1620	1598	1630	1615
12.2	1959	1955	1921	1955	1922

In all of these graphs, the standard deviation boundary was not crossed until after the measured shock location, unlike the small-scale test. All of the graphs had a shock width ranging from 20-40 pixels wide without much of a pattern. While 10 ms did not detect the shock peak as close to the actual shock as 12.2 ms did, 10 ms was used for the primary analysis since the illumination of the PG did not interfere with the displacement values as much as it did at 12.2 ms.

4.4 Density Reconstruction

The density field was reconstructed using Equations 2.20-2.29 and the atmospheric values listed in Table 4.2. The resulting density plots are shown in Figures 4.14 and 4.15. Each graph has the normalized density values for the HS and LK drawn in a solid line, the location of the pressure gauges, and the shock location shown as vertical dashed lines. Each graph also has a grayed-out region to represent the edge of the fireball mask.

Table 4.2: Atmospheric conditions on the day the C4 test was conducted

Atmospheric Pressure (kPa)	Atmospheric Temperature (K)	$\frac{\text{Pixel}}{\text{m}}$
84.79	302.5	305.94
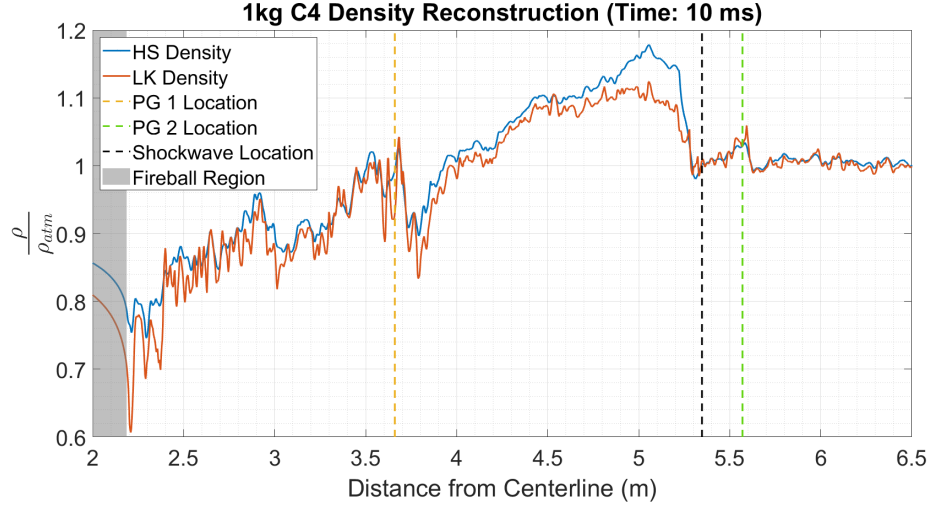
Figure 4.14: Line plot of the density reconstruction for the HS and LK techniques at $t = 10$ ms.
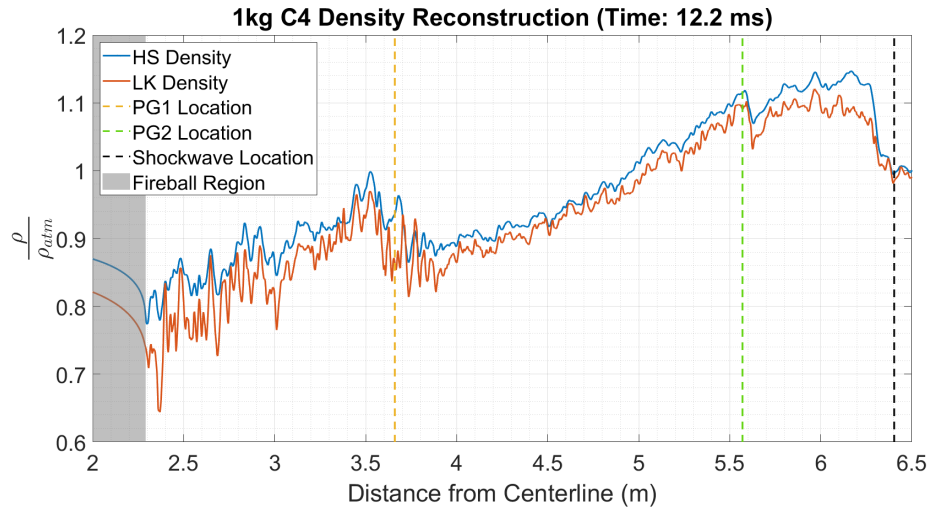
Figure 4.15: Line plot of the density reconstruction for the HS and LK techniques at $t = 12.2$ ms.

As shown in the graphs, the intensity increase due to the illumination of the pressure gauge stands could easily be interpreted as a shock feature behind the mach stem. Therefore it is important to be aware of these locations for an accurate analysis as the displacement values are analyzed further.

4.5 Pressure Reconstruction

To convert the density values to pressure, M and temperature profile needed to be calculated, and, the density needed to be represented as a function of time rather than position. To calculate the M, two consecutive background subtracted frames were used to measure the shock front displacement (in pixels) between frames. The shock displacement was then converted to a displacement in meters using Equations 2.20 -2.21, and then it was divided by the time step (dt) between the two frames to estimate the shock velocity V_{shock}:

$$V_{shock} = \frac{u_m}{dt} \tag{4.1}$$

where,

$$dt = \frac{\text{\# of frames}}{\text{Frame Rate}} \tag{4.2}$$

With the shock velocity, M was calculated using Equation 2.30. Equation 2.31 was used to calculate the expected temperature rise at the shock front. The temperature assumption described by Tobin and Hargather [34] suggests that there is an increase in temperature at the shock wave location, and then, it decreases linearly behind the shock wave in the same time it takes density or pressure to return to atmospheric conditions. The pressure gauge data was used to estimate the time it would take for the temperature to decay back to atmospheric temperature. The temperature is assumed to remain at the atmospheric value after the temperature decay. The temperature profile that is used is shown in Figure 4.16, where the shock peak would be at $t = 0$ ms for simplicity. M, temperature ratio, and temperature decay for both times are listed in Table 4.5.
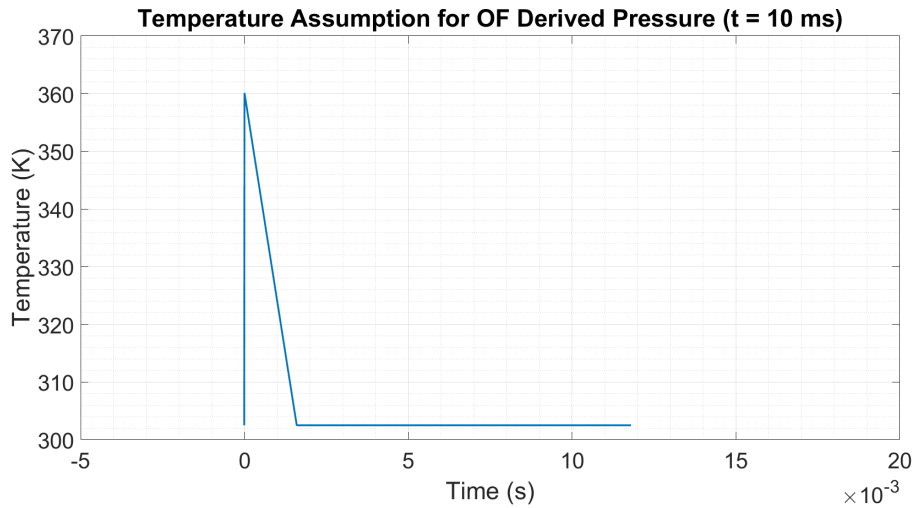
Figure 4.16: The assumed temperature profile behind the shock wave.

The density data needed to be plotted in terms of time so that the pressure profile could be calculated. To convert the x-axis from distance to time, the calculated shock velocity is used:

$$dt = \frac{dx}{V_{shock}} \tag{4.3}$$

The density can then be plotted versus time, where the initial density jump is at $t = 0$ ms, just like the temperature assumption. The pressure profile can be calculated using the Ideal Gas Law, Equation 2.33. The pressure plots are shown in Figures 4.17 and 4.18, where the pressure profile for both times was compared to the second pressure gauge data.

Table 4.3: Calculated M, temperature rise, and temperature decay time for each time period.

Time (ms)	M #	$\frac{T_2}{T_{atm}}$	Decay time (ms)
10	1.299	1.190	1.56
12.2	1.325	1.207	1.56
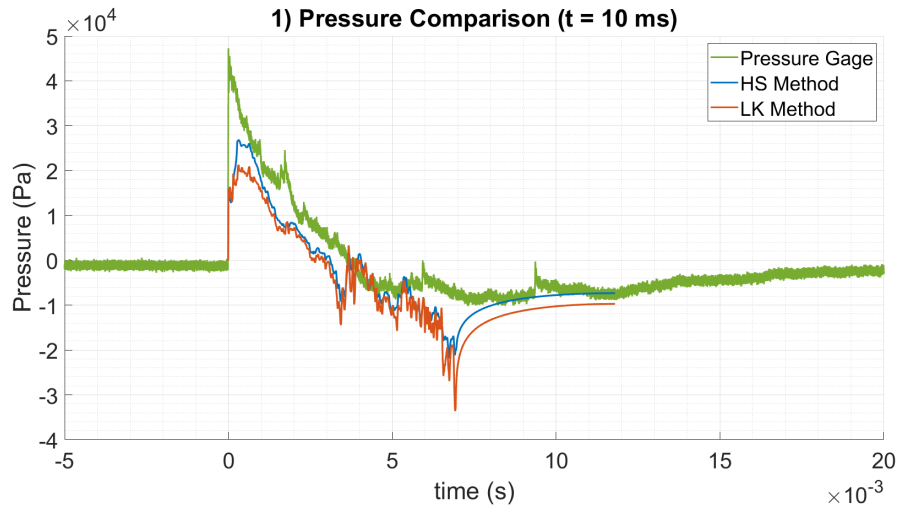
Figure 4.17: Pressure comparison between the second pressure gauge, HS, and LK derived data at 10 ms after detonation.
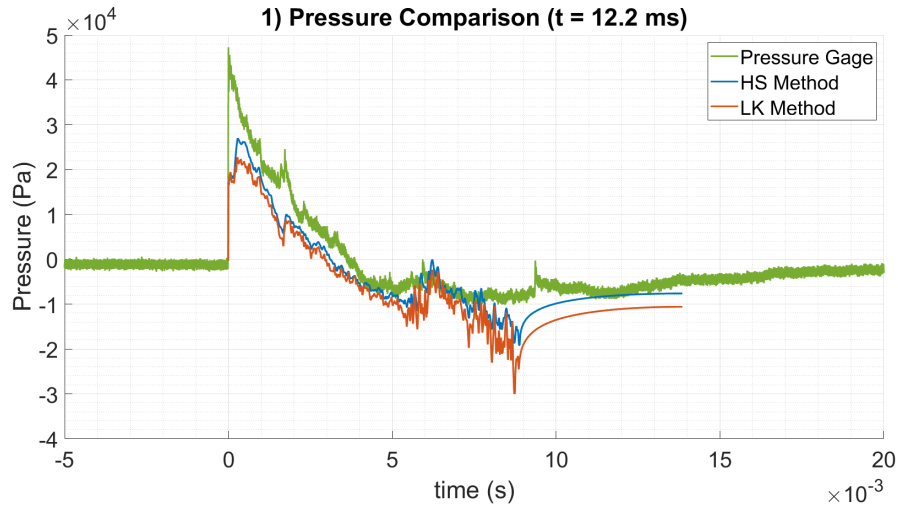
Figure 4.18: Pressure comparison between the pressure gauge, HS, and LK derived data at 12.2 ms after detonation.

The temperature profile is set so that the temperature rise happens right at the shock location found with the background-subtracted image rather than the standard deviation cross point or the local peak as shown in Table 3.3. Focusing on the data 10 ms after detonation, it was desirable to locate where the local peaks inside the pressure profile were on the background-subtracted image so it could be better assessed for the cause of each peak. Figure 4.19 identifies the shock edge that was found with the background subtracted method, the peak location region from the OF pressure profile, as well as the secondary peak located at $t = 0.00175$ ms in Figure 4.17. The background-subtracted shock location appears to have lower contrast in that region of the image which explains why the standard deviation point is not crossed closer to the shock edge. The OF-detected pressure peak aligns with a region that has high contrast between the flow-on and flow-off image. Finally, the secondary peak at 0.00175 ms appears to be a shock feature and not a false peak due to the pressure gauge illumination (which can be seen in Figure 4.19 at 1390 pixels).
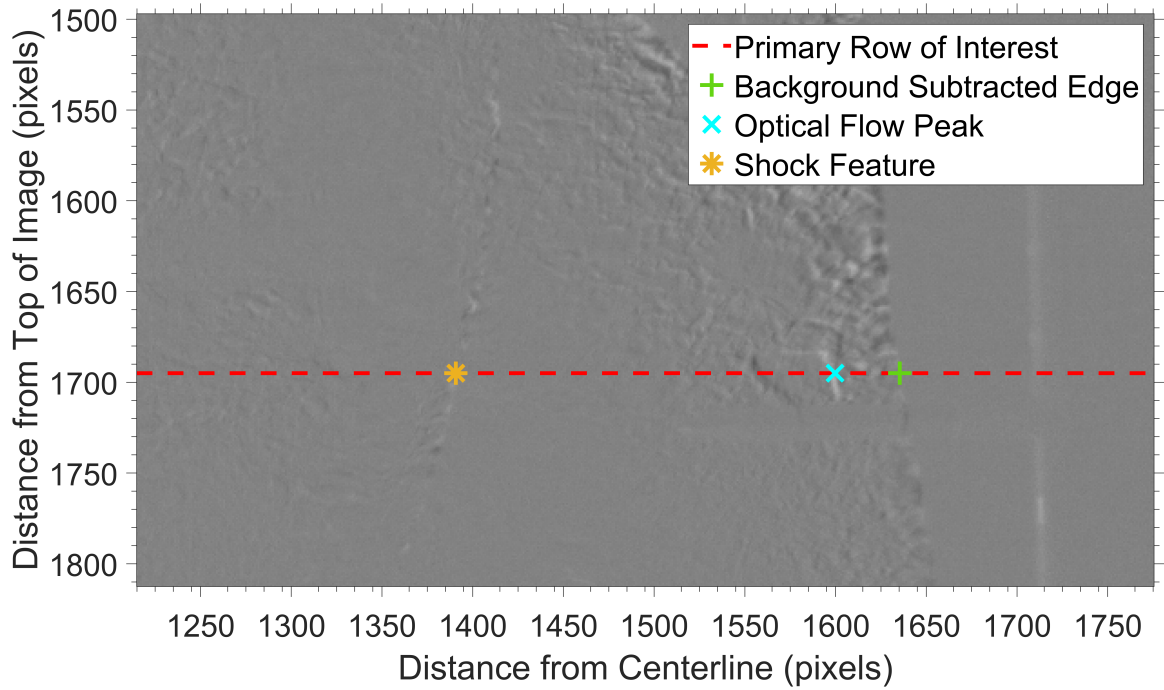
Figure 4.19: Background subtracted image with key locations annotated. The row of interest is shown as the red horizontal dashed line. The background subtracted is edge is shown as the green "+" symbol. The local pressure peak from the OF method is shown as a cyan "x". The secondary peak and found shock feature is shown by the yellow "*" symbol.

The effects of placing the temperature rise at the standard deviation threshold or the local peak, rather than the background subtracted boundary, were compared and are shown in Figure 4.20. For the comparison, the temperature decay time was kept constant. The initial pressure rise and slope of the pressure decay do not change significantly for the pressure comparison between images (a) and (b), but the slope does become steeper in image (c). This is because by moving the temperature rise further inside the shock wave, the secondary peak that was originally seen is no longer visible. Therefore to conserve the feature tracking aspects of the OF-derived methods, the temperature rise beginning at the background subtracted edge was used. Keeping this temperature profile is also a more accurate representation of what the temperature would be after the initial shock. Following these techniques, the OF-derived pressure data resolved the same trends and peak features as the pressure gauge. There is some evidence of stretching and compression happening within the pressure profile and this is due to the constant velocity assumption. There is not much of a difference between the HS and LK method besides the initial pressure peak identification at which the HS method resolved a higher value close to the pressure gauge results. To further compare these results, the error analysis on each method was conducted.
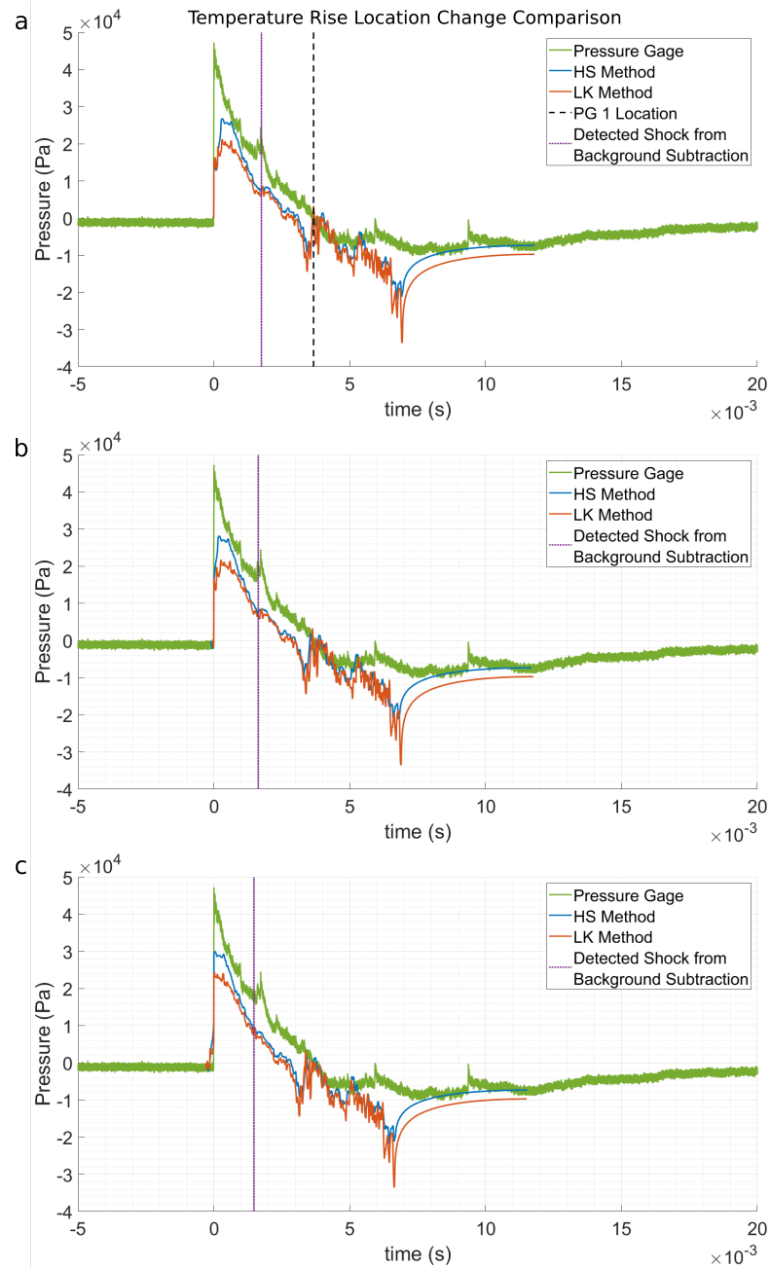
Figure 4.20: Calculated pressure plots where the temperature rise assumption is changed. Image (a) shows the pressure plot where the temperature rise begins at the pixel location where the shock boundary is found using the background subtration process. Image (b) shows the pressure plot where the temperature rise begins at the pixel location where the background noise threshold is crossed. Image (c) shows a pressure plot where the temperature rise happens at the pixel location where the OF methods detected a peak displacement. Image (a) shows a vertical dashed black line which shows the location of the first pressure gauge. There is a vertical dotted purple line that shows the location of the shock feature found in Figure 4.19. With the change in the temperature rise location, this peak can disappear.

65

4.6 Error Analysis

The error propagation through the large-scale OF analysis was calculated similarly to the small-scale tests, just with an extension to also calculate the pressure error. First, the uncertainty of ε was calculated using the error associated with the calibration object (Figure 1.2) and the l and L distances. These uncertainties are listed in Table 4.4. The ε error was calculated for each point behind the shock front to the fireball mask and was indexed as a row vector.

Table 4.4: Uncertainty values for ε calculation

HS Optical Flow Uncertainty	LK Optical Flow Uncertainty	Pixel Measurement Uncertainty	l and L Uncertainty
0.1623 pixels	0.3425 pixels	0.5 pixel	0.9144 m (1 yard)

The error propagation through the Abel inversion was measured by first adding and then subtracting one standard deviation of the background noise to the ε values prior to processing the data with Abel. The addition and subtraction of the ε error created maximum error bounds of the δ error and, therefore, density error. As with the small-scale test, this does overestimate the error associated with the Abel inversion since the likelihood of each point having maximum error is low. The OF-derived density values are shown in Figures 4.21 and 4.22.
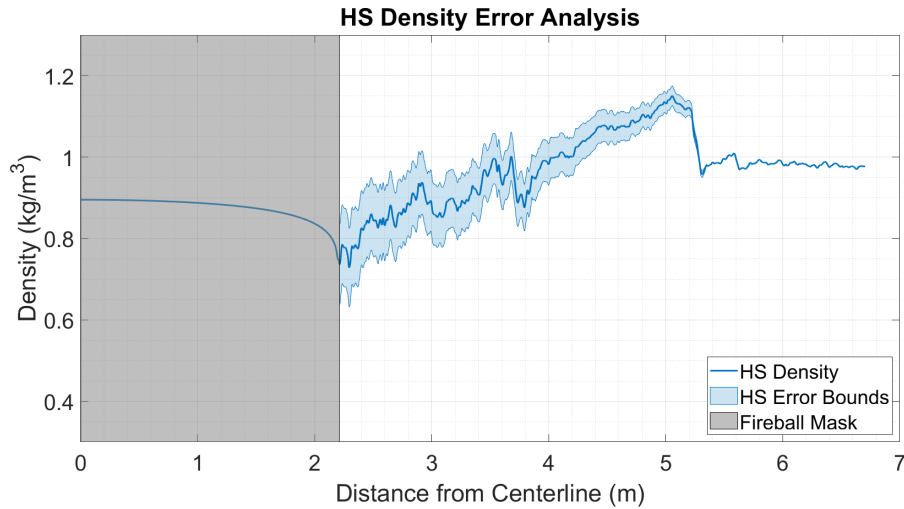
Figure 4.21: HS density error plot. The error increases towards the detonation site, which is due to Abel forward propagating error down from free-stream density.
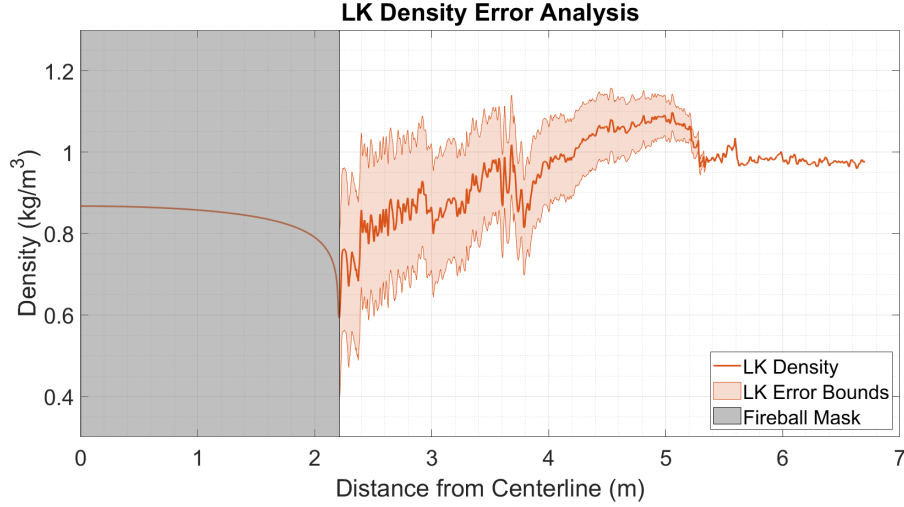
Figure 4.22: LK density error plot. The error increases towards the detonation site, which is due to Abel forward propagating error down from free-stream density.

The error increases from the shock front toward the fireball mask due to the error propagation in the Abel inversion. HS had a significantly lower error bound since it had half the background noise standard deviation than the LK method. The uncertainty for the pressure calculation includes the temperature assumption inside the shock wave. The temperature jump is related to M, so the error associated with the M is calculated first; the associated values can be seen in Table 4.5. The camera timing was found to have an insignificant amount of error, so it is not included in this error propagation.

Table 4.5: Uncertainty associated with the M calculation

Pixel Uncertainty	Shock Velocity Uncertainty	T_{atm} Uncertainty	M Uncertainty
0.5 pixels	2.203 m/s	1 K	0.0077

Next, the error propagation for the temperature decay section behind the shock wave was calculated. The associated uncertainties for calculating the temperature decay are shown in Table 4.6. Since each point from the detonation site to the shock front has a specific temperature error, each point is evaluated separately to calculate the pressure uncertainty. The final pressure uncertainty from the HS and LK methods are shown in Figures 4.23 and 4.24.

Table 4.6: Uncertainty associated with the temperature profile calculation

M Uncertainty	$\frac{T_2}{T_{atm}}$ Uncertainty	T_{atm} Uncertainty	Time Decay Uncertainty	Time Step Uncertainty
0.0077	0.0099	1 K	0.1 ms	3470 μs
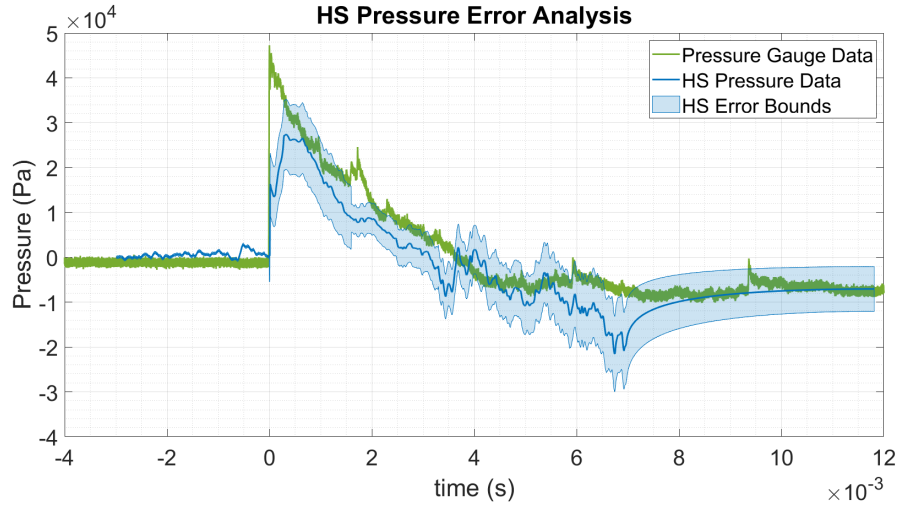
Figure 4.23: HS error propagation for the large-scale tests. The HS method is shown in blue and the pressure gauge results are shown in green.
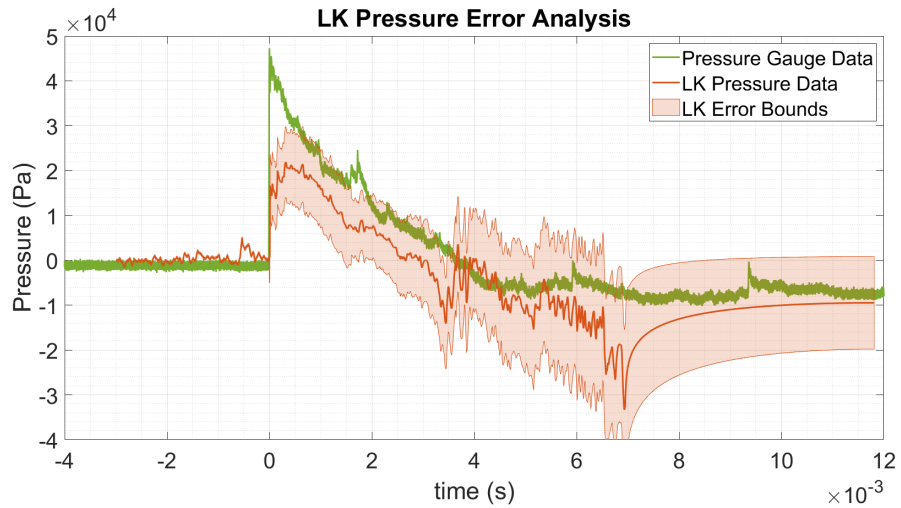
Figure 4.24: LK error propagation for the large-scale tests. The LK method is shown in red, and the pressure gauge results are shown in green.

Figure 4.23 and 4.24 show that HS tends to have a lower error bound than LK. The smoothing parameter (α) that was selected does not appear to over-smooth the image, nor does it smooth the peak displacement, density, and pressure values. While the lack of smoothing in the LK method might provide a more detailed analysis of what is happening at each pixel, that level of detail is noisy, not unnecessary, and produces a higher background standard deviation and thus a larger error than HS. Therefore, the better OF technique for large-scale experiments is the HS method.

Because there is an inherent light added to the system with the illumination from the fireball, it was desirable to see if that can be reduced by selecting a different flow-off frame.

4.6.1 Flow-off image considerations

To determine if the overall error in the system is impacted by the illumination from the fireball (like the pressure gauge stands that produce false peaks) a flow-off image 4.4 ms after detonation was used (denoted as sequential OF since it uses a flow-off image with a refractive disturbance). The illumination from the fireball in the sequential subtracted process should be more similar to the illumination in the frame of interest (10 ms after detonation). Figure 4.25 shows the new flow-off and flow-on images that were processed. The OF results are shown in Figure 4.26 which can be compared back to the OF results in Figure 4.2. The sequential OF limits the analysis region to the area between the shock location in the frame 4.4 ms after detonation and the shock location 10 ms after detonation. This is not a hindrance to this analysis because the shock at 4.4 ms after detonation has not reached the first pressure gauge stand yet, and the data that is of focus is located between the two pressure gauges.

Figure 4.25: The new flow-off and flow-on image to reconstruct sequential OF. The flow-off image is 4.4 ms after detonation, and the flow-on image is 10 ms after detonation.
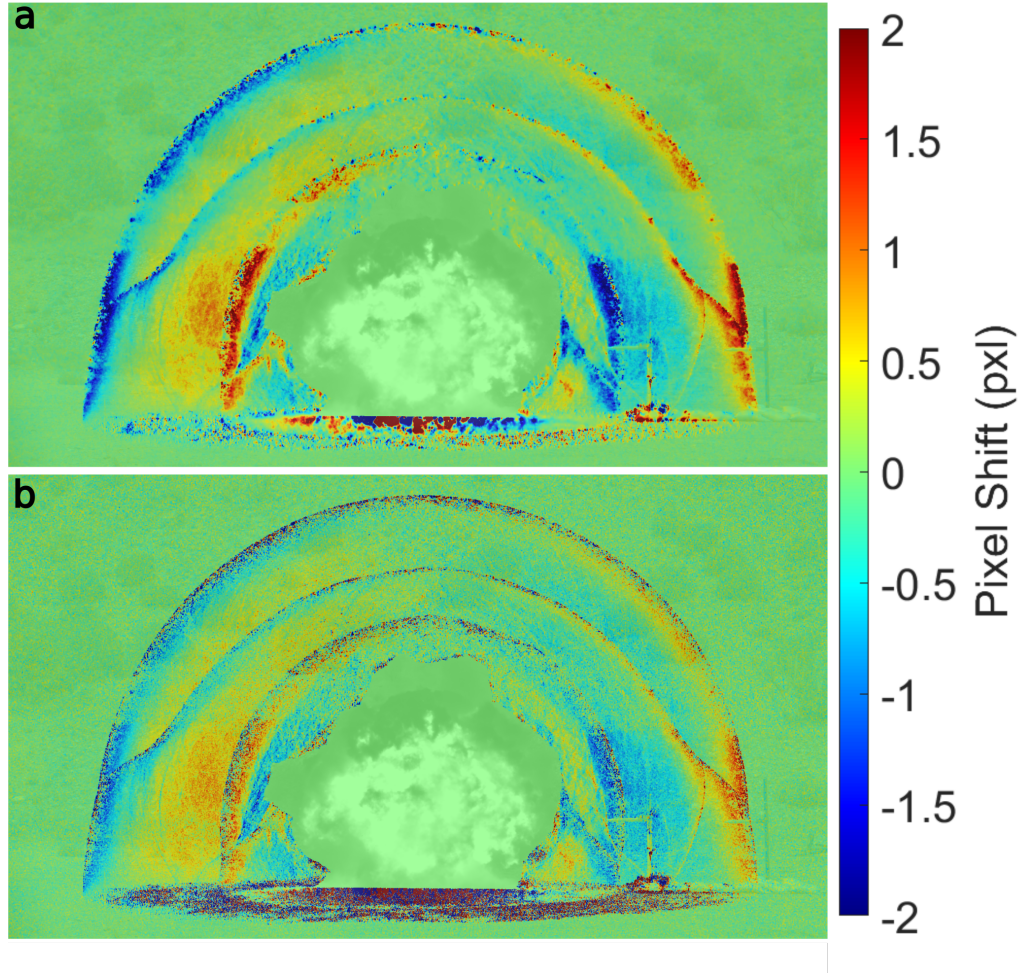
Figure 4.26: The horizontal displacement colored arrays. (a) shows the displacement values for HS, and (b) shows the displacement values for LK. The shockwave at both 4.4 ms and 10 ms is visualized.

The background noise calculated in the same area and manner as before is calculated from the sequential OF displacement values. The histogram for both OF methods is shown in Figure 4.27 where the average background distortion was found to be -0.006 pixels for both methods with a standard deviation of $\pm$ 0.048 pixels for HS, and $\pm$ 0.16 pixels for LK. This new standard deviation is significantly smaller than what was found in the Figure 3.3 histogram. The pressure profile was calculated in the same manner for the sequential OF and the results are shown in Figure 4.28 with the results from the non-sequential OF results also plotted. There is not a significant difference in the pressure measurements until approximately 4 ms (the location at which the shock wave from the flow-off image is interfering with the displacement results). Although the pressure results do not differ significantly, the overall error for both OF methods would decrease because the background noise decreased with the sequential OF method.
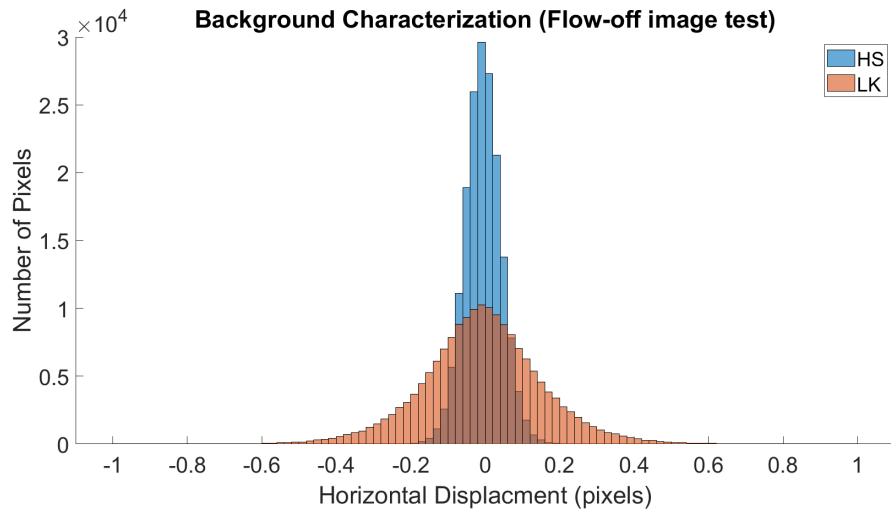
Figure 4.27: The background noise characterization plot for the sequential OF analysis
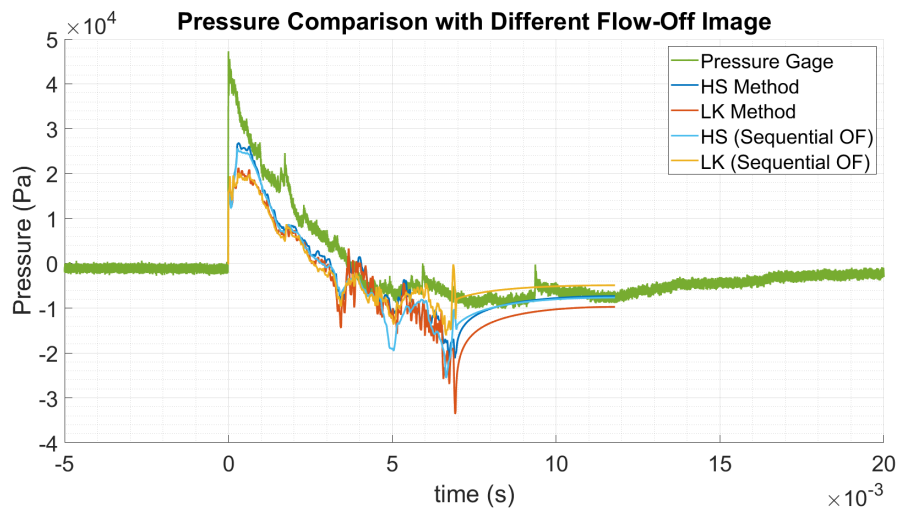
Figure 4.28: The pressure profile from both OF methods for the OF results calculated in Figure 4.17 with the addition of the sequential OF results.

CHAPTER 5

CONCLUSIONS AND FUTURE WORK

Background-oriented schlieren has been shown to be a useful technique to extract quantitative density from compressible flows. Two optical flow techniques were applied here to shock wave flows to measure quantitative density profiles in laboratory-scale and field-scale experiments. The density profile at various locations along a cone surface was calculated from small-scale experiments. The measured density profiles followed the quantitative schlieren and theoretical gas dynamic density profiles around the conical projectiles. Both optical flow techniques resulted in the same background noise error, but the LK method measured a higher pixel displacement inside the conical shock. The larger displacement caused the LK method to have a final relative density error upwards of 10 %, whereas the HS method only had a relative error of 5%. The theoretical slope between the cone surface and free-stream density was -0.145, the HS method calculated a slope of -0.147, and the LK method resulted in a slope of -0.184. While the smoothing parameter in the HS method had the ability to over-smooth the results, an α value between 0.01 and 0.1 were acceptable values. The density results for the acceptable range of α values result in similar slopes of -0.14 to -0.147 and all the plots are still closer to the theoretical profile than LK. Therefore, it is reasonable to conclude the HS OF method outperformed the LK method for small-scale tests.

For the large-scale tests, the general features behind the shock front were well captured. Generally, both OF techniques resulted in the same density and pressure values and they both estimated approximately the same pixel displacements. The HS method tended to resolve a higher pixel shift at the shock edge and the LK method showed the pixel shift for each pixel without any smoothing, however, this caused the data to be significantly more noisy. The LK method had a larger error in the final density and pressure profile since the OF background noise standard deviation was twice that of the HS method. Since the large-scale test used a natural background, it was expected to produce a higher error than the small-scale tests in general. But, the smoothing parameter in the HS method minimized the noise in the OF calculation by forcing neighboring pixels to have similar displacement values. The HS method outperformed the LK method overall in the large-scale tests.

5.1 Future Work

The range of smoothing parameters for the HS method was found to be between 0.01 and 0.1. The acceptable range for the smoothing parameter differs between applications, for the tests discussed here an $\alpha = 0.05$ produced detailed data that was not under or over-smoothed. However, it would be of interest to determine if this range of α variables for compressible flows always lies between 0.01 and 0.1 and if there is a specific number in this range that is optimal. The discussion of the shock width at the boundary between the shock wave and free-stream air was discussed briefly in this thesis. This is a discussion that can be expanded on further and researched further to determine how to get more detailed information at these boundaries. One suggestion to resolve the peak density at the shock boundary better would be to only process the OF methods inside of the shock wave and use 1D gas dynamic relationships to estimate the peak density measurement. Finally, for the small-scale tests specifically it would be interesting to test faster projectiles and shock interactions to determine the complexity of shock features OF BOS can resolve.

For large-scale tests, the flow-off image choice can either add additional noise to the system or minimize noise. As was shown here, a flow-off image with some illumination from the blast minimizes noise within the overall density reconstruction. However, it does limit the region in which data can be extracted since the shock wave from both the flow-off and flow-on images are captured in the OF analysis. It would be beneficial to investigate different applications where non-sequential and sequential OF analysis could be used to compare the methods further. The overall problem still stands that the background for BOS is the limiting factor to further quantitative data from natural background BOS images. To further validate that this is a background problem, it could be useful to test the large-scale tests again with a manufactured background that has sufficient variation. It would also be of interest to see if heat haze, the distortion of a background caused by heat radiating from an object in high-ambient temperatures, causes any error in the OF techniques. This is of interest when applying OF BOS to large-scale data sets on days where there is a high ambient temperature and heat haze is more prevalent. This was not seen as a large source of error for the large-scale tests discussed herein, but it would be of interest to determine if could be a source of error. For large-scale tests, it would be useful to compare the OF-derived density profile to a theoretical profile of the density variation behind the shock. This would allow a direct comparison without the additional errors associated with converting the OF density to pressure and would give a more detailed assessment of just the OF errors. Finally, it would be useful to test a different deconvolution method other than the Abel inversion for both small-scale and large-scale tests. Work by Molnar et al. [5] suggests that a Physics-Informed Neural Network can be used to improve BOS data. This in combination with HS OF could produce even better results and potentially reduce error.

REFERENCES

[1] James T. Heineck, Daniel W. Banks, Nathanial T. Smith, Edward T. Schairer, Paul S. Bean, and Troy Robillos. Background-oriented schlieren imaging of supersonic aircraft in flight. *AIAA Journal*, 59(1):11–21, 2021.

[2] Markus Raffel. Background-oriented schlieren (BOS) techniques. *Experiments in Fluids*, 56(60), 2015.

[3] T. Mizukaki, K. Wakabayashi, T. Matsumura, and K. Nakayama. Background-oriented schlieren with natural background for quantitative visualization of open-air explosions. *Shock Waves*, 24(1):69–78, 2013.

[4] O. K. Sommersel, D. Bjerketvedt, S. O. Christensen, O. Krest, and K. Vaagsaether. Application of background oriented schlieren for quantitative measurements of shock waves from explosions. *Shock Waves*, 18:291–297, 2008.

[5] Joseph P. Molnar, Lakshmi Venkatakrishnan, Bryan E. Schmidt, Timothy A. Sipkens, and Samuel J. Grauer. Estimating density, velocity, and pressure fields in supersonic flows using physics-informed BOS. *Experiments in Fluids*, 64(1), 2023.

[6] Masanori Ota, Friedrich Leopold, Ryusuke Noda, and Kazuo Maeno. Improvement in spatial resolution of background-oriented schlieren technique by introducing a telecentric optical system and its application to supersonic flow. *Experiments in Fluids*, 56(48), 2015.

[7] Benjamin H Wahls and Srinath V Ekkad. Temperature reconstruction of an axisymmetric enclosed reactive flow using simultaneous background oriented schlieren and infrared thermography. *Measurement Science and Technology*, 33, 2022.

[8] L. Venkatakrishnan, P. Suriyanarayanan, and G. Jagadeesh. Density field visualization of a micro-explosion using background-oriented schlieren. *Journal of Visualization*, 16(3):177–180, 2013.

[9] Mark Wernet. Real-time background oriented schlieren: Catching up with knife edge schlieren. Technical Report 220144, NASA, 2019.

[10] L. Venkatakrishnan and G. E. A. Meier. Density measurements using the background oriented schlieren technique. *Experiments in Fluids*, 37(2):237–247, 2004.

[11] Krzysztof Blachut and Tomasz Kryjak. Real-time efficient FPGA implementation of the multi-scale Lucas-Kanade and Horn-Schunck optical flow algorithms for a 4k video stream. *Sensors*, 22(13), 2022.

[12] Venkataraman Mahalingam, Koustav Bhattacharya, Nagarajan Ranganathan, Hari Chakravarthula, Robin Roberson Murphy, and Kevin Sheldon Pratt. A vlsi architecture and algorithm for Lucas-Kanade-based optical flow computation. *IEEE*, 2009.

[13] Bruce D. Lucas and Takeo Kanade. An iterative image registration technique with an application to stereo vision. In *Proceedings of Imaging Understanding Workshop*, pages 121–130, 1981.

[14] Bradley Atcheson, Wolfgang Heidrich, and Ivo Ihrke. An evaluation of optical flow algorithms for background oriented schlieren imaging. *Experiments in Fluids*, 46(3):467–476, 2008.

[15] Keisuke Hayasaka, Yoshiyuki Tagawa, Tianshu Liu, and Masaharu Kameda. Optical-flow-based background-oriented schlieren technique for measuring a laser-induced underwater shock wave. *Experiments in Fluids*, 57(12), 2016.

[16] Bora O. Cakir, Sergio Lavagnoli, Bayindir H. Saracoglu, and Christer Fureby. Assessent and application of optical flow in background-oriented schlieren for compressible flows. *Experiments in Fluids*, 64(11):11, 2023.

[17] P. Hariharan. *Basics of Interferometry*. Academic Press, 1 edition, 1991.

[18] W. H. Steel. *Interferometry, second Edition: Cambridge Studies in Modern Optics 1*. Combridge University Press, 1986.

[19] G. S. Settles. *Schlieren and Shadowgraph Techniques: Visualizing Phenomena in Transparent Media*. Springer, 2001.

[20] SPIE - The International Society ofor Optical Engineering. *Interferometry XII: Techniques and Analysis*, 2004.

[21] Michael J. Hargather and Gary S. Settles. A comparison of three quantitative schlieren techniques. *Optics and Lasers in Engineering*, 50(1):8–17, 2012.

[22] Michael John Hargather and Gary S. Settles. Natural-background-oriented schlieren imaging. *Experiments in Fluids*, 48(1):59–68, 2010.

[23] J.L. Barron, D.J. Fleet, and S.S Beauchemin. Performance of optical flow techniques. *International Journal of Computer Vision*, 12:43–77, 1994.

[24] F Nicolas, V Todoroff, A Plyer, G Le Besnerais, D Donjat, F Micheli, F Champagnat, P Cornic, and Y Le Sant. A direct approach for instantaneous 3d density field reconstruction from background-oriented schlieren (bos) measurements. *Experiments in Fluids*, 57(1):13, 2016.

[25] F. Nicolas, V. Todoroff, A. Plyer, G. Le Besnerais, D. Donjat, F. Micheli, F. Champagnat, P. Cornic, and Y. Le Sant. A direct approach for instantaneous 3d density field reconstruction from background-oriented schlieren (BOS) measurements. *Experiments in Fluids*, 57(1), 2015.

[26] Berthold K.P. Horn and Brian G. Schunck. Determining optical flow. *Artificial Intelligence*, 17:185–203, 1981.

[27] T Liu and L Shen. Fluid flow and optical flow. *J Fluid Mech*, 614:253–291.

[28] Deqing Sun, Stefan Roth, and Michael J. Black. A quantitative analysis of current practices in optical flow estimation and the principles behind them. *International Journal of Computer Vision*, 106(2):115–137, 2013.

[29] Bryan Schmidt and Mark Woike. Wavelet-based optical flow analysis for background-oriented schlieren image processing. *AIAA Journal*, 59:1–8, 2021.

[30] Bruce D. Lucas. *Generalized Image Matching by the Method of Differences*. PhD thesis, Carnegie-Mellon University, 1984.

[31] Jason M. Falls. High-speed quantitative schlieren measurement of density fields around conical supersonic projectiles. Master's thesis, New Mexico Tech, 2022.

[32] E.P. Simoncelli, E.H. Adelson, and D.J. Heeger. Probability distributions of optical flow. *IEEE Xplore*, pages 310–315, 1991.

[33] P. Kohle and A. Agrawal. Abel inversion of deflectometric data: Comparison of accuracy and noise propagation of existing techniques. *Appl. Optics*, 48(20):3894–3902, 2009.

[34] Jesse D. Tobin and Michael J. Hargather. Quantitative schlieren measurement of explosively-driven shock wave density, temperature, and pressure profiles. *Propellants, Explosives, Pyrotechnics*, 41(6):1050–1059, 2016.

[35] G.F. Kinney and K.J. Graham. *Explosive Shocks in Air*. Springer Berlin Heidelberg, 2013.

[36] J. W. Maccoll. The conical shock wave formed by a cone moving at a high-speed. *Proceedings of the Royal Society of London. Series A - Mathematical and Physical Sciences*, 159(898):459–472, 1936.

[37] Harry Ku. Notes on the use of propagation of error formulas. *Journal of Research of the National Bureau of Standards*, 70(4):263–273, 1966.

[38] John R. Taylor. *An Introduction to Error Analysis*. University Scgience Books, 1997.

APPENDIX A

RESEARCH PLAN FOR SMALL-SCALE TESTS

Research Project Summary:

The Shock and Gas Dynamics Laboratory (SGDL) is studying the density variation around ballistically launched projectiles of varying geometries. The purpose of the testing described here is to visualize and perform quantitative measurements using schlieren photography for density variation characterization.

High velocity ballistic experiments will be performed projectiles of various size, shape, and composition. The projectiles will be launched and caught using a sand catch. High speed schlieren imaging will leverage the Specialized Imaging SI-LUX 640 spoiled coherence laser illumination source. Where applicable, projectiles will be held in 3D printed or machined sabots and launched at velocities up to 2km/s. The launching of the projectiles will be performed using SGDL's universal receiver (UR) and various powder gun barrels located at the Ballistics Sciences Laboratory (BSL). A cut-down 50 BMG brass cartridge will be used to hold the powder charge and percussion primer when using 50, 55, 65, and 75 caliber systems. Other commercial cases will be used where appropriate. Commercial smokeless powders will be used for these powder charges. The IBHVG2 program will be used for predicting gun performance before a powder load is utilized to ensure developed gas pressure remains within the gun system, projectile, and sabot design specifications. The maximum allowable breech pressure for the 50 BMG barrel is 65 ksi, the expected breech pressure from IBHVG2 must be lower than this value. Testing at the BSL and operation of the gun system will be in accordance with the Gun Start of Day and Operational Procedures attached at the end of this document (attachment 5 and 6 respectively). In experiments with a detonator being used in combinations with the conical projectiles, attachment 9 (procedure for use of RP-80 detonators with Conical Projectiles) procedures and protocols will be followed.

Energetic Materials, Chemicals, or Hazardous Materials Involved:
- Commercial smokeless powders
- 50 BMG CCI #35 primers

Location of Operations:
- All testing will be conducted at the BSL
- Sabot assembly with projectiles (where applicable) will be performed offsite at the SGDL research lab L4 (EMRTC chemistry labs)

Material Storage Requirements:
- Smokeless powder will be stored in accordance with EMRTC ordinance requirements
- Projectiles do not require special storage considerations

Disposal Requirements:
- Any spilled smokeless powder will be collected and determination made if still usable:
  - If powder is still usable, it is not considered waste and will be used or stored as applicable and per regulatory requirements
  - Powder deemed not suitable for use in the gun system will be properly containerized in a designated container and stored as applicable and per regulatory requirements. No disposal of powder is required for this testing

Required Personnel:
- Operation of the gun system requires a minimum of two personnel (Gun Operator and Safety)

- SGDL personnel may fill the role of Test Engineer, and/or Gun Operator
- At least one EMRTC employee, Dr. Hargather, or Joe Gatto must be present during gun operation as Safety. The present EMRTC employee must be either an Ordnance Gunner or an Engineer 1 or higher.

- Personnel Limits – A maximum of three essential personnel may be present in the Firebooth. All non-essential personnel will be located in the Visitors and Instrumentation Observation Loft during operation of the gun system unless prior approval has been granted by the Safety Office

Personal Protective Equipment (PPE):
- Safety glasses and hearing protection will be worn by all personnel present during loading and firing of the gun system
- Laser safety glasses will be worn when the SI-LUX system is armed (see callouts in Attachment 7) (OD +5 at 640nm)
- Hardhats and steel toe boots will be worn by those lifting and unloading the sand catch when applicable
- See Attachment 2

Equipment Needed:
- Gun system
- 50 BMG reloading press
- Scale with tenth of a grain resolution (milligram resolution)
- Fan for air circulation
- Fire Extinguishers. Minimum requirements: One Class ABC fire extinguisher
  - One class D fire extinguisher if performing testing using metals which could combust (Aluminum or Magnesium)
  - It will be noted that in the event of a fire all personnel are to evacuate the BSL and contact campus police. No students shall fight any fire.
- Instrumentation as needed and provided by SGDL

Firing System Schematic:
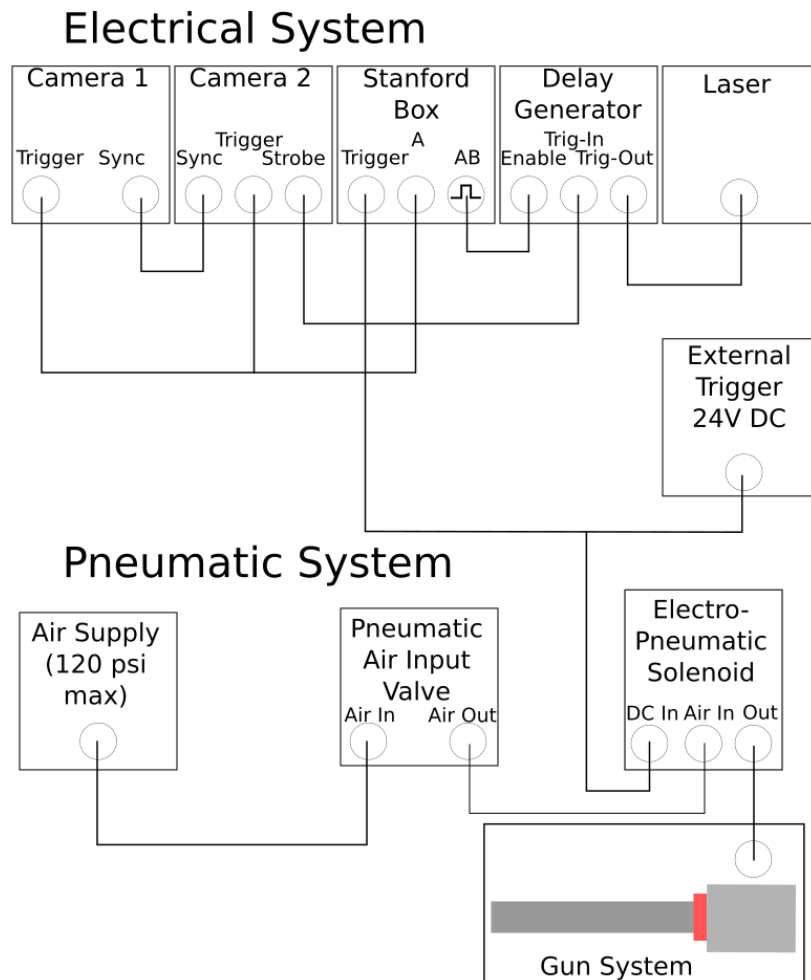
Planned Test Matrix:
Testing will encompass a variety of conical projectiles over an extended period of time. A test matrix will filed with the Safety Office and on file at the BSL prior to the start of each day of testing

Planned Testing Schedule or Duration of Project:
Testing may take place anytime Monday through Friday during normal EMRTC Field Lab operation hours.
This program is expected to have at least a 3-year duration.

Sand Catch Requirements
The bullets will be fires from a max distance of 100 feet into a catch box capable of arresting a .50 Cal. *The Ultimate Sniper* states that 24in of dry sand and 36in of wet sand are sufficient to stop a .50 Cal AP round at 100 yards. The fragmentation data sheet for the MK211 states that 24in of sand in the form of two sand bags will reduce the maximum fragmentation to 10ft. The sand catch will be observed during fire to assure proper function. This observation will assure that the round struck the catch, no sandbags have fallen, that none of the sandbags have deteriorated to the point where the sand is freely falling from the catch. It will also confirm that the back plate has not been struck.

The sand catch will be inspected between each shot to verify the sand catches is backed by enough sand bags to arrest the bullet. This inspection will consist of walking around the trap, checking for lose bags, checking for damaged bags, and checking for any damage on the back plate. Any bags that no longer hold shape or freely lose half of their sand, will be replaced. Damage to the back plate will suspend testing until it can be replaced.

References:
Include all references pertinent to the project

- SOP 101, Health and Safety
- SOP 103, Industrial Safety
- SOP 104, Laboratory Safety and Operations
- SOP 402, Emergency Action Plan
- SOP 403, Risk Management
- SOP 404, Hazardous Waste

Attachments:

1. Job Hazard Analysis
2. PPE Selection
3. Site Closure
4. Safety Data Sheets
5. Tailgate Briefing Form
6. Gun Start of Day Log
7. Gun Operational Procedures
8. Revised sand catch cleaning operation procedures
9. Procedure for use of RP-80 detonators with conical projectiles

Attachment 1

Job Hazard Analysis

Attachment 2

PPE Selection

Attachment 3

Site Closure

Site Closure

The following site closure shown in the map above will be observed:

1. Two Ton and the Torres facility magazine north west of the BSL building will be cleared and closed to personnel during testing
2. West Lab, East Lab, Vacuum Stability and the Torres facility magazine north of the BSL building will be open to personnel, but the personnel will remain behind the closure gate during testing. The Gun Operator is responsible for ensuring personnel at the listed facilities understand the closure and is responsible for providing these personnel clearance to enter or exit
3. The gate to East and West Labs will be closed.
4. The chain gate at the start of the access road leading to the BSL and lower Torres facilities will be closed
5. A Z-sign will be placed in front of the chain gate at the start of the access road leading to the BSL and lower Torres facilities as shown
6. A Z-sign will be placed at the top of the exterior staircase connecting the main Torres building to the BSL building
7. Personnel may work in the main Torres building during testing

Surface Danger Zone (SDZ)

The powder gun system is mounted in a fixed position with the barrel axis horizontal to the ground plane and the barrel bore 1.23 meters (48.5 inches) above the ground surface. A 50 caliber conical projectile travelling at 2km/s (6600ft/s) was found to demonstrate the farthest fly out

distance of the projectile shapes and sizes to be tested at the maximum theoretical muzzle velocity. This maximum fly out distance was calculated to be 770 meters (2530 feet) for the fixed horizontal orientation of the gun barrel. With the applied engineering controls, the surface danger zone (SDZ) for testing at the BSL with the powder gun system is reduced to a 100 meters (330 feet) radius with a 30-degree arc as shown in the site closure map above. The applied engineering controls to reduce the SDZ are as follows:

1. The powder gun is fixed to a test stand. This test stand ensures the gun's axis is horizontal to the ground to mitigate over shoot of projectile stops and the gun's axis is oriented parallel to the building NW centerline to minimize risk of projectiles missing projectile stops

2. Two primary projectile stops are employed to restrict potential projectile fly out to no more than 100 meters (330 feet):

    a. The primary projectile stop is installed down range of the gun system at the NW end of the BSL building. This stop is nominally 24" high by 24" wide by 36" deep and consists of a solid fill of dry sand. The primary stop will be no more than 15.15 meters (50 feet) from the muzzle of the gun system to minimize the possibility of a projectile missing the stop due to vertical or horizontal drift during flight

    b. The secondary projectile stop is the earthen hill directly behind the primary projectile stop. This hill starts approximately 57.6 meters (190 feet) from the gun emplacement and rises approximately 45.5 meters (140 feet) above the gun emplacement. This secondary stop ensures any projectiles that miss the primary projectile stop due to vertical or horizontal drift are restricted to a horizontal fly out of no more than 100 meters (330 feet)

Attachment 4

Safety Data Sheets

Attachment 5

Tailgate Briefing Form

Attachment 5

NEW MEXICO TECH ENERGETIC MATERIALS RESEARCH AND TESTING CENTER	**Tailgate Briefing Form**

TEST INFORMATION

Date:		Time:		Briefed By:	
Site:				Test Title:	
Test Engineer:				Safety:	
Gun Operator:					

WEATHER

Temp:			Wind:	Direction:		Precip:	
				Speed:		Cloud %:	

TOPICS COVERED

	Planned Site Activities		Chemical Hazards		Buddy Team Procedures
	Physical Hazards		PPE Required		Emergency Procedures
	Biological Hazards		Explosive Hazards		First Aid Procedures
	Heat/Cold Stress		Respiratory Hazards		Site Access / Clearances
	Site Communications		Decon Procedures		Other: Describe Below

Other:

BRIEFING ATTENDEES

Printed Name	Signature	Printed Name	Signature

By signing above, I certify that I have been briefed on and understand the information above.

NOTE: Tailgate briefings may need/have attachments from Ordnance or Instrumentation. Ensure all Tailgate Briefing forms are available if questions arise.

Attachment 6

Gun System Start of Day Log

START OF DAY LOG SHEET FOR GUN SYSTEM
(If already completed for the day of testing, go to gun system operation procedures)

1.1. Testing Conditions and Test Matrix:

      1.1.1.   Test Engineer: _____

      1.1.2.   Gun Operator: _____

      1.1.3.   Safety: _____

      1.1.4.   Note date/time: _____

      1.1.5.   Barometric pressure (HPa): _____

      1.1.6.   BSL inside temperature: _____

      1.1.7.   Number of planned gun tests: _____

      1.1.8.   Test matrix with powder loads to be used is attached
               Test Engineer Signature: _____

      1.1.9.   File Start of Day Log Sheet in designated folder at BSL

      1.1.10.   File Tailgate Briefing Form in designated folder at BSL

      1.1.11.   Pre-Test walkthrough completed with Dr. Hargather or EMRTC
      representative:

      _____

Attachment 7

Gun System Operational Procedures

The following operational procedures apply when using the SI-LUX 640 spoiled coherence 640nm laser illumination source for high speed imaging (henceforth referred to as "laser illumination source", "laser", or "SI-LUX"). The following modifications to test procedures apply to all projectiles. The testing procedure differs from RP-19-01 for reactive materials with modified and added steps included for SI-LUX laser operations

1. GUN PRETEST PROCEDURES

(If already completed and start of new test, go to 2)

1.1. **Start of Day**

1.1.1.   Ensure Start of day log has been filled and filed with a copy of test matrix at BSL

1.1.2.   Ensure Tailgate Briefing has been performed and form filed at BSL. Repeat if any new personnel arrive on site during testing. Gun Operator performs this review

1.1.3.   Check that a Z-sign is on entry road to Torres facility and a Z-sign is in place at the start of the stairs to the Ballistics Science Building (BSL) according to site closure map

1.1.4.   Check the Torres Main Building. If non-test related personnel are to be present in the Torres Main Building, inform them of testing to be performed in the BSL. Personnel may enter or exit Torres Main Building at will during testing in BSL.

1.1.5.   Ensure Torres facilities North of BSL, labeled in red in the Site Closure figure are clear of personnel.

1.1.6.   Check that the closure gate is closed according to the site closure map. Ensure personnel at West Lab, East Lab, Vacuum Stability and the Torres facility magazine north of the BSL building are aware that they are to remain behind the closure gate during testing and must obtain clearance from the Gun Operator to enter or leave the area

1.1.7.   Review fire procedures with all personnel to be present during testing. Repeat if any new personnel arrive on site during testing. Gun Operator performs this review

1.1.8.   Distribute PPE (hearing protection, laser safety goggles, and safety glasses) to all personnel to be present during testing

1.2. **System Hardware Checkouts (Firebooth, gun system, sabot stripper (where applicable), and ventilation system)**

1.2.1.   Ensure power is off to Firebox (No green or red light) by disconnecting   power supply

1.2.2.   Ensure Firebox cage is locked

1.2.3.   Approach gun from rear and switch Air Input Valve on air cylinder to "SAFE"

1.2.4.   Visually confirm breech and barrel are clear. As required to conduct visual inspection, disconnect cocking sear, open breech, and/or remove Chamber Flag

1.2.5.   Insert Chamber Flag into breech

1.2.6.   Check lateral play in recoil carriage. If play in the assembly is found, discontinue testing until recoil carriage has been disassembled and all fasteners checked and appropriately tightened

1.2.7.   Check that red barrel retainer nut is tight

1.2.8.   Check play in the bolt handle assembly. If play in the bolt assembly is found, discontinue testing until all fasteners have been checked and appropriately tightened

1.2.9.   Connect yellow airline to compressor or suitable compressed air supply (120psi main supply maximum)

1.2.10.   Set regulator pressure on compressor or air supply between 80 and 120psi

1.2.11.   Visually inspect sabot stripper for damage which could degrade operation and ensure sandbags are in place on bottom tray

1.2.12.   Situate ventilation duct perpendicular to muzzle of barrel. Duct opening should be two feet from barrel exit. Turn on ventilation system

1.2.13.   Visually inspect BSL building to ensure no equipment/hardware are in the line of fire of the gun system that is not designed to be so. Ensure all cleaning supplies and any flammables are safely stored behind the firing line

1.3. **Fire System Checkout**

1.3.1.   Ensure that laser warning signs are posted on the East and West doors to BSL, place the door barricades across the East and West doors, note the laser operator as the gun operator

1.3.2.   Ensure power to Firebox is disconnected, Firebox cage is locked, breech is open, Air Input Valve is set to "SAFE", and Chamber Flag is inserted in breech

1.3.3.   Pull air cylinder rod up to extend. Extend rod until it stops

1.3.4.   Turn Air Input Valve to "ARM"

1.3.5.   Return to Firebooth

1.3.6.   Obtain CAGE KEY and FIRE KEY from lockbox

1.3.7.   Obtain SI-LUX ARM KEY from instrumentation

1.3.8.   Confirm all persons present during testing are ready for a trigger check, announce LASER GOGGLES ON

1.3.9.   Arm the laser using SI-LUX software announcing ARMING LASER and LASER ARMED when the laser illumination source is being armed and is armed

1.3.10.   Using the SI-LUX ARM KEY arm the laser announcing LASER ARMED when the laser is ARMED

1.3.11.   Return to the Firebooth

1.3.12.   Open Firebox Cage

1.3.13.   Connect power supply to Firebox and ensure power is supplied (Green light on)

1.3.14.   Insert FIRE KEY into Firebox, turn to arm system (Red light on), and press fire button

1.3.15.   Disconnect power from Firebox (no green or red light) and close and lock Firebox Cage. Gun Operator retains CAGE KEY and FIRE KEY for all following steps

1.3.16.   Approach gun system and turn Air Input Valve to "SAFE". Visually confirm air cylinder rod has retracted

1.3.17.   When the gun system has been Safed approach the laser illumination source, check that the laser has been disarmed. disarm the SI-LUX if necessary announcing LASER DISARMED

1.3.18.   Turn off the laser illumination source and keep the SI-LUX ARM KEY announcing LASER OFF when clear

1.3.19.   If air cylinder rod retracts and system operates as expected, the gun system is ready for operation.

1.3.20.   If the air cylinder fails to retract, Gun Operator should repeat steps 1.3.2 through 1.3.13 after checking the following:
  - Air Input Valve is set to "ARM"
  - Air is supplied to control solenoid
  - Trigger line from Firebox to control solenoid is undamaged
  - Firebox outputs power when fire button is depressed

2. GUN FIRING PROCEDURE
(May only begin if Start of Day Pretest Sheet and all system checkouts have been performed. Perform for each test firing of the gun system)

2.1. System Alignment

2.1.1.   Ensure power to Firebox is disconnected, Firebox cage is locked, breech is open, Air Input Valve is set to "SAFE", and Chamber Flag is inserted in breech

2.1.2.   Remove Chamber Flag and insert laser bore sight

2.1.3.   Align target/gun for desired impact point

2.1.4.   Visually inspect sabot stripper for damage which could degrade operation and ensure sandbags are in place on bottom tray

2.1.5.   Align sabot stripper to ensure projectile will not impact stripper plate

2.1.6.   When alignment complete, remove bore sight and insert Chamber Flag

2.2. **Cartridge Loading**

2.2.1. Ensure power to Firebox is disconnected, Firebox cage is locked, breech is open, Air Input Valve is set to "SAFE", and Chamber Flag is inserted in breech

2.2.2. Clear BSL ground floor of all non-essential personnel. Non-essential personnel are to remain in the Visitors and Instrumentation Observation Loft during loading and firing of the gun system. The Firebooth is restricted to a maximum of three essential personnel only. The Test Engineer, Gun Operator, and Safety are the only personnel considered essential

2.2.3. Turn on ventilation fan. Ventilation fan is to remove combustion gases from BSL whenever necessary

The following steps are to be conducted by the Gun Operator only. Eye protection is required for all steps for all personnel, hearing protection is required for the gun operator from Step 2.2.9 and from Step 2.2.14 for all other personnel until the gun has been cleared. The CAGE KEY FIRE KEY and SI-LUX ARM KEY are to remain on the Gun Operator's person at all times unless inserted in the Firebox Cage lock, Firebox, or SI-LUX laser unit, respectively.

2.2.4. Obtain propellant to be used for testing from the back room and bring to the loading bench. ONLY ONE powder may be on the loading bench at any given time

2.2.5. Install resizing dies on 50 BMG reloading press on loading bench

2.2.6. Deprime and resize propellant case (cutdown 50 BMG case)

2.2.7. If case originally had a crimped primer, deburr primer pocket

2.2.8. Use rotary scraper to remove carbon deposits

2.2.9. If removed primer was impacted, but did not initiate, return impacted primer to the lock box for later removal by EMRTC personnel

2.2.10. Remove resizing dies and install primer installing tool on 50 BMG reloading press

2.2.11. Insert No. 35 50 BMG primer, open end up, into tool and resized case into

holder. Fully press primer into case (press until tool stops at preset depth). Check that primer face is recessed (~0.005") below surface of the case base

2.2.12.   Weigh out desired powder load for test using weigh boat on scale

2.2.13.   Pour powder that has been weighed out into case using funnel. Press floral foam into case to fill empty volume and ensure powder is retained against primer

2.2.14.   Place the projectile and loaded cartridge onto opposing sides of the gun stand and approach the laser illumination source

2.2.15.   Announce LASER GOGGLES ON, arm laser announcing ARMING LASER and LASER ARMED when each step is completed

2.2.16.   Turn on the laser illumination source using the SI-LUX ARM KEY announcing LASER ON

2.2.17.   Return to gun and load projectile using depth gauge to achieve desired insertion depth in breech

2.2.18.   Verbally announce "EARS ON, LOADING GUN" to all personnel. Insert loaded case into breech and close bolt

2.2.19.   Engage cocking lever, then move to rear of gun and turn Air Input Valve to "ARM"

2.2.20.   Return to Firebooth

2.2.21.   Ensure non-essential personnel are behind barricades in the loft. Ensure essential personnel are behind Firebooth barricades

2.2.22.   Open Firebox Cage and connect power to Firebox (Green light on)

2.2.23.   Verbally announce "KEY IN" to all personnel and insert FIRE KEY into Firebox. Turn FIRE KEY to arm Firebox (Red light on)

2.2.24.   Verbally announce countdown "FIRING IN THREE, TWO, ONE" to all personnel. Press orange fire button

2.2.25.   After gun fires, verbally announce "KEY OUT" to all personnel, remove key from Firebox, disconnect power from Firebox, and lock Firebox Cage.

Retain CAGE KEY and FIRE KEY on person. Proceed to the Clear Gun Procedure (Section 2.3)

2.2.26.   If gun fails to fire, verbally announce "KEY OUT" to all personnel, remove key from Firebox, disconnect power from Firebox, and lock Firebox Cage.
Retain CAGE KEY and FIRE KEY on person. Proceed to the Gun Misfire Procedure (Section 2.4)

2.3. **Clear Gun Procedure:**
The following steps are to be performed only by the Gun Operator. Eye and ear protection is to be worn by all personnel until gun has been announced as clear

2.3.1.   Ensure power to Firebox is disconnected and Firebox cage is locked

2.3.2.   Approach gun from rear and turn Air Input Valve to "SAFE"

2.3.3.   Lower bolt and use extraction tool to remove case from breech. If case cannot be extracted using extraction tool, insert the brass pushrod into the muzzle and push case out of breech

2.3.4.   Visually inspect breech/bore to ensure barrel is clear

2.3.5.   Insert Chamber Flag into breech and verbally announce "GUN CLEAR" to all personnel

2.3.6.   Approach the laser illumination source, disarm the laser announcing LASER DISARMED, and LASER OFF. Retain SI-LUX ARM KEY on person

2.3.7.   Personnel may now remove laser safety goggles and return to the BSL main floor

2.3.8.   For continued testing, return to step 2.1.1

2.4. **Misfire Procedure:**
The following steps are to be performed only by the Gun Operator. Eye and ear protection is to be worn by all personnel during these steps

2.4.1.   Ensure power to Firebox is disconnected and Firebox cage is locked

2.4.2.   Call safety office to alert of misfire and walk through steps 2.4.3-2.4.14 together

2.4.3.   Verbally announce "MISFIRE, 30 SECOND COUNT" to all personnel and begin a 30 second count

2.4.4.   Approach gun from rear and turn Air Input Valve to "SAFE"

2.4.5.   If cocking lever has not been pulled, disconnect cocking lever from bolt

2.4.6.   Lower bolt and use extraction tool to remove loaded case

2.4.7.   Return loaded case to loading bench and approach laser illumination source

2.4.8.   Disarm SI-LUX laser announcing LASER DISARMED and LASER OFF, the gun operator retains the SI-LUX ARM KEY

2.4.9.   If the misfire occurred due to a failure of the firing system (failure to trigger, broken firing pin, etc), return loaded case to loading bench. Make the necessary repairs to the firing system and return to Section 1.3: Fire System Checkout before returning to Step 2.2.13

2.4.10.   If the firing system was observed to operate and a primer indentation found on the loaded case, return to Step 2.2.13 and proceed

2.4.11.   If three misfires are observed, return loaded case to loading bench, remove foam wadding, and pour powder into weigh boat. Leave powder and set misfired primed case to the side. Return to beginning of firing procedure to proceed forward reloading a new case

2.4.12.   If another misfire is observed with a newly primed case, suspend testing until the misfire cause can be identified and rectified

2.4.13.   If three misfired are observed, return loaded case to loading benc, remove foam wadding, and pour powder to source container and set misfired primer to the side. Return to beginning of firing procedure to proceed forward reloading a new case

2.4.14.   If another misfire is observed with a newly primed case, suspend testing until the misfire cause has been identified and rectified.

Powder should be returned to source container and impacted primer to the lock box for later removal by EMRTC personnel

3. GUN POST TEST PROCEDURES
(Proceed if all testing with the gun system is complete for the day)

3.1. System Hardware Shutdown (Firebooth and gun system)

3.1.1.   Ensure power is off to Firebox (No green or red light) by disconnecting   power supply

3.1.2.   Ensure Firebox Cage is locked

3.1.3.   Approach gun from rear and switch Air Input Valve on air cylinder to "SAFE"

3.1.4.   Visually confirm breech and barrel are clear. As required to conduct visual inspection, disconnect cocking handle, open breech, and/or remove Chamber Flag

3.1.5.   Insert Chamber Flag into breech

3.1.6.   Disconnect yellow airline from air supply

3.1.7.   Return CAGE KEY and FIRE KEY to lockbox

3.1.8.   Turn off ventilation system

Attachment 8

Revised Sand Catch Cleaning Operation Procedures

1. SANDCATCH POST TEST PROCEDURES

A revised sand catch is used to safely catch projectiles of greater mass than the original 55 gallon drum used for RP-19-01: Study High Velocity Impact of Reactive Materials Using 0.55 Caliber Powder Gun. Specifications on the revised sand catch are in accordance with TP-19-25 for lot testing of 50 BMG. The sand catch is approximately 1800 pounds fully loaded, and as such any lifting operations will be performed by those wearing hard hats and steel toes. The Titan Telescoping Gantry Cane has the lowest capacity rating of all components in the sand catch with a load rating of 3000 pounds. The minimum factor of safety for the lifting operation is 1.7 on the published ratings for all components. No fewer than two operators will be involved with the emptying of the sand catch. The sand catch will be cleaned after a maximum of 20 shots into the catch, or at the end of a test series where the next session will exceed the maximum number of shots before cleaning.

1.1.   Distribute appropriate PPE

1.2.   Move the gantry crane into place and the sand catch tub and cribbing into place for receiving the sand if fully dumping

1.3.   Ensure that the casters on the gantry crane and the catch tub are locked

1.4.   Attach the three lifting lugs of the sand catch chain hoist to the crane using the lifting straps, and D-Ring shackles

1.5.   Tension the chain hoist without lifting the sand catch, check that all lengths of chain are equal and tensioning properly

1.6.   Begin lifting using the chain hoist such that the sand catch is raised off of the steel welding table

1.7.   Unlock the casters on the gantry crane and using team pushing to position the sand catch above the catch tub

1.8.   Position the front 4 to 10 inches of the sand catch overhanging the catch tub

1.9.   Lower the sand catch onto the cribbing and the catch tub

1.10.   Translate the gantry crane back and attach the rearward lifting lugs on the sand catch onto the crane

1.11.   Remove the face plate of the sand catch using the four toggle clamps

1.12.   Tip the catch up slightly using the gantry crane

1.13.   Remove all of the sand from the catch using a shovel

1.14.   Inspect the rubber plug and the plywood for damage

      1.14.1. Rubber plugs can be used for three shooting sessions

      1.14.2. Plywood is to be replaced after every other shooting session, or if any damage is noted on the face

      1.14.3. Visibly Inspect the AR500 back plate for damage, replace the AR500 plate if any damage is visible

1.15.   Lay the sand catch back level, refill sand (if applicable) using shovels, and reinstall the faceplate on the catch

Attachment 9

Procedure for use of RP-80 Detonators with Conical Projectiles

1. **Purpose:**

   The Shock and Gas Dynamics Laboratory (SGDL) is studying the density variation around projectiles passing through an explosively-driven shock wave. The purpose of the testing described here is to visualize and perform quantitative measurements using schlieren photography for density variation characterization.

   High velocity ballistic experiments will be performed projectiles of various size, shape, and composition. The projectiles will be launched and caught using a sand catch in accordance with EMRTC Test Plan TP-19-25: 50 Cal Match Ammunition Testing. A detonator will be used to produce a shock wave which will be directed toward the projectile in flight. High speed schlieren imaging capture images of the interaction between the projectile and the explosively driven shock wave. This addendum addresses the changes to add the detonator to the gun operations.

2. **Energetic Materials, Chemicals, or Hazardous Materials Involved:**
   2.1. Commercial smokeless powders
   2.2. 50 BMG CCI #35 primers
   2.3. RP-80 open-faced detonators

3. **Location of Operations:**
   3.1. All testing will be conducted at the BSL

4. **Material Storage Requirements:**
   4.1. Smokeless powder will be stored following EMRTC ordinance requirements
   4.2. Projectiles do not require special storage considerations

5. **Disposal Requirements:**
   5.1. Any spilled smokeless powder will be collected, and a determination made if still usable:
      5.1.1. If the powder is still usable, it is not considered waste and will be used or stored as applicable and per regulatory requirements
      5.1.2. Powder deemed not suitable for use in the gun system will be properly containerized in a designated container and stored as applicable and per regulatory requirements. No disposal of powder is required for this testing

6. **Required Personnel:**
   6.1. Ordnance personnel are required for operations involving RP-80 detonators
   6.2. Operation of the gun system requires a minimum of two personnel (Gun Operator and Safety)
   6.3. SGDL personnel may fill the role of Test Engineer, and/or Gun Operator
   6.4. At least one EMRTC employee, Dr. Hargather, or Joe Gatto must be present during gun operation as Safety. The present EMRTC employee must be either an Ordnance Gunner or an Engineer 1 or higher. Operations involving RP-80 detonators will require an Ordnance Tech.

6.5. Personnel Limits – A maximum of three essential personnel may be present in the Firebooth. All non-essential personnel will be located in the Visitors and Instrumentation Observation Loft during the operation of the gun system unless prior approval has been granted by the Safety Office

7. Personal Protective Equipment (PPE):
7.1. Safety glasses and hearing protection will be worn by all personnel present during the loading and firing of the gun system and handling of RP-80s
7.2. Laser safety glasses will be worn when the SI-LUX system is armed (see callouts in Attachment 7) (OD +5 at 640nm)
7.3. Hardhats and steel toe boots will be worn by those lifting and unloading the sand catch when applicable
7.4. See Attachment 2

8. Equipment Needed:
8.1. Gun system
8.2. 50 BMG reloading press
8.3. Scale with a tenth of a grain resolution (milligram resolution)
8.4. Detonator Mount
8.5. Working Ventilation System
8.6. Fire Extinguishers. Minimum requirements: One Class ABC fire extinguisher
    8.6.1. One class D fire extinguisher if performing testing using metals that could combust (Aluminum or Magnesium)
    8.6.2. In the event of a fire, all personnel is to evacuate the BSL and contact campus police. No students shall fight any fire.
8.7. 2 Stanford Boxes
8.8. Fire Set
8.9. Other instrumentation as needed and provided by SGDL

9. Sequence of Steps:
Follow Gun Operational Procedures found in Attachment 7, replacing Section 2 (Gun Firing Procedure) with the following steps

GUN FIRING PROCEDURE
(May only begin if Start of Day Pretest Sheet and all system checkouts have been performed. Perform for each test firing of the gun system)

9.1. **System Alignment**
    9.1.1. Ensure power to Firebox is disconnected, Firebox cage is locked, breech is open, Air Input Valve is set to "SAFE", and Chamber Flag is inserted in breech
    9.1.2. Remove Chamber Flag and insert laser bore sight
    9.1.3. Target/gun for desired impact point
    9.1.4. Place detonation holder in the desired location

9.1.5.   Inspect sabot stripper for damage that could degrade operation and ensure sandbags are in place on the bottom tray

9.1.6.   Inspect sabot stripper to ensure projectile will not impact stripper plate

9.1.7.   When alignment is complete, remove bore sight and insert Chamber Flag

9.2. **Cartridge Loading**

9.2.1.   Ensure power to Firebox is disconnected, Firebox cage is locked, the breech is open, Air Input Valve is set to "SAFE", and Chamber Flag is inserted in the breech

9.2.2.   Clear BSL ground floor of all non-essential personnel. Non-essential personnel is to remain in the Visitors and Instrumentation Observation Loft during the loading and firing of the gun system. The Firebooth is restricted to a maximum of three essential personnel only. The Test Engineer, Gun Operator, and Safety are the only personnel considered essential

9.2.3.   Turn on the ventilation fan. A ventilation fan is to remove combustion gases from BSL whenever necessary

The following steps are to be conducted by the Gun Operator only. Eye protection is required for all steps for all personnel, hearing protection is required for the gun operator from Step 9.2.4 and from Step 9.2.20 for all other personnel until the gun has been cleared. The CAGE KEY FIRE KEY and SI-LUX ARM KEY are to always remain on the Gun Operator's person unless inserted in the Firebox Cage lock, Firebox, or SI-LUX laser unit, respectively.

9.2.4.   Obtain propellant to be used for testing from the back room and bring it to the loading bench. ONLY ONE powder may be on the loading bench at any given time

9.2.5.   Install resizing dies on a 50 BMG reloading press on the loading bench

9.2.6.   De-prime and resize propellant case (cutdown 50 BMG case)

9.2.7.   If the case originally had a crimped primer, deburr primer pocket

9.2.8.   Use the rotary scraper to remove carbon deposits

9.2.9.   If removed primer was impacted, but did not initiate, return impacted primer to the lockbox for later removal by EMRTC personnel

9.2.10. Remove resizing dies and install primer installing tool on 50 BMG reloading press

9.2.11. Insert No. 35 50 BMG primer, open the end up into the tool, and resized the case into the holder. Fully press primer into the case (press until tool stops at preset depth). Check that the primer face is recessed (~0.005") below the surface of the case base

9.2.12. Weigh out desired powder load for test using weigh boat on scale

9.2.13. Pour powder that has been weighed out into the case using a funnel.

9.2.14. Press floral foam into the case to fill the empty volume and ensure powder is retained against the primer

9.2.15. Place the projectile and loaded cartridge onto opposing sides of the gun stand

Only Ordnance will carry out steps 9.2.16 - 9.2.18, and 9.2.26

9.2.16. Insert the RP-80 detonator into the detonator holder from the back, *detonator will remain disconnected from the firing line during insertion and cartridge loading*

9.2.17. Ensure detonator is flush to the small lip at the front of the holder, and tape it in place from the back

9.2.18. Connect long detonator leads (5m to 30m in length) to the detonator so that it can be connected to the firing line from behind the gun or inside the firing booth after the cartridge is loaded.
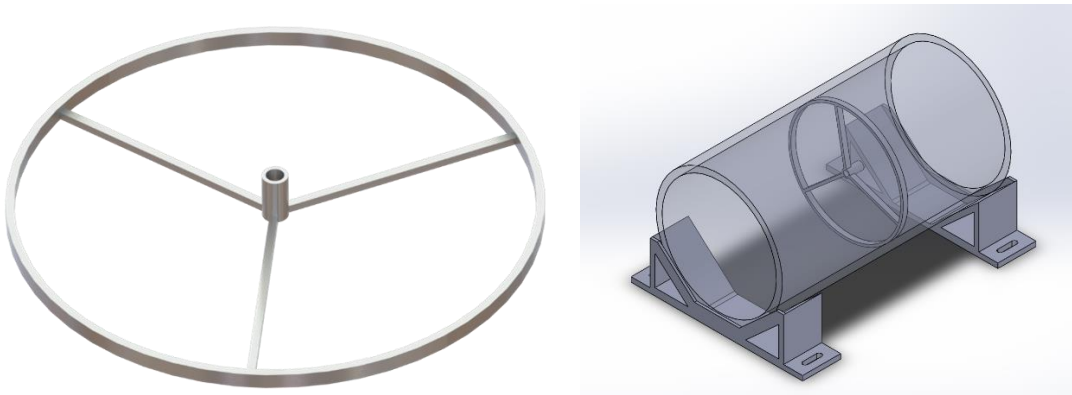
Figure 1: Image on the left is the detonator holder, and the diagram on the right is the fully assembled detonator holder with the casing (shown in grey) being a 6" PVC pipe, the detonator holder (shown a s a dashed line) placed inside the PVC pipe, and the detonator (shown in blue) placed in the center of the holder.

9.2.19. Announce LASER GOGGLES ON, arm laser announcing ARMING LASER and LASER ARMED when each step is completed

9.2.20. Turn on the laser illumination source using the SI-LUX ARM KEY announcing LASER ON

9.2.21. Return to gun and load projectile using depth gauge to achieve desired insertion depth in breech

9.2.22. Verbally announce "EARS ON, LOADING GUN" to all personnel. Insert loaded case into the breech and close bolt

9.2.23. Engage cocking lever, then move to the rear of the gun and turn Air Input Valve to "ARM"

9.2.24. Return to Firebooth

9.2.25. Ensure non-essential personnel is behind barricades in the loft. Ensure essential personnel are behind Firebooth barricades

9.2.26. Ordnance will connect firing line to fire set

9.2.27. Open Firebox Cage and connect power to Firebox (Green light on) Verbally announce "KEY IN" to all personnel and insert FIRE KEY into Firebox.

9.2.28. Ordnance charge fs_17, announce "READY TO FIRE"

9.2.29. Turn FIRE KEY to arm Firebox (Red light on) Verbally announce countdown "FIRING IN THREE, TWO, ONE" to all personnel. Press the orange fire button

9.2.30. After the gun fires, verbally announce "KEY OUT" to all personnel, remove the key from Firebox, disconnect power from Firebox, and lock the Firebox Cage. Retain the CAGE KEY and FIRE KEY on the person. Proceed to the Clear Gun Procedure (Section 9.3)

9.2.31. If the gun fails to fire, verbally announce "KEY OUT" to all personnel, remove the key from Firebox, disconnect power from Firebox, and lock the Firebox Cage. Retain the CAGE KEY and FIRE KEY on the person. Proceed to the Gun Misfire Procedure

9.2.32. If detonator fails to fire, but gun fires then attempt to fire the detonator again will be made using the FS-17. If detonator still fails to function, a 30 minute wait time will be started. Then the gun will be cleared, the laser turned off, and theRP-80 cleared.

9.3. **Clear Gun Procedure:**
The following steps are to be performed only by Ordnance. Eye and ear protection is to be worn by all personnel until the gun has been announced as clear

9.3.1.   Ensure power to Firebox is disconnected and the Firebox cage is locked

9.3.2.   Ordnance will disconnect the firing line from the fire set

9.3.3.   Approach the gun from the rear and turn Air Input Valve to "SAFE"

9.3.4.   Lower the bolt and use the extraction tool to remove the case from the breech. If the case cannot be extracted using the extraction tool, insert the brass pushrod into the muzzle and push the case out of the breech

9.3.5.   Visually inspect breech/bore to ensure barrel is clear

9.3.6.   Insert Chamber Flag into breech and verbally announce "GUN CLEAR" to all personnel

9.3.7.   Approach the laser illumination source, disarm the laser announcing LASER DISARMED, and LASER OFF. Retain SI-LUX ARM KEY on person Personnel may now remove laser safety goggles and return to the BSL main floor

9.3.8.   For continued testing, return to step 9.1.1

9.4. **Misfire Procedure:**

9.4.1.   Ensure power to Firebox is disconnected and Firebox cage is locked

Only ordnance will conduct steps 9.4.2-9.4.3

9.4.2.   Ordnance will detonate the detonator

9.4.3.   Ordnance will disconnect the firing line from the fire set

The following steps are to be performed only by the Gun Operator. Eye and ear protection is to be worn by all personnel during these steps

9.4.4.   Call safety office to alert of misfire and walk through steps 9.4.4-9.4.16 together

9.4.5.   Verbally announce "MISFIRE, 30 SECOND COUNT" to all personnel and begin a 30 second count

9.4.6.   Approach gun from rear and turn Air Input Valve to "SAFE"

9.4.7.   If cocking lever has not been pulled, disconnect cocking lever from bolt

9.4.8.   Lower bolt and use extraction tool to remove loaded case

9.4.9.   Return loaded case to loading bench and approach laser illumination source

9.4.10.   Disarm SI-LUX laser announcing LASER DISARMED and LASER OFF, the gun operator retains the SI-LUX ARM KEY

9.4.11.   If the misfire occurred due to a failure of the firing system (failure to trigger, broken firing pin, etc), return loaded case to loading bench. Make the necessary repairs to the firing system and return to Section 1.3: Fire System Checkout before returning to Step 2.2.13

9.4.12. If the firing system was observed to operate and a primer indentation found on the loaded case, return to Step 2.2.13 and proceed

9.4.13.   If three misfires are observed, return loaded case to loading bench, remove foam wadding, and pour powder into weigh boat. Leave powder and set misfired primed case to the side. Return to beginning of firing procedure to proceed forward reloading a new case

9.4.14. If another misfire is observed with a newly primed case, suspend testing until the misfire cause can be identified and rectified

9.4.15. If three misfired are observed, return loaded case to loading bench, remove foam wadding, and pour powder to source container and set misfired primer to the side. Return to beginning of firing procedure to proceed forward reloading a new case

9.4.16. If another misfire is observed with a newly primed case, suspend testing until the misfire cause has been identified and rectified. Powder should be returned to source container and impacted primer to the lock box for later removal by EMRTC personnel

10. Firing System Schematic:
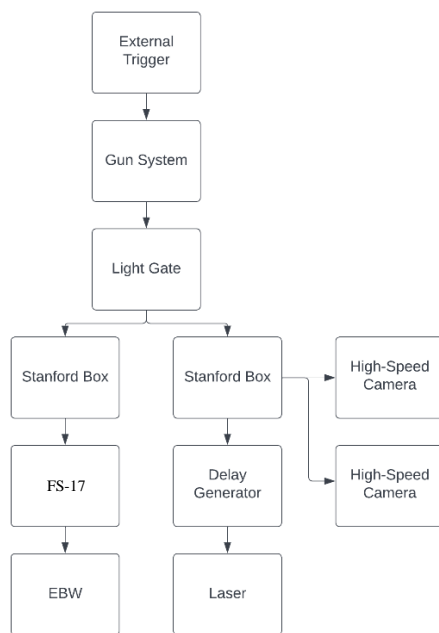
11. Planned Test Matrix:

Testing will encompass a variety of conical projectiles over an extended period. A test matrix will be filed with the Safety Office and on file at the BSL before the start of each day of testing

12. Planned Testing Schedule or Duration of Project:

Testing may take place anytime Monday through Friday during normal EMRTC Field Lab operation hours. This program is expected to have at least a 3-year duration.

13. References:

Include all references pertinent to the project

13.1.   SOP 101, Health and Safety
13.2.   SOP 103, Industrial Safety
13.3.   SOP 104, Laboratory Safety and Operations
13.4.   SOP 402, Emergency Action Plan
13.5.   SOP 403, Risk Management
13.6.   SOP 404, Hazardous Waste

QUANTITATIVE BACKGROUND-ORIENTED SCHLIEREN (BOS) MEASUREMENTS OF EXPLOSIVES AND HIGH-SPEED PROJECTILES USING OPTICAL FLOW TECHNIQUES

by

Kailene Marie Strebe

NEW MEXICO TECH

SCIENCE • ENGINEERING • RESEARCH UNIVERSITY